Modelling for Transient Optically Induced Metal-Insulator Transitions in Narrow-Gap Semiconductors and Semimetals

by

Jordina Vidal

Submitted to the Department of Physics
in partial fulfillment of the requirements for the degree of

Philosophy Doctor in Physics

at the

MASSACHUSETTS INSTITUTE OF TECHNOLOGY

May 1994

Author .....
Department of Physics
May 20, 1994

Certified by .....
Mildred S. Dresselhaus
Institute Professor
Thesis Supervisor

Accepted by .....
George Koster
Chairman, Physics Graduate Committee

Modelling for Transient Optically Induced Metal-Insulator Transitions in Narrow-Gap Semiconductors and Semimetals

by

Jordina Vidal

Submitted to the Department of Physics
on May 20, 1994, in partial fulfillment of the
requirements for the degree of
Philosophy Doctor in Physics

Abstract

The theoretical work presented in this thesis is based on models developed to interpret a series of optical experiments with short-pulse lasers, which allow a time-domain study of phenomena on a sub-picosecond timescale. By means of a pump-probe technique, we observe large amplitude oscillations in the time domain reflectivity response of a series of narrow-gap semiconductors and semimetals. The oscillations have the frequency of the fully-symmetric optical phonon mode of the system, and are maximally displaced from their midpoint value at zero time delay between pump and probe. These features indicate that a coherent phonon vibration is generated in these materials via an electronic excitation at different points of the Brillouin zone, which displaces instantaneously the equilibrium positions of the atoms. It is precisely this generation of coherent phonons that makes the time-domain technique distinct from conventional frequency domain techniques, such as Raman and neutron scattering.

Using a range of theoretical techniques, from nearly free electron models to state-of-the art *ab initio* calculations, I have made quantitative microscopic evaluations of the coherent phonon phenomenon. The studies focus on two unique aspects of having such coherent atomic vibrations in a narrow gap material, with special emphasis on the group V semimetals Sb and Bi. First of all, I have performed dynamical band structure calculations, as a function of the coherent atomic motion, in order to inspect the possibility of a transient metal-insulator transition at a terahertz frequency. Secondly, I have calculated the evolution of the displaced atoms in quasi-equilibrium with the laser-excited carriers, as the electron-ion coupled system returns to its ground state equilibrium. These calculations are fundamental, insofar they provide a quantitative microscopic description of the coherent phonon phenomenon. Moreover, the predicted magnitude of the atomic displacements, and the resulting band gap shifts in Sb, indicate that this material can undergo a metal-insulator transition at a terahertz frequency, when illuminated by a high power short pulse laser.

Thesis Supervisor: Mildred S. Dresselhaus
Title: Institute Professor

Acknowledgments

This work would not have been possible without the help and encouragement of the many exceptional people whom I have met during my graduate studies at MIT.

First of all, I would like to thank my advisor, Prof. Mildred Dresselhaus, who is "a well full of science"[1], a mountain of energy and a model of hard work and commitment to science and society. Despite her tight schedule, she has always been able to dedicate time to her students, and she has supported me in the most difficult moments. I want to thank also her longtime companion Gene Dresselhaus, who has run the "MGM-base" down the corridor in the absence of Millie. Not only have I learnt from him that group theory explains everything, but also that there are in this world supportive men who can happily live beside successful women. A last aknowledgment for Gene is directed to his work in improving the group computers, and his patience with my obstinate tendency to fill the system disk. Also thanks to the other computer hackers in our group, Lyndon Hicks, Boris Pevzner and Alex Fung, without whom I could not have written my thesis from my office terminal.

My work collaborator Steve Cheng would deserve a whole aknowledgments page by himself. Not only has he provided the experimental data for this thesis, but he has also promoted very interesting theoretical discussions. His expertise in optical matters and insight in physics have been crucial in shaping the progress of our research. In addition, Steve has trained me in the arts of presentation and communication, which he masters with excellence. His unlimited curiosity and enthusiasm, in and outside the lab, have been a permanent motivator throughout these years. Our discussions about just anything, from physics to anti-physics, have been joined sometimes by his fiancée Melissa. I wish this exceptional couple all my best, and I hope they decide to spend their honeymoon by the historical waters of the Mediterranean sea, with a stop over in Barcelona.

I also thank Herb Zeiger, whose expertise, pacience and perseverance have been key to the success of our theoretical discussions.

[1] Translation from the catalan "un pou de ciència".

To my advisor overseas, Xavier Gonze, I owe all my modest knowledge of the wonderful field of the *ab initio* techniques, and also a great gratitude for his tireless disposition. Without his generous invitation to collaborate with him in Louvain, and his help in getting the project to converge, a crucial chapter in this thesis would be missing. Also thanks to his graduate students. Jean Christophe Charlier, whom I congratulate for the successful accomplishment of his doctorate, even when his 1-year-old daughter Ilona would not allow him to sleep at nights. Philippe Goshez, for the nice evenings that you provided to the lonely visitor. And to all the members of the PCPM lab, with whom I shared so numerous coffee breaks.

I want to thank Prof. Erich Ippen, for his trust and patience, and also for the many good questions that he asked, some of which remain unanswered.

My two consecutive officemates occupy a very special place in this list of aknowledgements. First of all, Stan di Vittorio, who embodies the best of the old and the new continents in a perfect balance. I hope that our unquiet spirits settle down in the same city sime time. The kindness and support of his successor, James Chen, have no parallel in anybody I know. Amusing conversator, he kept me aware of all sorts of interesting things which I would have missed without him. Moreover, he spoiled me like I had never been spoiled, especially in the most difficult moments. Thanks James.

I also wanted to thank Peggy Berkovitz, the graduate students administrator, who has been like a mother for all of us.

If I start with my friends, I fear that this section can become longer than the thesis itself. Between the walls of this great institution that is MIT, I have met a bunch of wonderful people, whose support and friendship have been a cornerstone for my development during my stay in Boston. I hope they will forgive me for just enumerating them in chronological order, and I beg double excuses for those I omit. Thanks to Laura Pellise and Miquel Nadal; Fay, Amanda, Hua and Horace Darmawi; Naomi Makins and her family; Mike Titko, Menke Ubbens, Gillian Reynolds, Ole Hansen, Robin Côté, Harald Baeder; Verónica and Claudia Sánchez-Serrantes, Gustavo Lozano, Dorothy Bisbee, Sharon Defty, Greg Barry, Knut Streitlien, Hiren Ma-

niar, Olivier Herbelot, Rosario Gennaro, Robert Kallenberg, Harald Tuerk, Thomas Kaup, Josè Duarte, Muriel Mora, Marika Santagata and family, Peter Dürr, Eric and Herb Lin, Olivier and Roman Beau-de-Loménie, Erika Kiss, Constantia Petrou, Alberto Suárez, Mauricio Barahona, Maia Engeli, Gail Bier, Marga Gómez-Reino, Antonio Ferrera, Sarah de Rocher, Uli Knirsch, Jim Ellison and the other MUNers, and also to Jackie Campbell.

I also want to aknowledge "La Caixa" for their trust, when they decided to award me the generous two-year scholarship which permitted that I came to MIT.

Finally, my deepest gratitude to my family, who have provided infinite love and encouragement from Barcelona or by visiting me in Boston. Thanks to my parents, who have understood the value of education, and especially to my mother, whose open mind and wise advice paved my way to MIT. It is to her honor that I dedicate this work.

Jordina Vidal

May 20, 1994

To my mother,

Contents

List of Figures

List of Tables

Introduction

Although the field of solid state physics experienced a very rapid growth in the 50's, it did not reach maturity until recently, when developements in both experimental and theoretical techniques permitted the microscopic study of vast ensembles of interacting particles. This thesis could not have been written two decades ago, as both the fields of short pulse lasers and of first-principles calculations were still in their infancy. The rapid improvements in lasers, in terms of producing very short pulses of light, have provided a powerful tool for studying transient phenomena which occur on a sub-picosecond time scale. Sophisticated experimental techniques using these short light pulses have been successfully applied to study the dynamics of a large variety of physical systems. On the theoretical side, the rapid increase of computational power has triggered a parallel growth in microscopic calculations in solids, using so-called first-principles (or *ab initio*) methods. Presently, first-principles calculations can predict the electronic and geometric structure of a solid by only providing the atomic number and weight of the different constituents.

In this thesis research, we analyze theoretically certain microscopic transient phenomena which have been generated and detected by means of laser pulses of about 60 femtoseconds duration! This implies that we can optically resolve processes which take place on these time scales, such as the non-equilibrium relaxation of electrons and ions in a solid. The sequence of theoretical tools employed in this work culminates in the use of state-of-the-art *ab intio* methods to study the different microscopic processes occurring on this very short time scale.

As so often happens in the field of solid state physics, this research is the result of a collaborative project between experimentalists and theoreticians. A series

of very unique experimental observations awakened our curiosity to understand the fundamental processes underlying the data. By illuminating certain narrow-gap semiconductors and semimetals with a short-pulse laser, the atoms of the lattice can be set to oscillate in phase. This *coherent* atomic vibration is fundamentally different from the thermal agitation if the lattice. In the latter, the average shift from the equilibrium coordinates of the atoms at every instant is zero. In the former, the atoms suffer temporarily a net displacement away from their equilibrium positions.

The phenomenon of generation of coherent phonons proves that time-domain optical techniques are not just a complementary tool to the more conventional frequency-domain techniques, such as spontaneous Raman spectroscopy. The challenge was then to understand the mechanism of production of the coherent atomic motions, as well as to inspect the physical implications of having a lattice oscillating in phase. The purpose of this research is precisely to meet these challenges.

The thesis is organized as follows. Chapter 1 describes the experimental technique used to obtain the optical data. We then proceed to show typical modulated reflectivity traces for some narrow-gap semiconductors and semimetals, and we outline the features which make these materials so unique. In the last part of the chapter, we explain the phenomenological model that accounts for the experimental observations.

In Chapter 2 we study the physical implications of the coherent phonon phenomenon. The experiments described in this chapter extend previous coherent phonon studies because they show, for the first time, the possibility for coupling coherent phonon dynamics to electron dynamics in the limit of large vibrational amplitudes. In addition, the examples shown give support for the general notion that it is possible to modulate the ion coordinates in a solid so as to transform the physical characteristics of the solid at terahertz frequencies.

Chapter 3 inspects, via a perturbative pseudopotential band structure calculation, whether the ultrafast laser-generated coherent phonons can induce a metal-insulator transition on a subpicosecond time scale. The study provides qualitative support for the occurrence of such a transition in Bi and Sb, although it also shows that more accurate calculations are needed to confirm our working hypothesis quantitatively.

In Chapter 4, we have performed first-principles calculations of the phenomenon of generation of coherent phonons and their subsequent evolution in time for Sb. By means of the most advanced *ab initio* techniques, we predict the magnitude of the atomic displacements along the trigonal axis produced by the short-pulse laser electronic excitation. We also evaluate the band modulations in the vicinity of the Fermi level which result from this coherent atomic displacement.

Chapter 5 presents semiempirical calculations of the decay time of the background of the transient modulated reflectivity signal, which traces the return of the excited carriers to their pre-pump equilibrium configuration via electron-phonon scattering processes. We concentrate on two systems, the $Bi_{1-x}Sb_x$ alloys and Ti_2O_3 in the vicinity of their respective metal-insulator transitions, in order to relate the dynamical behavior of the carrier decay and the band structure across these transitions.

Finally, we summarize the main results of this theoretical work and propose areas for future research.

Chapter 1

Overview of experiment and phenomenological theory

The theoretical work presented in this thesis is inspired by a series of optical experiments with short-pulse lasers developed by T. K. Cheng and co-workers [1, 2, 3, 4, 5, 6], from the Department of Electrical Engineering and Computer Science at MIT, under the supervision of Prof. E. P. Ippen. These short-pulse laser techniques allow a time-domain study of phenomena on a sub-picosecond timescale. At the present time, such short response times cannot be attained by any electronic device, which makes the ultrafast optics techniques the only existing tools to study the time-domain transient dynamics of systems on this timescale. Although these experiments are not the object of this thesis by themselves, we will summarize the basic concepts about the short-pulse laser technique, in order to follow the subsequent theoretical analysis presented in this dissertation. A complete description of the laser apparatus and experimental setup, as well as an extensive analysis of the measurements, is contained in T. K. Cheng's doctoral dissertation [6], and references therein.

In the first section of this chapter, we describe the experimental technique used to obtain the optical data. We then proceed to show typical traces for some narrow-gap semiconductors and semimetals, and we also outline the features which make these materials so unique. In Section 1.3, we explain the phenomenological model that was developed by H. J. Zeiger *et al.* [7] to account for the experimental observations.

1.1 Description of the experiment

The time-resolved optical experiments involve two apparati: a laser which produces short pulses of light, and a pump-probe setup, which manipulates the light pulses in a way that we can measure the optical response of a solid on an ultrafast time scale.

1.1.1 Generation of short pulses

The short pulses of light are obtained by means of a colliding pulse modelocked laser (CPM)[1], which consists of a cavity of length L in which there is a gain medium and a loss medium. The spectrum of a laser beam travelling back and forth in this cavity should in principle have an infinite number of cavity modes, with frequencies $nc/2L$, where n is an integer and c the speed of light. Nevertheless, because the gain and loss media are frequency-dependent, only those modes which receive enough gain to exceed the loss will resonate. Figure 1-1 shows the frequency spectrum resulting from a CPM, as well as its Fourier transform.

As can be seen in the picture, the CPM spectrum in the frequency domain has the shape of a picket fence multiplied by a broad envelope ($\Delta\nu$). If all the cavity modes have the same phase[2], the Fourier transform of the CPM spectrum results in a time domain signal characterized by a picket fence convolved with a narrow envelope ($\Delta t \approx 1/\Delta\nu$).

In addition, various glass prisms are placed outside the cavity in order to variably change the pulsewidth within a certain range. The resulting CPM output specifications are:

Center frequency: $\approx 6300\mathring{A}$

Average power: 10-50 mW

Repetition rate: $\approx$ 80 MHz

Pulse width: 50-200 fs

[1] For an overview on modelocking, see [8].

[2] This condition is fullfilled by sending a laser beam, which is of course coherent, into the cavity.

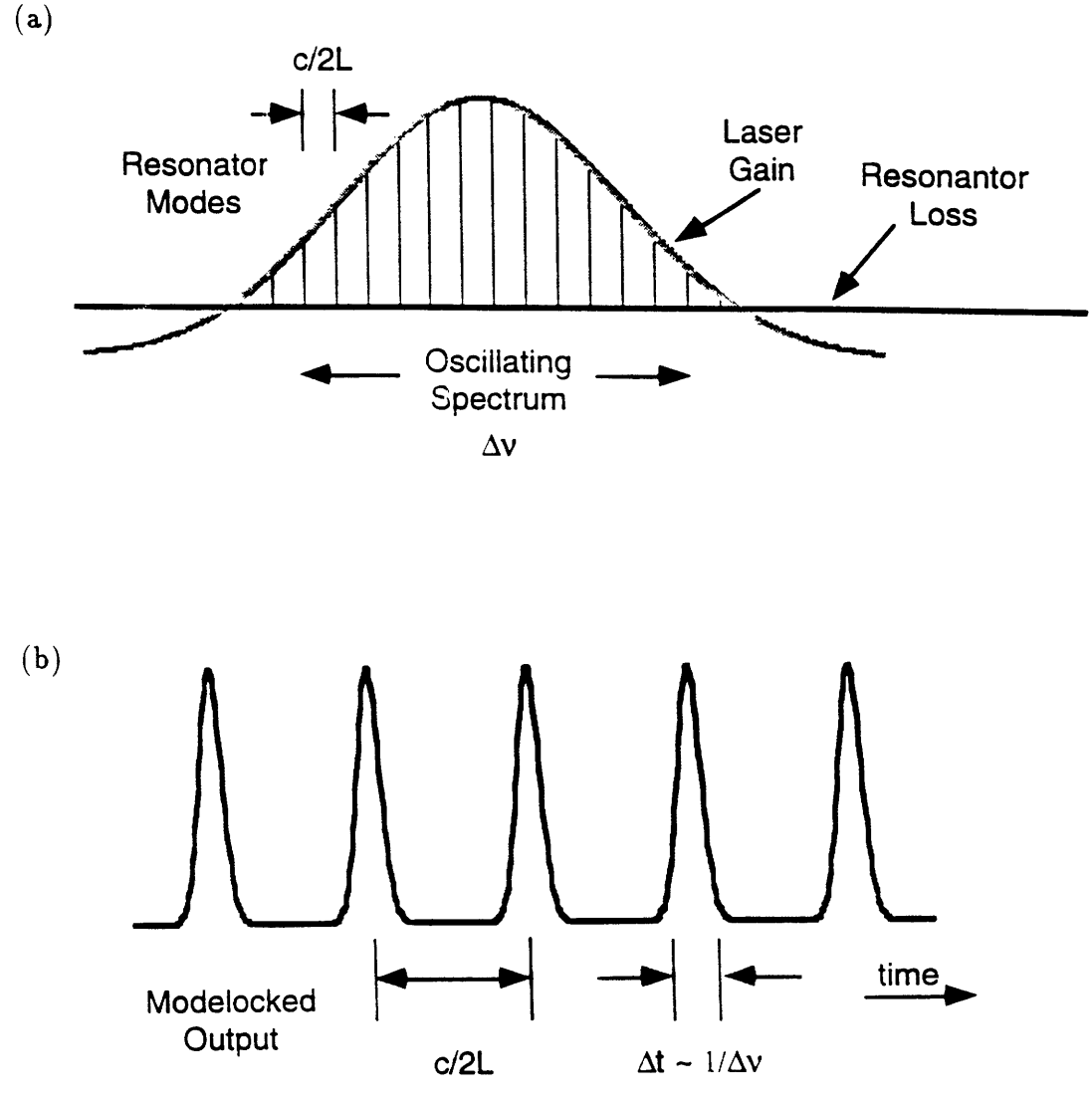

Figure 1-1: Output signal of a CPM laser with a cavity length L. (a) Frequency domain spectrum, along with the gain profile. (b) If all the phases of the modes are "locked", then the time domain ouput of the cavity is a pulse train. [6]

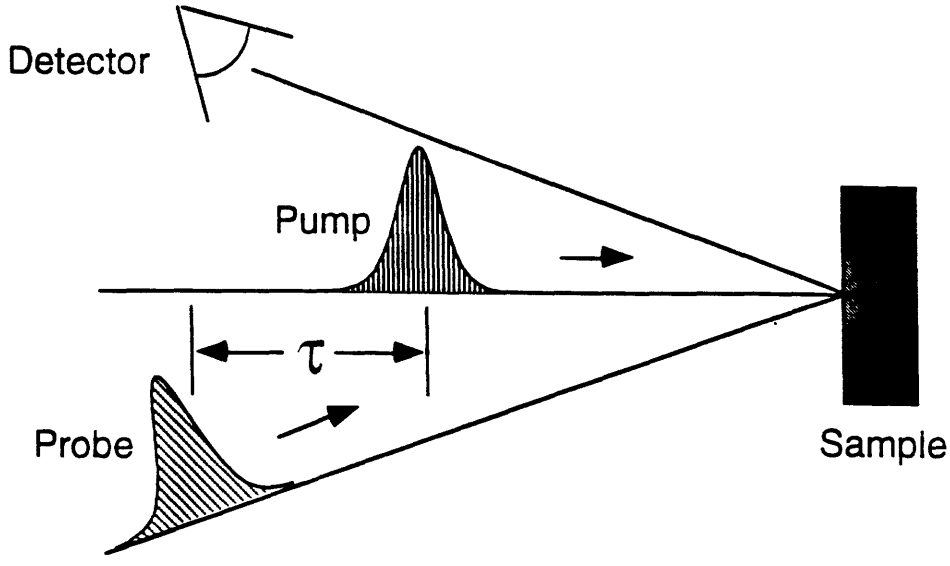

Figure 1-2: Illustration of the pump-probe apparatus. By advancing or delaying the pump with respect to the probe, we can map the changes in reflectivity induced by the pump, ΔR, as a function of time. [6]

1.1.2 The pump-probe experiment

We present in Figure 1-2 a diagram of the pump-probe technique[3], in order to facilitate its description.

The pulses produced by the CPM are split into two: the *pump*, which carries $\sim 70\%$ of the energy of the initial pulse and will provide an optical excitation to the sample, and the *probe*, which carries the rest of the energy and is used as a sensor of the pump-induced changes in the optical properties of the material.

When the pump pulse interacts with the sample, it causes the illuminated volume[4] to be temporarily excited.

By systematically varying the arrival time of the pump relative to the arrival time of the probe, we can map out the transient optical properties of the material. Since

[3] A complete description of this technique can be found in [9, 10, 11].

[4] V=area of spot size × optical penetration depth.

the CPM has a repetition rate of 80 MHz, we can only measure phenomena that relax in a time shorter than $\sim$10 ns. The variations on the arrival times are produced by changing the pathlength of one of the beams with respect to the other. This is achieved by attaching reflecting mirrors to a 0.1 mm precision stepper motor, which produces pathlength shifts as short as 0.2 mm, corresponding to a 0.67 fs time delay.

A detector measures the changes in probe intensity caused by the pump-induced optical changes in the material. The changes in the reflectivity of the sample, ΔR, are calculated by subtracting the signal detected in the absence of the pump from the signal measured when a pump pulse preceded the probe. Pump-induced changes in the reflected probe are discriminated from changes due to other sources by chopping the pump at 2 KHz, because then all the pump-induced changes will reappear at this characteristic chopping frequency. Interference effects between pump and probe are suppressed by rotating the polarization of the probe by 90° relative to the pump polarization, and adjusting the detector to uniquely register light signals polarized in the same direction as the probe polarization.

A typical pump-probe trace shows the modulated reflectivity, ΔR, as a function of time delay between pump and probe. Plotted in Figure 1-3 are characteristic pump-probe data for simple metals [12]. The main features of these traces are the sharp rise of ΔR around zero time delay, followed by a gradual decay back to its pre-pump value. The rise is due to the optical changes induced by the pump in the material, and it is typically on the order of the pulsewidth duration. The decay corresponds to the relaxation of the pump-induced excitation in the sample back to its ground state, a relaxation which takes place on a picosecond time scale.

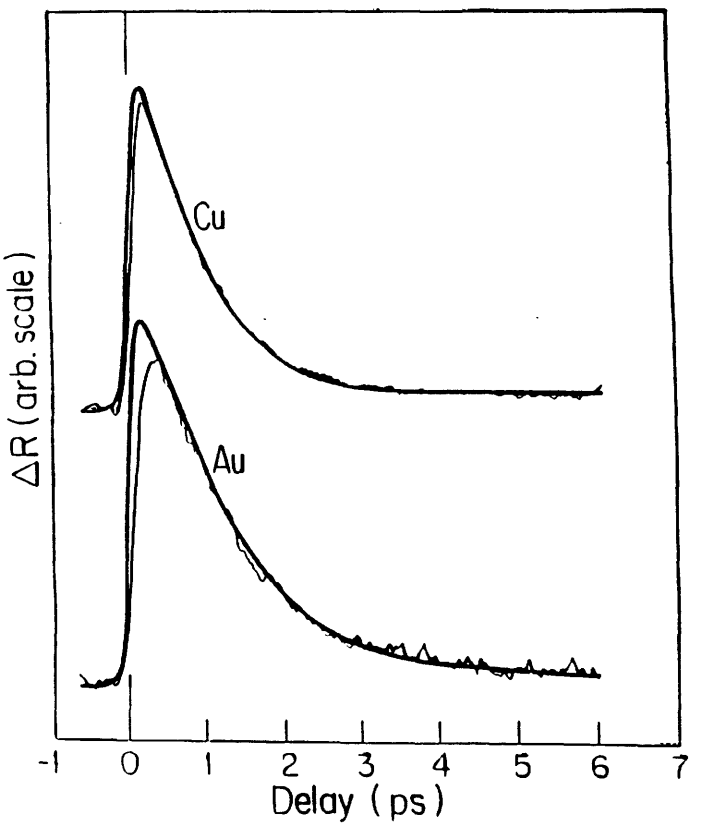

Figure 1-3: Pump-probe data for Cu and Au. [12]

1.2 Femtosecond studies of narrow-gap semiconductors and semimetals

T. K. Cheng has used the pump-probe technique to study a series of semimetals and narrow-gap semiconductors. Among them, special attention was given to the semimetals antimony (Sb) and bismuth (Bi), and the semiconductors tellurium (Te) and titanium sesquioxide (Ti_2O_3). The group V semimetals Sb and Bi crystallize in the rhomobohedral structure and have two atoms per unit cell. Titanium sesquioxide also has rhombohedral symmetry, but with two Ti_2O_3 groups per unit cell. Tellurium is a hexagonal semiconductor with three Te atoms per unit cell.

Figure 1-4 shows typical pump-probe data for Sb, Bi, Ti_2O_3 and Te. Similar to the metals, the reflectivity of these materials changes more or less sharply near zero time delay and relaxes at different rates. Notice in the figure that typical decay times of the modulated reflectivity ΔR for these materials are about several picoseconds, like for the metals.

But a new feature is observed in all these semimetals and narrow-gap semiconductors, namely, the existence of an oscillatory component superimposed on the decaying background. The amplitude of these reflectivity oscillations is particularly large (on the order of 1%), which suggests that there is a significant periodic modulation of the electronic structure of the material.

The Fourier analysis of the oscillations (see insets in Figure 1-4) shows that the frequencies correspond to the A_{1g} phonon mode in each material[5]. Furthermore, we find from the Fourier transform data that there is only one frequency of oscillation, although these materials have other Raman-active E_g modes with similar Raman intensities and frequencies. This observation is independent of the geometry of the experimental setup and the polarizations of the light beams. This very special feature of detecting only fully symmetric phonon oscillations in the ΔR trace is going to be key to understanding the mechanism for the generation of these oscillations.

[5]In Te, the mode has only A_1 symmetry, as this material is not invariant with respect to the inversion symmetry operation.

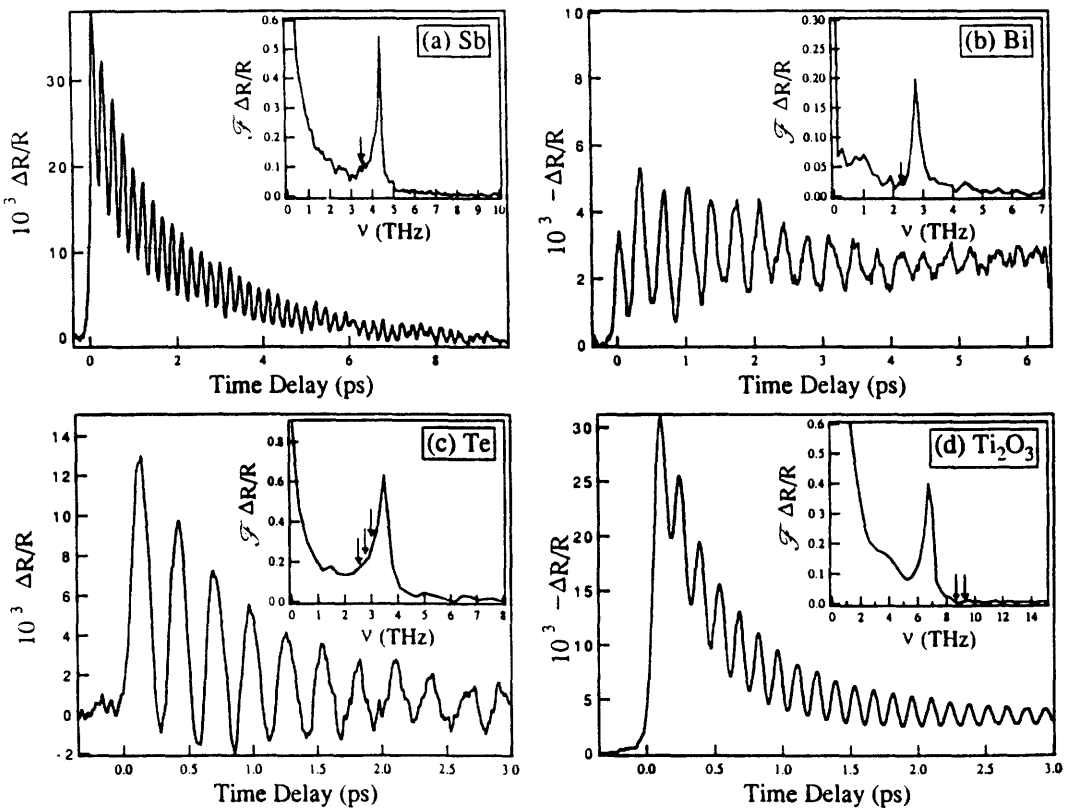

Figure 1-4: Observations of the coherent phonons in Sb, Bi, Te and Ti_2O_3 using pump-probe experiments. In each case, the Fourier transform of the pump-probe data is shown as an inset. Arrows indicate the positions of Raman-active modes which have intensities comparable to those of the A_1 or A_{1g} modes but do no appear in the Fourier-transform pump-probe spectrum. [7]

The fact that we can identify the frequency of the oscillatory component of ΔR with those of a phonon in the material, indicates that we are observing the signatures of the atoms in the lattice oscillating in phase. We will denote such lattice vibrations by the term *coherent phonon oscillations*, which are characterized by having an instantaneous net displacement of the equilibrium positions of the atoms, when averaged over the illuminated volume. This is distinct from the "incoherent" excitation of the phonons by other techniques, such as Raman, infrared or neutron scattering. These frequency-domain techniques do not produce a net average displacement of the atomic equilibrium coordinates.

Another more subtle aspect of the pump-probe data (Figure 1-4), which is different from the data for the metals (Figure 1-3), is the rise of the signal near zero time delay. In the case of the metals, ΔR reaches half of its maximum change at zero time delay. Instead, for the group of semimetals and semiconductors we have studied, the signal appears to rise later and reaches half maximum well after zero time delay. This observation will be crucial to the understanding of the mechanism for generation of coherent phonons.

The accurate determination of zero time delay is very critical in the interpretation of pump-probe data for coherent phonon materials. The basic concept behind the method to measure $t = 0$ is that the role of the pump and probe are reversed by chopping the second instead of the first. If the pump and the probe are of equal intensity, the zero time delay is determined by the intersection of the trace taken in the standard configuration and that taken with the reversed configuration (see Figure 1-5).

1.3 Displacive Excitation of Coherent Phonons (DECP)

The appearance of oscillations in the pump-probe reflectivity response has for some time been observed in organic molecules [18, 19], where they were identified with different Raman-active molecular vibrations. In more recent times, the phenomenon

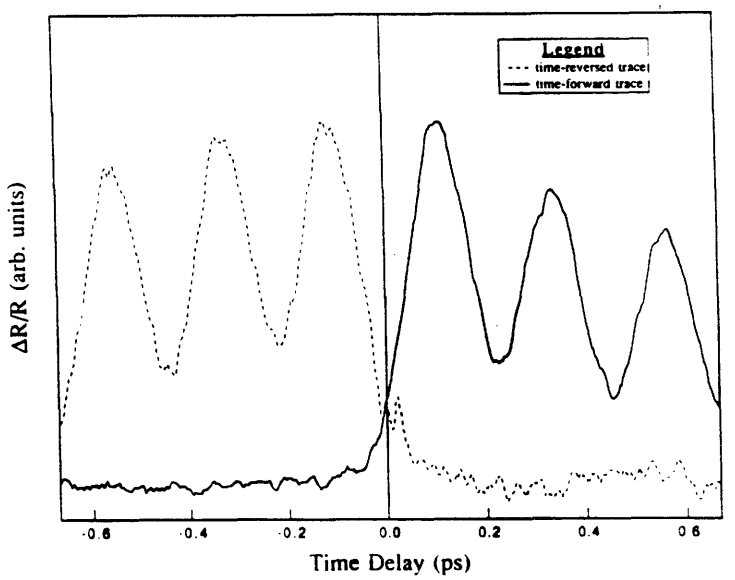

Figure 1-5: Two typical pump-probe data traces obtained by chopping the pump beam (solid trace) and the probe beam (dashed trace). Zero time delay is determined by the intersection of the two traces. [7]

of pump-probe generation of coherent phonons has been observed in studies of wide gap semiconductors, such as Ge [20] and GaAs [21], and high temperature superconductors [22]. In these systems, various mechanisms have been proposed for the generation of the coherent phonons.

Cosine-phase reflectivity oscillations have been reported in molecular systems [24], and the generation mechanism by means of an electronic excitation is referred to as resonant stimulated Raman scattering (RSRS). There are several distinctions between the coherent oscillations generated in molecules and those appearing in the small gap materials that we have studied. We postpone the comparison until we enter into a more detailed analysis of the coherent phonon phenomenon (Section 2.3). We will just mention at this point that in the conventional RSRS processes all allowed Raman-active modes are coherently generated, whereas in our materials only the fully symmetric A_{1g} (or A_1) mode is detected. The reason for observing only this mode is that the solids do not have sharp electronic levels, but rather have wide bands of allowed energy states. As a result, a laser-induced excitation can occur

at various points of the Brillouin zone, which translates into changes of the real space electronic distribution that mantain the full symmetry of the crystal. Thus, we could say that we are observing a resonant stimulated scattering process occurring in solids. Nevertheless, as we will see in Section 2.2, the fact that the collective atomic excitations in the solid are described by extended waves instead of the well localized wavefunctions defining the molecular vibrations, will have very important consequences.

The very unique feature of observing only fully symmetric modes eliminates the mechanisms proposed for the generation of coherent phonons in GaAs and Ge [21, 20] as suitable for our small-gap systems. GaAs and Ge are cubic materials which do not have a Raman-active fully symmetric mode. In those polar semiconductors, the generation of coherent phonons with a symmetry other than A_1 symmetry is believed to be due to the induction of effective dipole moments in each unit cell by the laser excitation. The sum of these dipoles builts a surface electric field on a time scale of a tenth of a picosecond which induces the coherent phonon oscillation. The slow rise of this surface field, on the same time scale as the characteristic phonon periods for these materials, allows the phonons to follow the displacement of their equilibrium positions at every instant. As a consequence, the oscillatory component of the observed ΔR is well described by a sine function. Conversely, Bi, Sb, Te and Ti_2O_3 are non-polar materials, and the pump-probe reflectivity oscillatory signal is described by a cosine.

The last type of materials where coherent phonons are observed are the high T_c cuprate-superconductors [22]. For those materials, the oscillatory component of ΔR is believed to show a cosine-dependence and, to the author's knowledge, no mechanism has yet been identified for the generation of coherent phonons.

In conclusion, the very unique features observed in our pump-probe studies of semimetals and narrow-gap semiconductors exclude any of the existing models as a potential mechanism for the generation of coherent phonons.

The phenomenological model that explains the pump-probe reflectivity data for these groups of semimetals and narrow-gap semiconductors was developed by H. J. Zeiger *et al.* [7]. We present in this section the main concepts of this phenomeno-

logical analysis. A complete description of the model can be found in T. K. Cheng's Master thesis [13], and also in [7].

In the analysis of the pump-probe data, we consider the modulated reflectivity signal, $\Delta R/R$, as a linear superposition of an electronic contribution and a coherent phonon contribution. This linear decomposition is correct in the limit of low pump excitations, that is, if the lattice temperature remains below the melting point during the experiment.

The relaxation of a pump-induced electronic excitation has been extensively studied in a large variety of materials[6] and shown to produce a monotonically decaying response of $\Delta R/R$. Added to this exponential decay is the effect of the thermal heating of the lattice, which causes the background to return to its pre-pump value on a time scale longer than the typical electronic decay time, but shorter than the time interval between the arrival of two consecutive pump pulses. The coherent phonon contribution is easly identifiable because of its oscillatory nature. As we will see later, there is also a decaying background associated with the phonon response, due to the coupling between the phonon and electronic systems.

Figure 1-6 shows schematically the decomposition of ΔR into the different contributions, which we proceed to analyze in more detail.

The electronic dynamics can be modeled via a linear rate equation, which results in the characteristic exponential solution with a decay rate $\beta = 1/\tau_{el}$:

$$\left(\frac{\Delta R}{R}\right)_{background} = A \cdot e^{-t/\tau_{el}}. \tag{1.1}$$

The slow decay of the lattice heating is detected as a constant overall shift of the background, C, on this picosecond time scale.

The coherent phonon dynamics can be modelled by a harmonic oscillator equation, for small atomic displacements from the equilibrium position. If we consider the action of the pump pulse as a driving force $F(t)$, we obtain the equation of motion for a

[6] See, for example, [12].

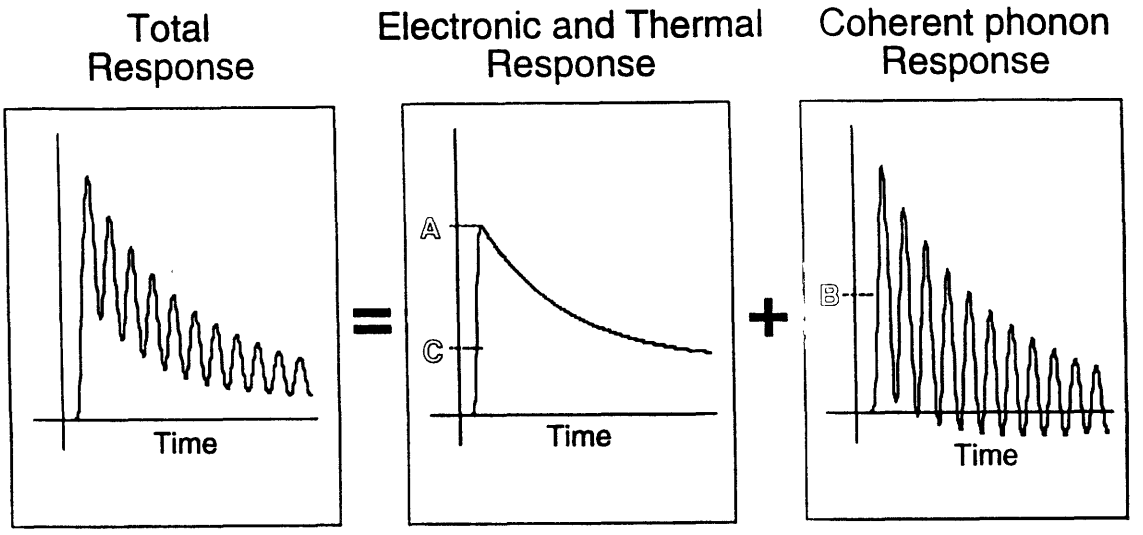

Figure 1-6: Phenomenological separation of the pump-probe reflectivity into various contributions. A denotes the maximum rise of the background, C is the thermal background and B is the midpoint of the oscillatory component after the arrival of the pump. [6]

given phonon mode as [23]

$$\rho[\ddot{Q}(t) - 2\gamma\dot{Q}(t) - {\omega_0}^2 Q(t)] = F(t), \tag{1.2}$$

where ρ is the reduced mass of the phonon, Q the phonon coordinate, γ the effective damping of the coherent oscillation through different scattering processes, and ω_0 is the angular frequency of the phonon.

The forcing term, $F(t)$, depends on the electric field created by the pump pulse. A phonon mode of frequency ω_0 can be generated only if the frequency bandwith of the pulse is larger than ω_0. In that case, a term of the type $F_i(w) \cdot exp(\omega_0 t)$ will be present in the Fourier transform of F(t), which will resonate with the phonon normal mode [23][7].

If $F(t)$ is described by a delta function centered at zero time delay, the solution

[7]Coherent oscillations with frequencies larger than the laser bandwith can also be generated by using two or more pumps, with frequencies which differ by some normal frequency of oscillation for the system. Such a technique has been extensively used by Nelson and co-workers for the study of stimulated Raman scattering processes of dyes and molecular solids. [18, 19].

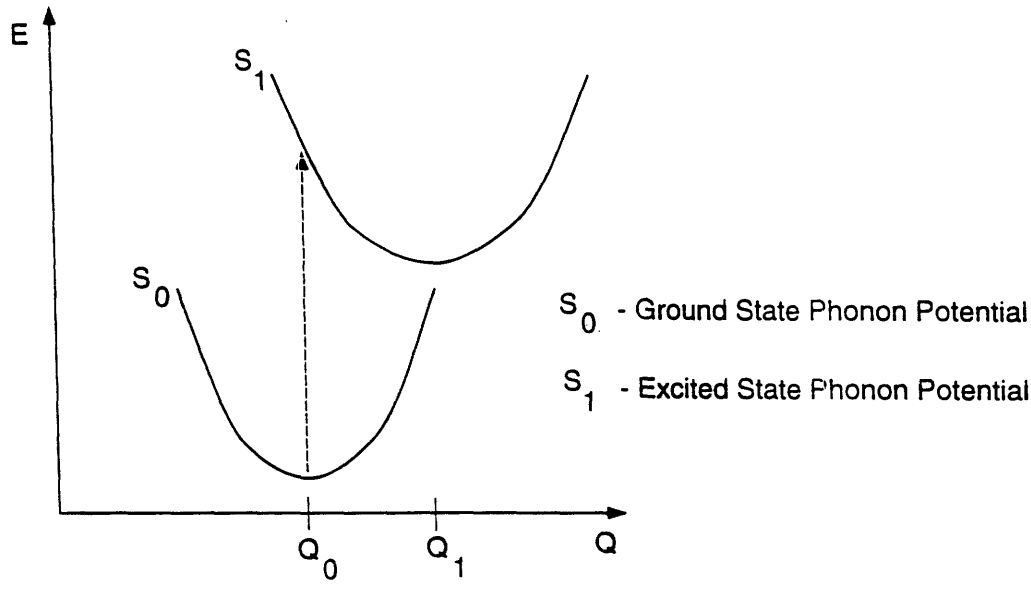

Figure 1-7: Schematic representation of the displacive excitation mechanism. [6]

of equation (1.2) is

$$Q(t) = B \cdot e^{-t/\tau_{ph}} sin\omega_0 t, \tag{1.3}$$

with $\tau_{ph} = \gamma^{-1}$, and where the sine dependence of $Q(t)$ indicates that the atom has not moved at zero time delay, but has acquired an instantaneous velocity due to the laser impulse.

We showed in the previous section (Figure 1-5) that the oscillatory component of the reflectivity response for the materials under study was maximally displaced from the midpoint of the oscillation at zero time delay. This indicates that the phonon motion is best described by a cosine function rather than a sine.

The situation described by equation (1.2) and its solution (1.3) arises when a coherent oscillation is produced without modification of the electronic population, which remains in the ground state. These sine-dependence oscillations are readily observed in non-resonant Raman scattering experiments. Both in solids and molecular systems, if the laser excitation acts on the electrons, the change of the electronic population results in a new potential which determines a new equilibrium coordinate for the ions. We call this generation mechanism *displacive excitation of coherent phonons* (DECP) (see illustration in Figure 1-7). Due to the large difference in the masses of electrons and ions, these electronic changes appear to be instantaneous on

the typical time scale of the ion dynamics. Thus, we still have to impose the boundary condition that the atoms have not yet moved at $t = 0$. The equation that properly describes the generation of coherent phonons in an excited electronic state is then,

$$\rho[\ddot{Q}(t) - 2\gamma\dot{Q}(t) - {\omega_0}^2(Q(t) - Q_0(t))] = F(t), \tag{1.4}$$

where $Q_0(t)$ is the time-evolving equilibrium coordinate of the ions due to the effect of the electronic excitation, and $Q_0(t)$ will therefore have the functional form:

$$Q_0(t) = Q_0(0) \cdot e^{-t/\tau_{el}}. \tag{1.5}$$

The solution of equation (1.4) is

$$\begin{aligned} Q(t) &= Q_0(t) - Q_0(0) \cdot e^{-t/\tau_{ph}} cos\omega_0 t & (1.6)\\ &= Q_0(0) \cdot (e^{-t/\tau_{el}} - e^{-t/\tau_{ph}} cos\omega_0 t) & (1.7) \end{aligned}$$

which verifies that the atoms have not yet moved at $t = 0$, but describes the oscillation as a cosine.

The changes in reflectivity induced by the coherent phonons are then:

$$\begin{aligned} \left(\frac{\Delta R}{R}\right)_{oscillations} &= \frac{1}{R}\frac{\partial R}{\partial Q}\Delta Q = \frac{1}{R}\frac{\partial R}{\partial Q}(Q(t) - Q(0)) & (1.8)\\ &= B \cdot (e^{-t/\tau_{el}} - e^{-t/\tau_{ph}} cos\omega_0 t). & (1.9) \end{aligned}$$

Finally, adding together the background (eq. (1.1)), the coherent phonon contribution (eq. (1.8)) and the effect of the lattice heating, we obtain:

$$\left(\frac{\Delta R}{R}\right)_{pump-probe} = A \cdot e^{-t/\tau_{el}} + B \cdot (e^{-t/\tau_{el}} - e^{-t/\tau_{ph}} cos(\omega_0 t + \phi)) + C \tag{1.10}$$

in which the coefficients A, B and C indicate the contribution of each process to $\Delta R/R$, and ϕ measures the departure of the oscillatory component from the perfect cosine behavior.

Table 1.1: Values of fitting parameters for the DECP model and literature Raman data.

	Pump-Probe Data			
Material	A	B	C	ϕ (degrees)
Sb	$+2.5 \times 10^{-3}$	$+2.7 \times 10^{-2}$	-2.2×10^{-5}	$+3 \pm 4$
Bi	-4.6×10^{-3}	$+3.1 \times 10^{-3}$	-1.3×10^{-3}	-13 ± 13
Te	-6.6×10^{-3}	$+1.4 \times 10^{-2}$	$+3.2 \times 10^{-4}$	$+7 \pm 9$
Ti_2O_3	$+2.6 \times 10^{-2}$	-5.7×10^{-2}	-3.7×10^{-3}	-20 ± 10

	Pump-Probe Data			Raman Data	
Material	τ_{el}[a] (ps)	τ_{ph}[a] (ps)	$\omega_0/2\pi$ (THz)	$\omega_0/2\pi$ (THz)	τ_{ph} (ps)
Sb	1.67	2.90	4.5 ± 0.1	4.50[b]	2.4
Bi	10.3	2.41	2.9 ± 0.1	2.94[b]	3.0
Te	0.63	1.26	3.6 ± 0.1	3.61[c]	2.4
Ti_2O_3	0.40	1.59	7.0 ± 0.1	7.14[d]	1.3

[a] Values for relaxation time are accurate within 10%.
[b] Ref. [14].
[c] Ref. [15].
[d] Ref. [16].

We present in Table 1.1 the values of the different DECP parameters fitted to the pump-probe data shown in Figure 1-4.

1.4 Conclusions

We observe large amplitude oscillations in the time domain reflectivity response for Sb, Bi, Te and Ti_2O_3 by means of the pump-probe technique. The oscillations have the frequency of the fully-symmetric A_{1g} phonon mode of the system and are maximally displaced from their midpoint value at zero time delay between pump and probe. These features indicate that coherent phonons are generated in these materials via an electronic excitation at different points of the Brillouin zone, which displaces the equilibrium positions of the atoms.

Chapter 2

Coherent phonons

In this chapter, we analyze the physical implications of having a lattice oscillating in a coherent fashion. We first give a brief overview of the dielectric response as a probe of the microscopic behaviour of the material. Then we compare the pump-probe techniques with other optical measurements, with a special emphasis on those features which make the time-domain techniques unique. We will see that the coherent phonon phenomenon permits the study of the phonons in an electronic excited state, as well as their evolution as the system relaxes back to the ground state. In addition, some considerations about the response of the bands to such coherent lattice displacements are addressed. In the remainder of the chapter, we explain the experimental work and physical interpretation of the various consequences of having coherent phonons.

2.1 The dielectric response

Solids have been traditionally described as an ensemble of nuclei and electrons. The macroscopic properties of the solid could then be obtained through the diagonalization of the Hamiltonian for this system of $\sim 10^{23}$ particles. In the 60's, Pines [43] presented an alternative description of the solid as a gas of elementary excitations. Within this framework, he defined two kinds of excitations:

1. Quasi-particles, which resemble the real constituent particles. These are usually fermions, and a typical example is the electron.

2. Collective excitations, which are collective motions of many particles. These are usually bosons, and phonons are an example of them.

The study of the solid is performed via probing these excitations and studying the response function, $R(\omega)$. If $I_i(\omega)$ is the the input probe, and $I_o(\omega)$ describes the output signal, linear response theory tells us that:

$$I_o(\omega) = R(\omega)I_i(\omega), \tag{2.1}$$

where $R(\omega)$ does not depend on the probe, but only on the properties of the solid.

Therefore, in this approach, the microscopic and macroscopic behaviors of the solid are connected via the response function $R(\omega)$. The process of calculating $R(\omega)$ consists of the following steps: 1) define the elementary excitations within a Hamiltonian formalism, 2) solve the corresponding dispersion relations, 3) evaluate the appropriate matrix elements and 4) calculate the response functions.

An example of such functions is the dielectric response, $\epsilon(\omega)$, which contains information on how the material reacts to an external electric field. $\epsilon(\omega)$ has contributions from the cores (nuclei plus valence electrons) and the conduction electrons. A general expression for $\epsilon(\omega)$ is[1]:

$$\epsilon(\omega) = \epsilon_{core}(\omega) + \frac{4\pi i\sigma(\omega)}{\omega} + \frac{4\pi^2 e^2 i}{\omega}\int \frac{d\vec{k}}{(2\pi)^3}\Sigma_{n,n'} D_{nn'}(\vec{k})\delta\Big(\frac{\mathcal{E}_n(\vec{k}) - \mathcal{E}'_n(\vec{k})}{\hbar} - \omega\Big), \tag{2.2}$$

with

$$D_{nn'}(\vec{k}) = \frac{f(\mathcal{E}'_n(\vec{k})) - f(\mathcal{E}_n(\vec{k}))}{\mathcal{E}_n(\vec{k}) - \mathcal{E}'_n(\vec{k})}\frac{1}{3}\Sigma_i| < n\vec{k}|v_i|n'\vec{k} > |^2. \tag{2.3}$$

In equation (2.2), the first, second and third terms on the right hand side correspond, respectively, to the core, free electron and interband contributions to the dielectric function $\epsilon(\omega)$, and $\sigma(\omega)$ is the conductivity. In (2.3), $f(\mathcal{E}_n(\vec{k}))$ is the Fermi-Dirac distribution for electrons at the n^{th} band with eigenenergy $\mathcal{E}_n(\vec{k})$, and $| < n\vec{k}|v_i|n'\vec{k} > |^2$ is the square of the matrix element for optical transitions between

[1]See Ashcroft and Mermin [44], Appendix K, pp. 776-779.

bands n and n', at wavevector $\vec{k}$.

The fraction of power reflected, or the reflectivity, is then defined as:

$$R = \left|\frac{1-\kappa}{1+\kappa}\right| = \frac{(1-n)^2+k^2}{(1+n)^2+k^2} \tag{2.4}$$

where

$$\kappa = \sqrt{\epsilon}, \qquad n = Re\ \kappa, \qquad k = Im\ \kappa. \tag{2.5}$$

In a reflectivity experiment, all the contributions to $\epsilon(\omega)$ are evaluated by shining light on a sample with an incident beam and measuring the reflected light. If one of the contributions is much larger than the others, the dominant term buries any information about the system contained in the smaller terms.

A way to get around this problem is by measuring the modulated reflectivities, $\Delta R/R$, instead of the absolute value. $\Delta R/R$ can be obtained in a variety of experiments where some external field is applied to the material, and one measures changes in R produced by changes in the applied field. As an example, we present in Figure 2-1 a plot of the data for a piezoreflectance experiment in Bi, where the changes in reflectivity caused by imposing pressure on the material are measured as a function of the reflected light frequency [46].

The figure shows two important points, which characterize any modulated reflectivity experiment:

1. Large changes in $\Delta R/R$ at a certain ω are associated with relative shifts between bands separated by an energy $\hbar\omega$. In other words, the modulated reflectivity is strongly coupled to measurements of changes in the interband contribution to $\epsilon(\omega)$, changes which are produced by the departures of the lattice and electronic distributions from equilibrium, as an action of the external field.

2. The magnitude of the reflectivity changes is typically very small.

In the piezoreflectivity experiment, when stress is applied to the Bi sample, the lattice is distorted in a way which shifts bands which were at ~ 2 eV separation, as the peak at this frequency indicates.

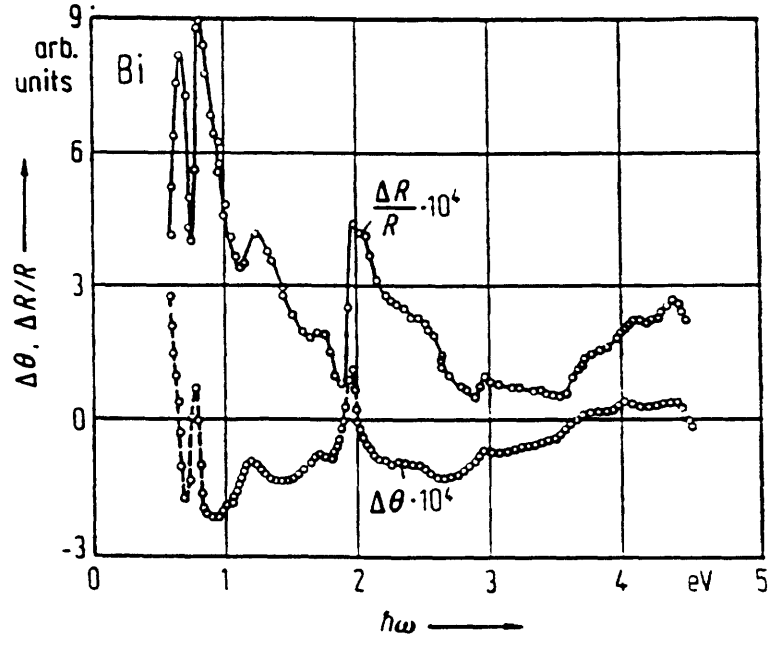

Figure 2-1: Piezoreflectance $\Delta R/R$ in Bi vs. photon energy. The change of the phase angle $(\Delta\theta)_{11}$ calculated with Kramers-Kronig relations is also shown. RMS-values of the stress components in the basal plane of the sample are estimated to be $X_{11} = X_{22} = 1.2 \cdot 10^8$ dyn/cm^2. $\Delta R = R(p) - R(p = 0)$. [46]

The transient modulated reflectivity experiments provide another example of such techniques. In a traditional pump-probe experiment for a metal, $\Delta R/R$ measures changes in the reflectivity produced by the electric field of the pump, changes that decay exponentially with time.

In our particular case, the oscillatory signal superimposed on the decaying background contains a new piece of information: it is measuring the relative band shifts between occupied and unoccupied bands separated by 2 eV, as a function of the A_{1g} phonon field.

In the next section we will analyze the implications of the observation of such a unique phenomenon in solids.

2.2 Time versus frequency domain experiments

It is precisely the generation of coherent phonons that makes the time-domain technique distinct from conventional frequency domain techniques such as Raman and inelastic neutron scattering.

In the previous chapter we described the features of the coherent phonon generation in narrow gap semiconductors and semimetals which made this phenomenon distinct from other time-domain techniques which observed collective oscillations. In this chapter, we want to concentrate on the consequences of generating collective oscillations in a narrow-gap solid.

An immediate outcome of having phonons generated through an electronic excitation is that we can study phonons when the system is not in its ground state. This phenomenon leads to a direct investigation of two interaction processes between the carriers and the phonons:

- The mechanism of generation of coherent phonons, via changes in the electronic distribution caused by the laser.
- The dynamics of the phonons as the system relaxes back to its ground state.

The next section will be devoted to experiments designed to better understand these two processes. The purpose of the study is solely to gain a fundamental understanding of the interactions between different excitations in a solid. No application has yet been identified.

The creation of coherent phonons is not connected to the specific transport properties of the material. A proof of this statement is the experimental detection of coherent phonons in various types of materials other than narrow gap semiconductors and semimetals, including wide gap semiconductors (Ge [20], GaAs [21]) and superconductors (high T_c cuprates [22]). Nevertheless, a very interesting physical consequence arises from setting the lattice of a narrow-gap material into a coherent oscillation: If the lattice motion produces large band shifts in the vicinity of the band gap, the sign of the gap could be reversed at each cycle of the oscillation.

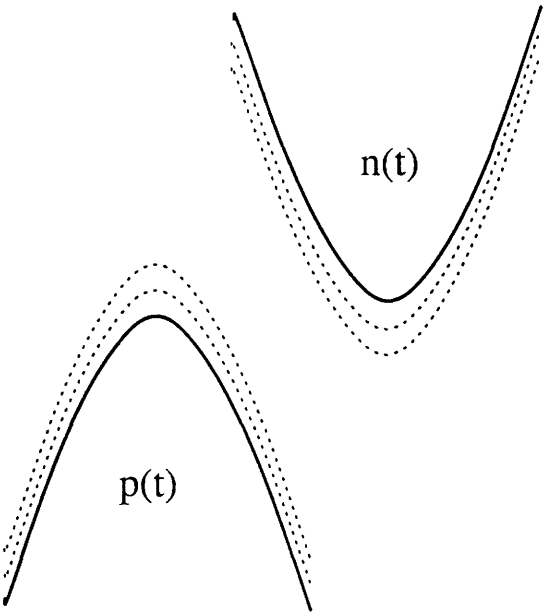

Figure 2-2: Schematic representation of an indirect band gap modulation at a THz frequency.

If the carriers could scatter fast enough to follow the band modulation, these materials would undergo a metal-insulator transition on a time scale of the phonon period. We will analyze this hypothesis in Section 2.4. If this hypothesis proves to be correct, a direct application of the phenomenon would be the creation of electronic devices operating at a frequency of several THz[2]. A discussion of the applications of the coherent phonon phenomenon is included in T. K. Cheng's doctoral dissertation [6].

2.3 Power-dependent study of coherent phonons

Before we proceed to the description of the experiments and the analysis, it is important to outline which features we may expect in the data, if the mechanism of generation of coherent phonons has indeed a displacive nature. We will better identify these features by comparing the DECP mechanism with the resonant stimulated Raman scattering (RSRS) processes occurring in molecular systems (see Section 1.3).

[2]The fastest switches known at the present time have frequencies on the order of 100 GHz [61].

Although both processes involve the generation of coherent phonons in an excited electronic state, there are some fundamental differences between these processes due to the distinct nature of the systems involved.

In molecular systems, right after the arrival of the pump pulse, the laser-induced electronic excitation causes the particles to oscillate in phase. However, after electronic dephasing occurs, the electrons occupy well-defined electronic eigenstates of the molecules. We can then observe oscillations in both ground and excited electronic states. When the intensity of the pump increases, and after electronic dephasing occurs. the fraction of molecules vibrating in the excited state rises, which results in a larger amplitude of the ΔR oscillations.

Conversely, the periodic and highly interacting nature of the solids prevents the spacial localization of the pump-induced oscillation. The coherent phonons in solids can be understood as extended collective excitations. Consequently, the increase in pump power results in an overall increase in the amplitude of the extended phonon wavefunction. If the excitation is such that it produces a displacement of the vibrational centers, we may expect a linear increase of the atomic displacement with increasing pump power.

Although the signature to be expected in the experiments with the two systems is the same, namely, a linear increase of the amplitude of the reflectivity oscillations with pump power, the physical implications are fundamentally different. Therefore, any viable microscopic model which attempts to describe the DECP mechanism should predict this linear dependence of the atomic displacement with pump intensity.

A second distinction between both systems is the nature of the electronic energy levels. Molecules have very sharp electronic levels, resulting in long lifetimes of the electrons in such states. Pump-probe experiments with molecular systems show that the lifetime of a laser-induced electronic excitation is much longer than the relaxation time of the coherent molecular vibration. Therefore, the oscillations generally die out before the electrons return to their ground state.

In the case of solids, the fact that there are oscillations in ΔR well after the background has returned to its pre-pump value (see Figure 1-4) indicates that the

coherent phonon lifetimes are longer than those of the electronic excitation. Therefore, the generation of coherent phonons in solids permits us to observe the evolution of the lattice vibrations during the process of relaxation of the electronic system.

In high power experiments with narrow-gap semiconductors and semimetals, we may expect to observe an initial shift of the phonon frequency, followed by a return to the pre-pump value. These signatures would be different for the high power pump-probe experiments with molecules, where only the shift of frequencies can be observed, but without subsequent relaxation. Again, a theoretical model for the time evolution of the electron-phonon coupled system in our solids will have to reproduce this signature in the frequency.

We have thus seen that power-dependent pump-probe experiments in narrow-gap semiconductors and semimetals will improve our understanding of the interaction between carriers and phonons. When the pump power is raised, so is the population of excited carriers increased. The dependence on power of the amplitude and frequency of the modulated reflectivity oscillation, immediately after the arrival of the pump, will provide information on the mechanism of excitation of coherent phonons. By studying the relaxation of the amplitude and frequency as the excited carrier population returns to the ground state, we can better understand the screening mechanism acting on the coherent phonons.

2.3.1 Experimental results

We will summarize the experimental data used as a source for our theoretical study of the various empirical phenomena. An extensive overview of those experiments can be found in T. K. Cheng's doctoral dissertation [6].

Power-dependent time-resolved experiments were performed for Sb using the standard pump-probe setup. The pulses, with a duration of 60 fs and an energy of 2 eV, are incident on the sample at an 80 MHz repetition rate. An amplifier allowed for variations of the pump power from 2 mW to 24 mW, a range of pump powers which corresponds to energies per pulse extending from 25 pJ to 300 pJ. Figure 2-3 presents the traces for the modulated reflectivity ΔR obtained at different pump powers.

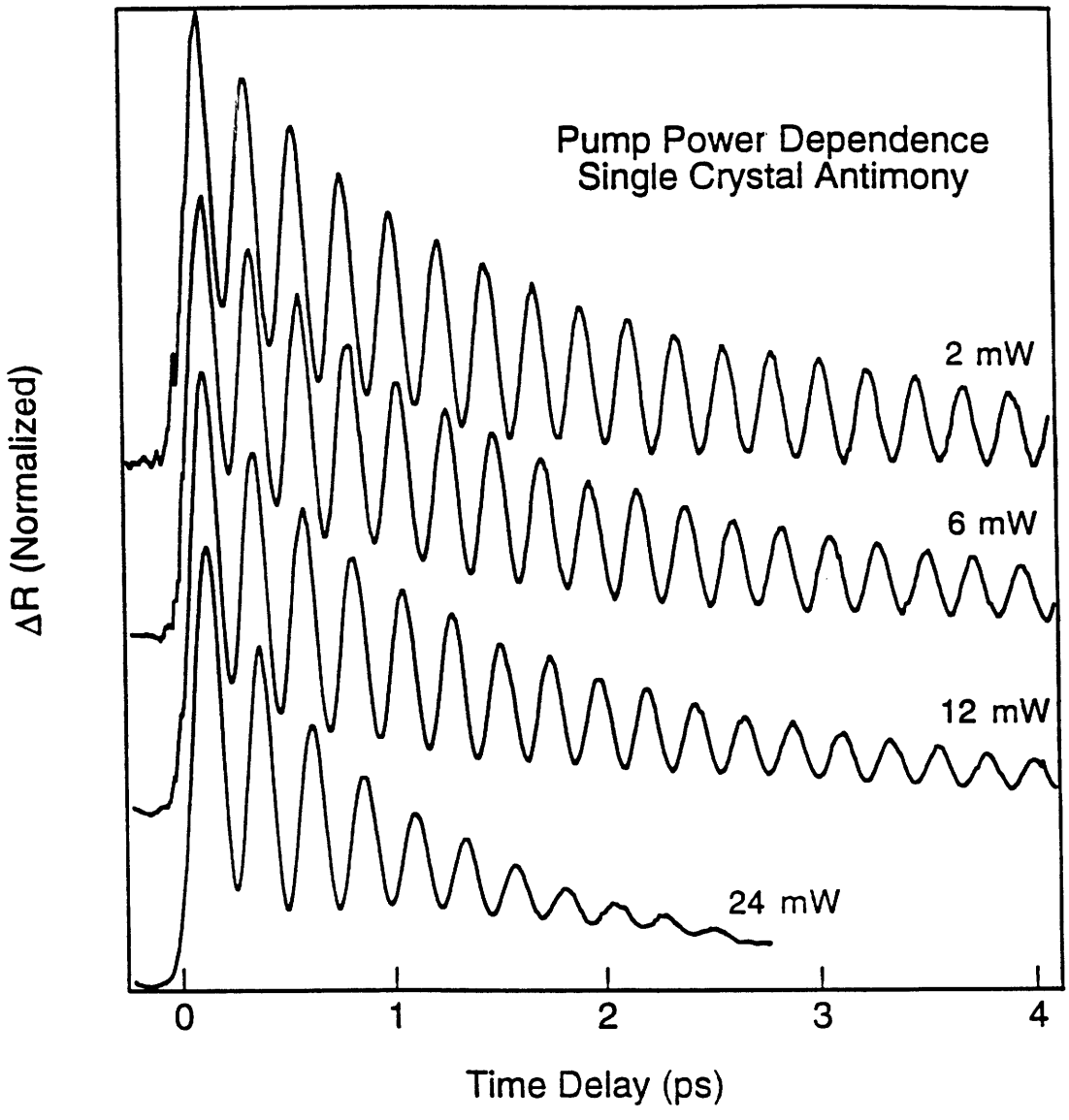

Figure 2-3: Power dependence for transient reflectivity measurements in single crystal Sb. The pump power was varied by an order of magnitude from 2 mW to 24 mW. The traces at each power level have been normalized to unity to facilitate comparison of the data. [6]

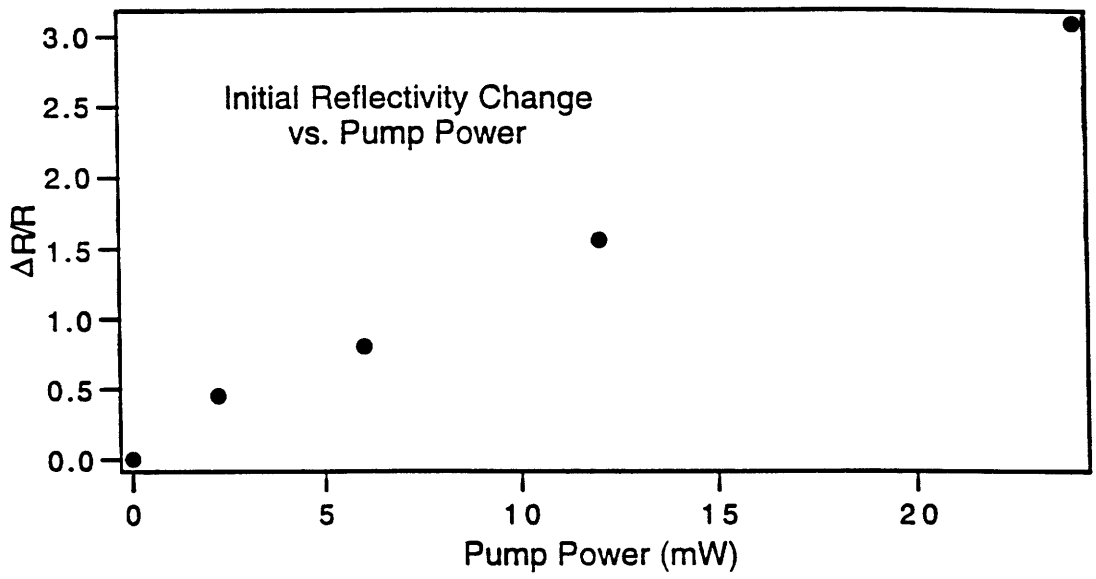

Figure 2-4: Plot of the magnitude of the initial reflectivity change in single crystal Sb. The data suggest that the coherent phonon amplitude is linearly proportional to the pump intensity. [6]

The first part of the analysis is connected with the phonon generation process. For this purpose, the values of the initial amplitude and frequency of the oscillatory component of ΔR have been extracted from the data and plotted as a function of the pump power (Figures 2-4 and 2-5).

The second part of the experimental analysis is associated with the relaxation process. We present in Figures 2-6, 2-7 and 2-8 the decay constants for the amplitude damping, the frequency changes and the background relaxation, respectively, as a function of pump power.

2.3.2 Discussion

The zero-time analysis (Figures 2-4 and 2-5) reveals two important facts:

- Both the amplitude and frequency shifts depend linearly on the pump powers, for values up to 24 mW. This indicates that we are still working in the harmonic regime.

- The initial frequency shifts are negative and can be as large as 9%, for a pump power of 24 mW.

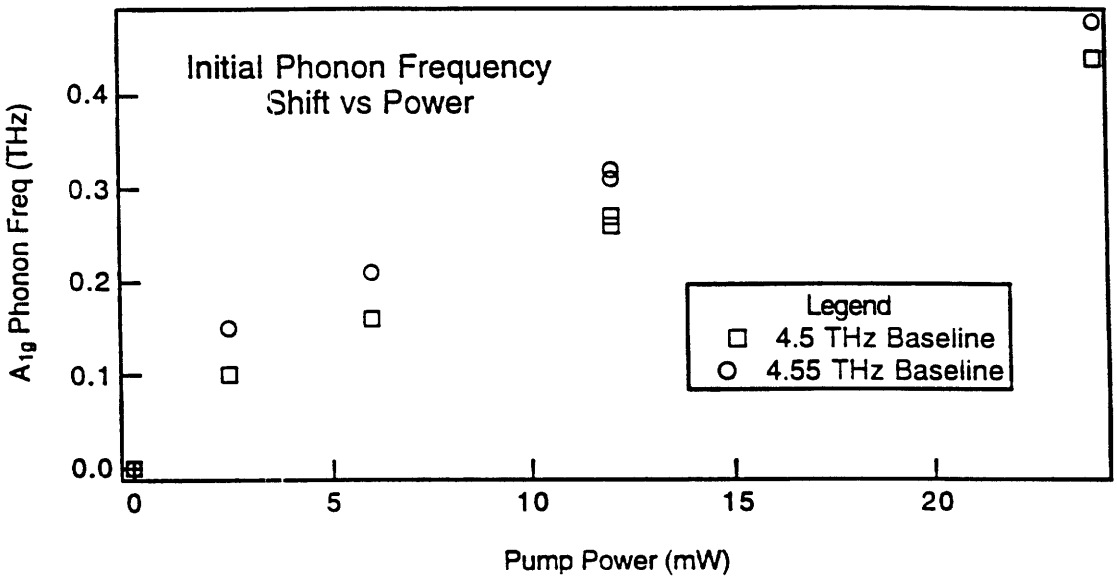

Figure 2-5: Plot of the initial frequency shifts near zero time delay versus pump power for single crystal Sb. The values were obtained by fitting the instantaneous frequencies of the coherent phonons to an exponential decay and extracting the maximum frequency shift at zero time delay. Because the oscillation frequencies appear to recover to 4.55 THz for low power levels, we have also indicated the hypothetical frequency shift, if the baseline frequency were to return to 4.55 THz instead of 4.5 THz. [6]

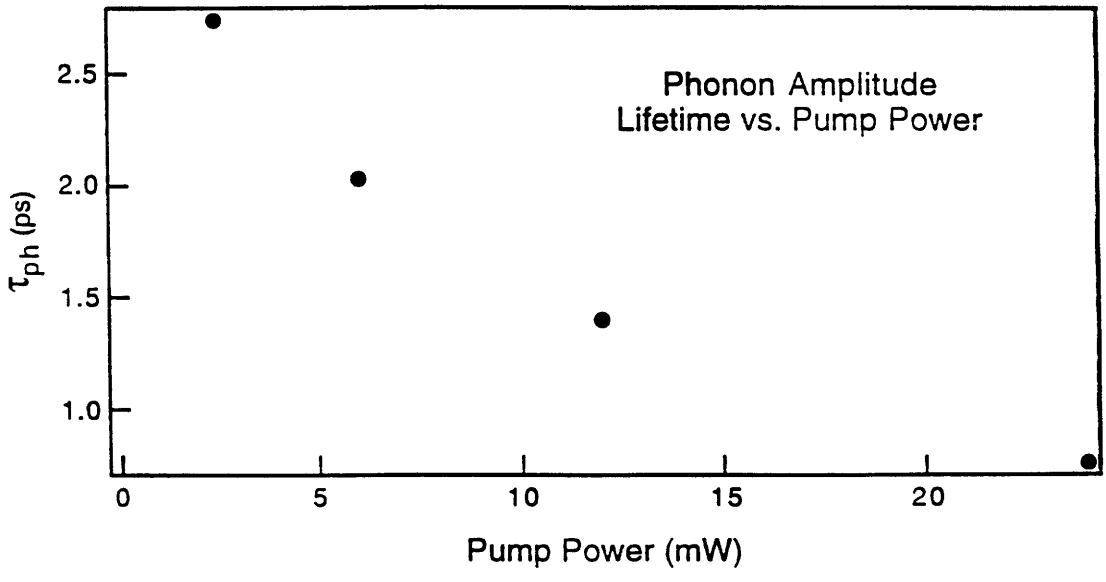

Figure 2-6: Plot of the coherent phonon lifetime ($\tau_{ph} = 1/\gamma$) versus pump power for single crystal Sb. The data indicate that the phonon becomes severely damped as the pump excitation intensity is increased. [6]

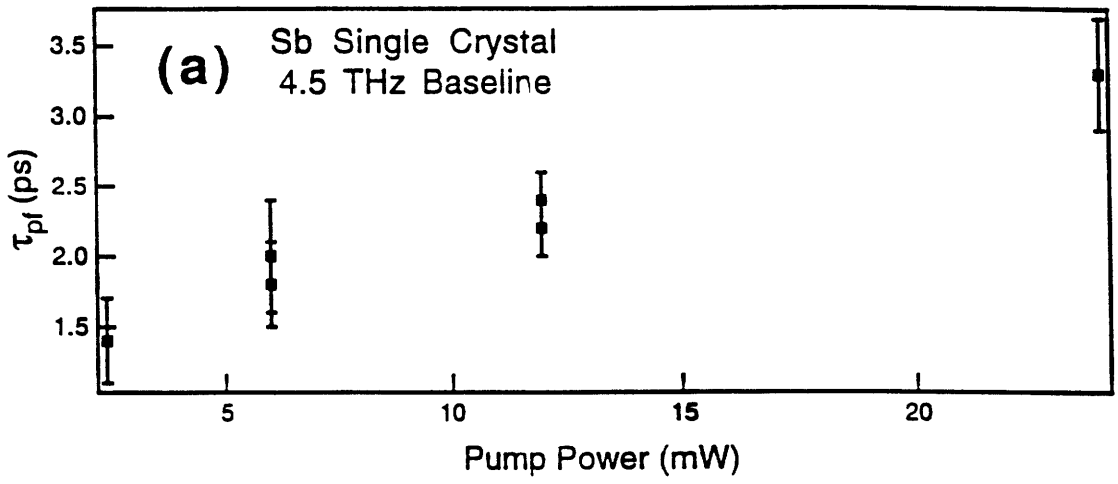

Figure 2-7: Plot of the fitted decay time τ_{pf} for the transient phonon frequency to return to its spontaneous Raman value. [6]

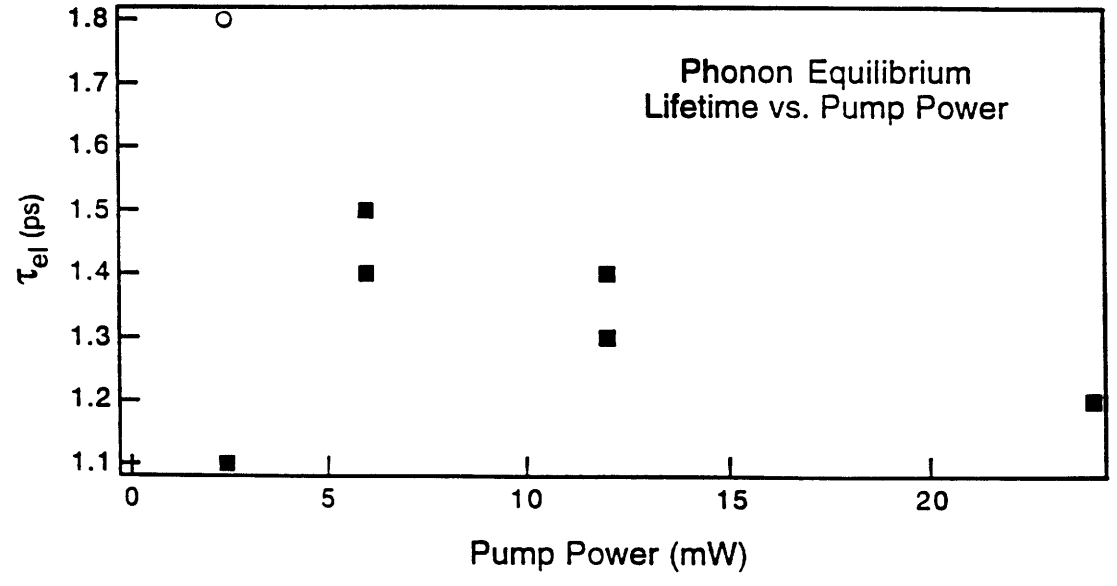

Figure 2-8: Fitted decay time τ_{el} of the equilibrium point of the reflectivity oscillations versus pump power. The dark squares represent data collected together in one day. It is disturbing that the decay time for the lowest power is only 1.1 ps. Previous low-power data typically gave $\sim$ 1.8 ps for this value (as indicated in the open circle). Unfortunately, only one trace was taken at this power level. [6]

Any theory which attempts to model the mechanism for generation of coherent phonons will have to reproduce these features.

In addition, we observe substantial differences between the time evolution of the background reflectivity data and of the oscillatory component. Namely:

- The amplitude of the oscillation amplitude decays faster than the background, and both decay times decrease with increasing values of the pump power.
- Conversely, the decay time of the phonon frequency back to its Raman value increases with increasing pump power.

Such experimental evidence shows that any simple model which directly links the phonon dynamics to the decay of the background is inadequate. Moreover, the fundamentally distinct behavior of the decay of the background and the frequency shift of the phonon oscillation eliminates vibrational anharmonicities as an explanation for the time-dependent phonon behavior. If higher-order terms in the ion Hamiltonian were responsible for the frequency shifts, the time for the frequency to recover to the spontaneous Raman value would be the same as that for the background, which traces the return of the ions to their ground state equilibrium position.

These data point to a complex screening mechanism as a potential candidate to account for the time-evolution of the different parameters associated with the coherent phonons.

2.4 The metal-insulator transition hypothesis

Both the $Bi_{1-x}Sb_x$ and Ti_2O_3 systems, in the regions where metal-semiconductor transitions occur, are very well suited for testing our hypothesis. The existence of a very narrow band gap, combined with the typically high density of carriers excited by the laser pump[3], leads to the possibility that the coherent phonons induce a modulating semimetal-semiconductor transition at a THz frequency. The dynamics

[3]As we will see in later calculations, the laser can excite as many as $\sim 10^{-20}$carriers/cm^{-3}.

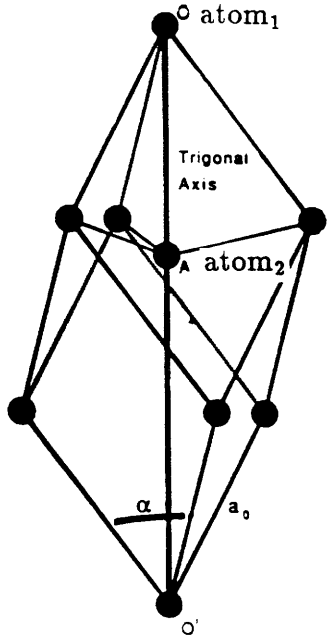

Figure 2-9: Primitive unit cell for the arsenic structure. If we set the origin at one of the two atoms (marked O), which we refer to as atom$_1$, then atom$_2$ is placed on the trigonal axis at A, z_0 away from atom$_1$ (see Table 2.1 for the values of the different lattice parameters).

of this transition can be studied with the varying probe delay as the material relaxes back to the pre-pump state.

2.4.1 Bi-Sb system

Metal-insulator transitions in $Bi_{1-x}Sb_x$ alloys

The group V semimetals crystallize in the arsenic or A7 structure, which consists of a rhombohedral lattice with two atoms per unit cell (see Figure 2-9 [34]).

This structure arises from a Simple Cubic (SC) lattice, which undergoes two small independent distortions of its two constituent Face Centered Cubic (FCC) sublattices in order to achieve stability: a relative displacement of the two FCC sublattices along the body diagonal, and a shear motion which decreases the rhombohedral angle α from 60°. (See Figure 2-10 for an illustration of this structure and its corresponding Brillouin zone, and Table 2.1 for values of the lattice parameters).

Their band structure is characterized by a negative indirect band gap between the conduction band (CB) minimum at the L point and the valence band (VB) maximum at the T point for Bi and at the H point for Sb[4]. Typical carrier densities for Sb are on the order of 10^{19} cm^{-3} at room temperature, and an order of magnitude lower for Bi. Figure 2-11 shows the band structure for Sb and Bi obtained via a first-principles

[4]See Figure 2-10(b) for the high symmetry points in the rhombohedral Brillouin zone.

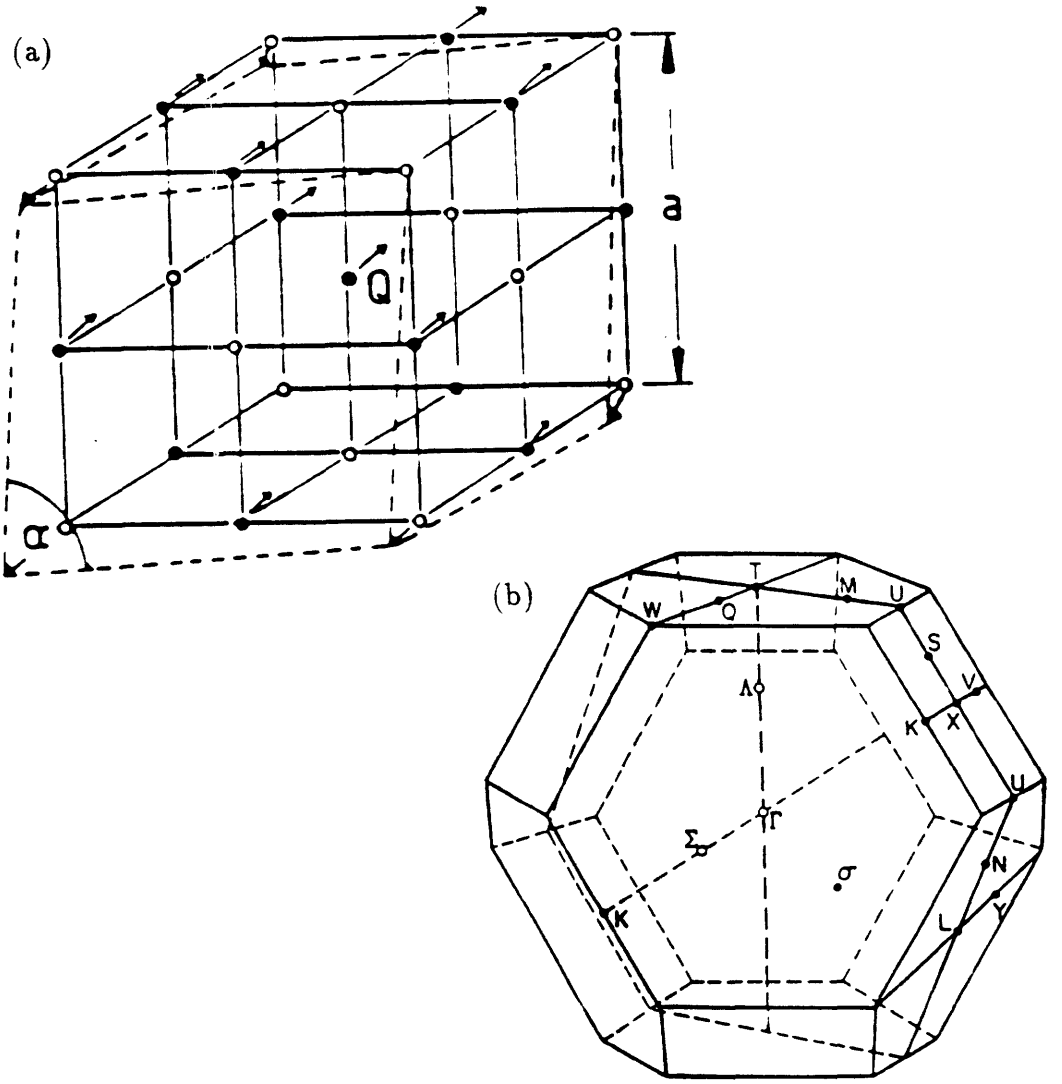

Figure 2-10: (a) Arsenic structure as a product of two distortions from the simple cubic structure, namely, a displacement between two interpenetrating FCC lattices (indicated by arrows), and a shear distortion which decreases the rhombohedral angle α from 60°. (b) Brillouin zone for the rhombohedral structure showing the standard notation for the symmetry points, lines and planes.

Table 2.1: Lattice parameters, Raman frequencies and indirect gap values for Bi and Sb.

	Sb	Bi
$a_0(\text{Å})$[a]	4.4898	4.7236
$\alpha(\text{deg})$[a]	57.233	57.35
$c_{hex}(\text{Å})$[b]	11.2	11.8
z_0[a,c]	0.46724	0.46814
$E_{gap\ ind}(meV)$[d,e]	-160	-38
$\nu_{A_{1g}(LO)}(\text{THz})$[d]	4.5	2.9
$\nu_{E_{1g}(TO)}(\text{THz})$[d]	3.5	2.2

[a] Reference [34].
[b] The hexagonal lattice parameter c_{hex} is included for convenience. It defines the length of the unit cell along the trigonal axis, and is used as a length unit.
[c] In reduced units, that is, in units of c_{hex}.
[d] Reference [28].
[e] The top of the valence band in Sb is situated at the H point, which has coordinates (0.350,0.163,0.163) in units of the rhombohedral lattice parameters [34].

pseudopotential calculation by Gonze *et al.* [34]. This calculation was performed with a matrix diagonalization technique, using a set of as many as 600 plane waves for Bi, and somewhat less for Sb.

The phonon spectra for all the semimetals are characterized by the existence of two Raman-active modes at the Γ point, with $A_{1g}(LO)$ and $E_{1g}(TO)$ symmetries, respectively.

Table 2.1 includes the material parameters of relevance for this work, namely, the lattice parameters, band overlap and frequencies of the Raman-active modes, for Sb and Bi.

The similarity of lattice parameters in Bi and Sb permits the preparation of very homogeneous $Bi_{1-x}Sb_x$ alloys, for which all the material properties vary continuously as a function of alloy composition. At $x = 0.065$, these alloys undergo a semimetal-semiconductor transition, due to a drop in the energy of the top of the valence band at the T point (T^-_{45} in Figure 2-12) with respect to the bottom of the conduction band at the L point (L_s). At $x = 0.22$, the alloy turns semimetalic again, this time

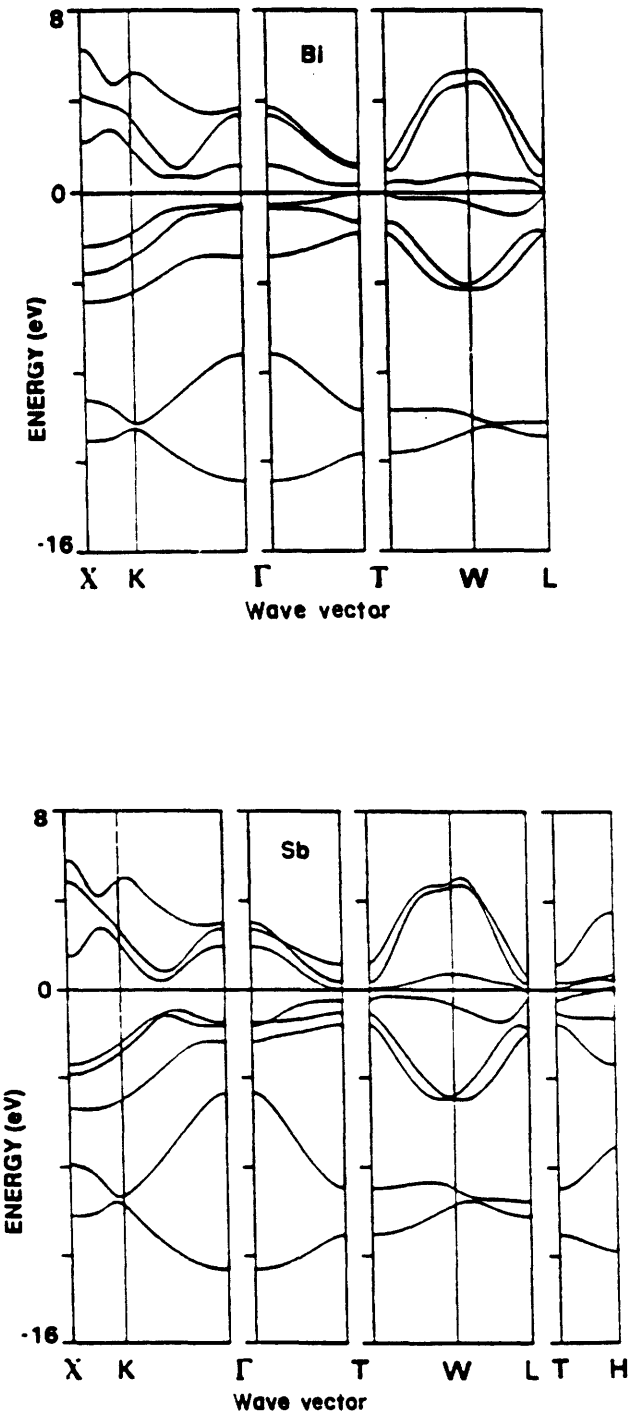

Figure 2-11: Band structure for Sb and Bi along different directions in the Brillouin zone. [34]

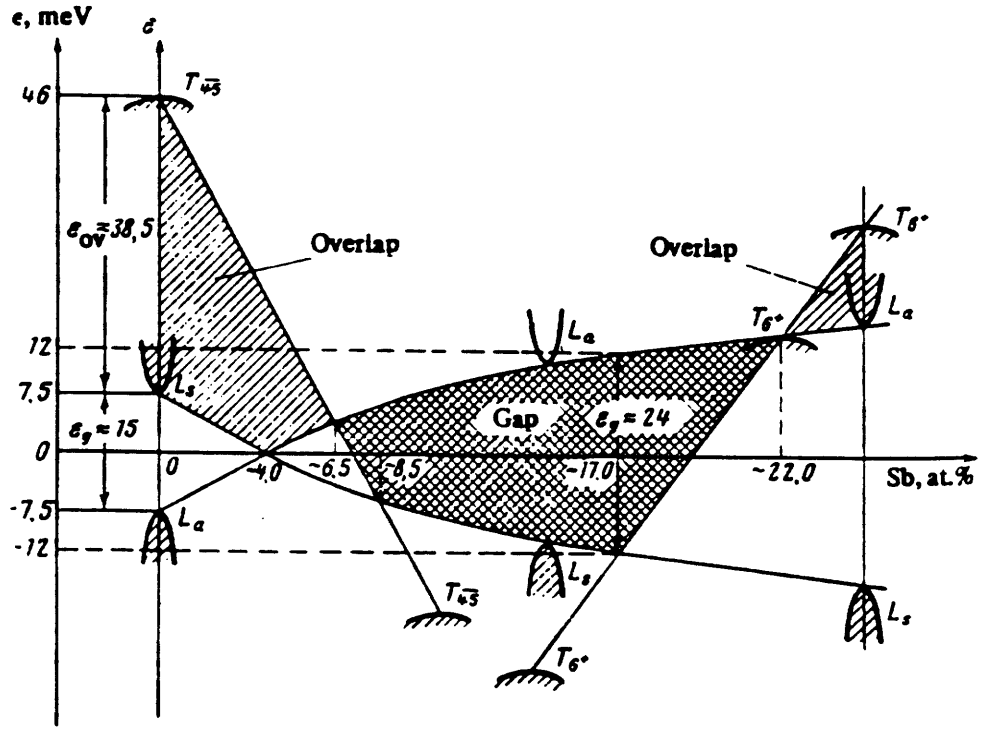

Figure 2-12: Variation of the energy bands of $Bi_{1-x}Sb_x$ alloys with increasing Sb concentration in the interval $0 \leq x \leq 0.25$. The semiconducting region is crosshatched [48].

due to the rise of the top of the valence band at H (labeled T_6^+)[5] above the bottom of the conduction band at L (L_a). In addition, the 25 meV direct band gap at the L point in Bi decreases with increasing Sb concentration, vanishes at $x = 0.05$ and increases to the final value of 100 meV for pure Sb.

These semimetal-semiconductor ($x = 6.5\%$) and semiconductor-semimetal ($x = 22\%$) transitions do not involve changes in lattice symmetry. X-ray data [47] show an anomalous increase in c_{hex}, when Sb is added in the semiconducting region, while a_{hex} steadily decreases for all composition ranges[6] (Figure 2-13).

If we conduct pump-probe experiments on $Bi_{1-x}Sb_x$ alloys in the vicinity of the semiconductor-semimetal transitions ($x = 6.5\%$ and $x = 22\%$), the coherent phonons

[5]The point is labeled with a T instead of an H because of a previous belief that the hole pocket for Sb was placed at the same k-point as for Bi.

[6]c_{hex} is the hexagonal c-axis lattice parameter, which has the length of the unit cell along the trigonal axis, and a_{hex} is the hexagonal lattice parameter in the plane perpendicular to the trigonal axis.

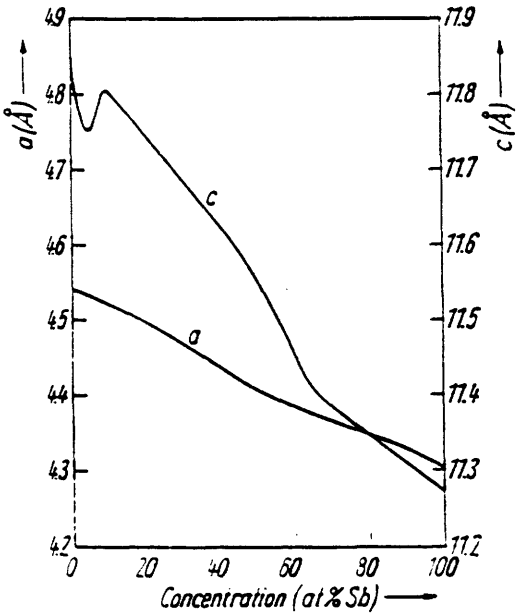

Figure 2-13: Hexagonal lattice parameters of $Bi_{1-x}Sb_x$ alloys as a function of Sb concentration. a and c are, respectively, equivalent to the a_{hex} and c_{hex} defined in the text.

may induce the indirect band gap to change sign at a THz frequency. In the following chapters, we will do a quantitative analysis of the band gap shifts induced by an A_{1g} phonon field. If the intervalley scattering time between the L and T(H) points is smaller than phonon period, the transport properties of these semimetals will be drastically modulated on a subpicosecond time scale.

For the case of Bi, an upper limit for the intervalley scattering time τ_{iv} between the L point electrons and T point holes was provided by Lopez [29]. This value was calculated via an extrapolation to room temperature of the fit to experimental data obtained by acoustomagnetoelectric (AME) effect measurements below 50 K. If the only mechanism for electron-hole recombination is a one-phonon-assisted scattering process, then $\tau_{iv}(300\ \mathrm{K})<3.8$ ps. This value is to be compared to the A_{1g} phonon period in Bi, which is 0.35 ps. It is to be expected that additional mechanisms at 300 K, such as multi-phonon-assisted scattering processes, will lower the electon-hole recombination time under the value of the A_{1g} phonon period. Nonetheless, room temperature measurements of this recombination time are required before we can

draw any conclusions.

There is a large dispersion in the empirical values of τ_{iv} provided in the literature for the $Bi_{1-x}Sb_x$ alloys with small Sb composition. For $x < 0.25$, τ_{iv} varies in the range $10^{-7} - 10^{-9}$ s, at temperatures below 4 K [30, 31]. Such dispersion does not allow to distinguish the mechanisms for intervalley scattering that are active in the semimetallic phase from those which contribute in the semiconducting phase. The larger band overlap in Sb than in Bi, with a similar distance in reciprocal space between the electron and hole pockets, will likely lead to a higher rate for intervalley scattering. This higher scattering rate may in part be offset by the fact that the effective masses of the carriers in Sb are about 3 times larger than in Bi, which would imply a smaller scattering rate. Unfortunately, no experimental data are available for the intervalley scattering time in Sb.

Experimental study

We have performed femtosecond time-resolved pump-probe studies in $Bi_{1-x}Sb_x$ alloys for x in the range $0\% - 12\%$.

Figure 2-14 shows the reflectivity data $\Delta R/R$ for two different alloy compositions near the semimetal-semiconductor transition. With regard to the oscillatory component, we can observe the appearance of a two-mode oscillation. The second mode becomes more pronounced with increasing Sb concentration. This can be seen more clearly in the Fourier transforms of the data plotted in each insert.

The frequencies found in the Fourier transforms are characteristic of two lattice modes, the dominant one being the pure Bi A_{1g} mode at $100cm^{-1}$ (3 THz), and the incipient mode at $120cm^{-1}$ (3.6 THz) is assigned to an A_{1g} mixed Bi-Sb mode [49]. No E_g modes are observed in the pump-probe data, although the Bi E_g mode at $70cm^{-1}$ (2.1 THz) produces high intensity Raman peaks, as can be seen in Figure 2-15.

The Raman data also show that the pure Sb A_{1g} mode at $150cm^{-1}$ (4.5 THz) is much weaker than the other A_{1g} modes, since very few Sb-Sb pairs are present at low Sb concentrations. This is probably the reason why this mode is not present in the pump-probe reflectivity oscillations.

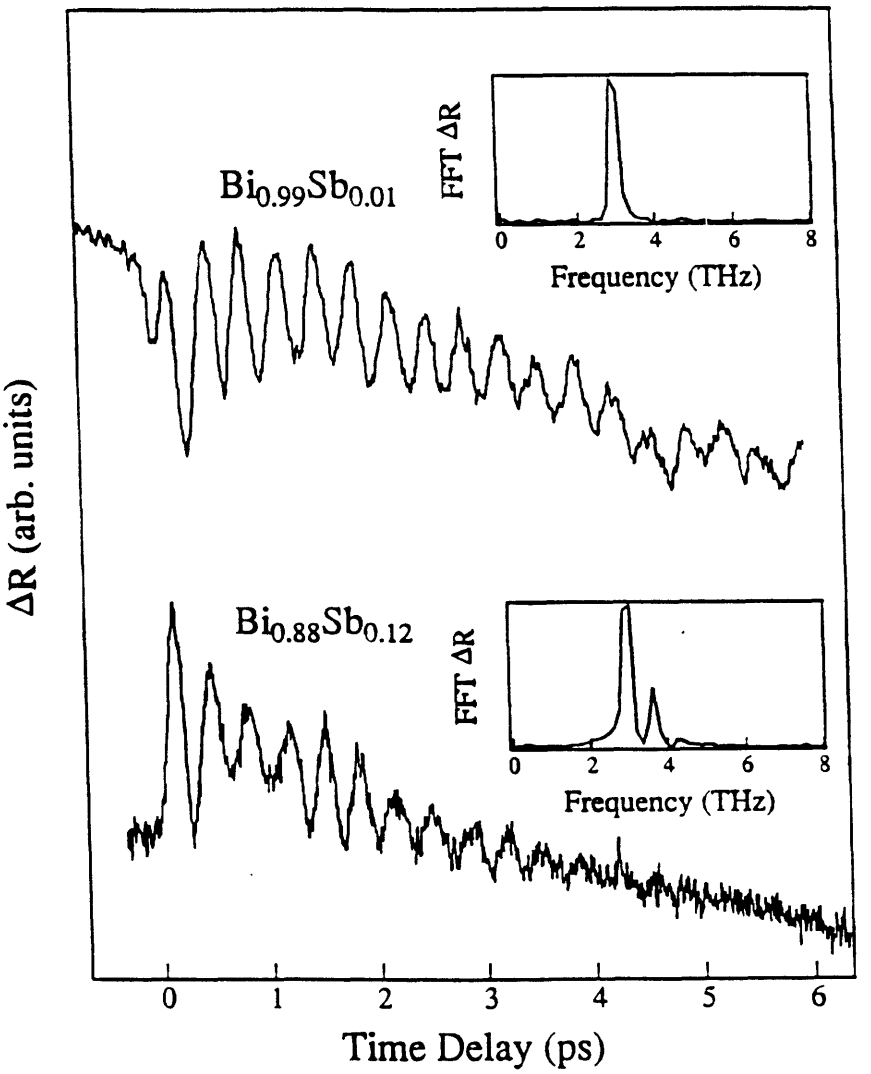

Figure 2-14: Observations of coherent generation of optical phonons in $Bi_{0.99}Sb_{0.01}$ (top) and $Bi_{0.88}Sb_{0.12}$ (bottom) alloy samples using pump-probe experiments. A Fourier transform of the pump-probe data is shown for each sample in the inset. [17]

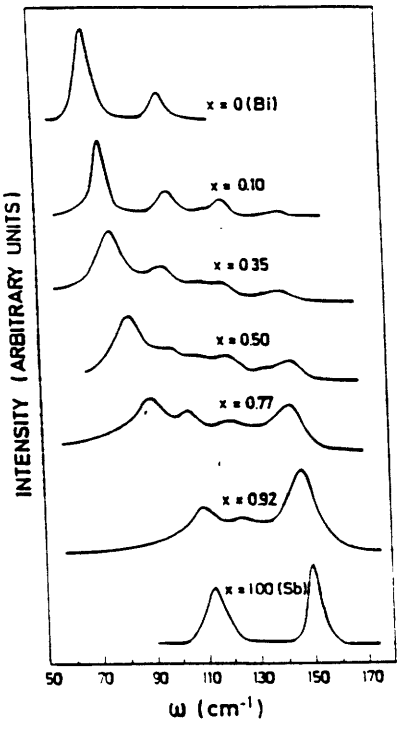

Figure 2-15: Raman spectrum of $Bi_{1-x}Sb_x$ taken with unpolarized light for various values of x [49].

2.4.2 Titanium sesquioxide

Temperature dependent transition in Ti_2O_3

Some similarities can be found between the $Bi_{1-x}Sb_x$ alloys and titanium sesquioxide, a narrow gap semiconductor with an indirect band gap of ~ 0.1 eV [52]. This semiconductor crystallizes in a hexagonal corundum structure, with two Ti_2O_3 groups per unit cell (see Figure 2-16).

If the temperature is raised from 300 to 600 K, the interatomic distances change dramatically, turning the material from a semiconductor to a semimetal [50]. As a function of increasing temperature, x-ray measurements indicate a 3% increase of the Ti(1)-Ti(2) separation across the semiconductor-semimetal transition and a slight decrease in the O(1)-O(2) distance with no change of lattice symmetry [51]. A band-crossing model has been proposed previously to explain the changes in the conductivity and in the specific heat of Ti_2O_3 at the transition [53]. In this model, the rise

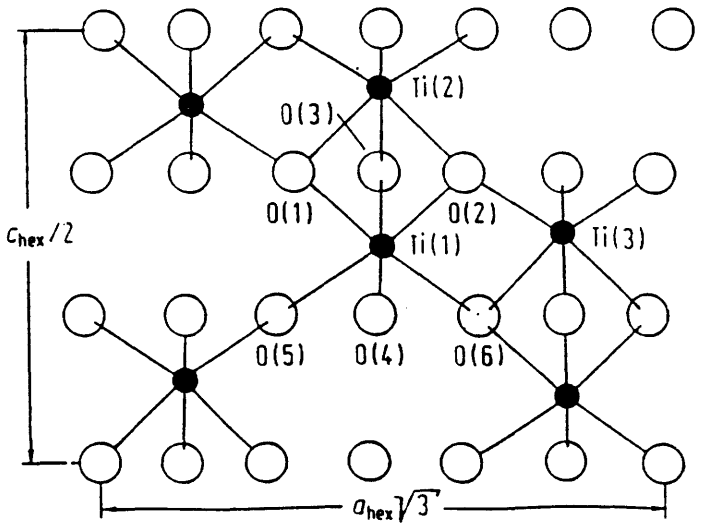

Figure 2-16: Projection of the Ti_2O_3 structure normal to the (110) direction [51].

of the top of the valence band above the bottom of the conduction band is explained in terms of those atomic displacements across the transition. It is significant that the symmetry of the lattice displacement producing the semiconductor-to-semimetal transition is the symmetry of the lowest A_{1g} optical mode in Ti_2O_3. In Figure 2-17, we present a plot of the temperature-dependent spontaneous Raman scattering data, which show a softening of the optical phonon frequencies by as much as 10% [16].

Experimental measurements

The pump-probe technique was used to investigate the temperature dependent behavior of Ti_2O_3. The data were obtained by mounting the crystal on a feedback-controlled resistive heating element. A thermocouple was used to monitor the temperature of the sample in the temperature range 300 K - 570 K with an estimated error of $\pm$30 K.

The modulated reflectivity signal, presented in Figure 2-18, shows strong oscillatory components, which are the signatures of the lower frequency Raman-active A_{1g} phonon mode.

Figure 2-19 shows the temperature-dependent behavior of the coherent phonon frequency. In the plot of the A_{1g} coherent phonon frequency, we observe the same softening and recovery previously reported by spontaneous Raman scattering data (Fig-

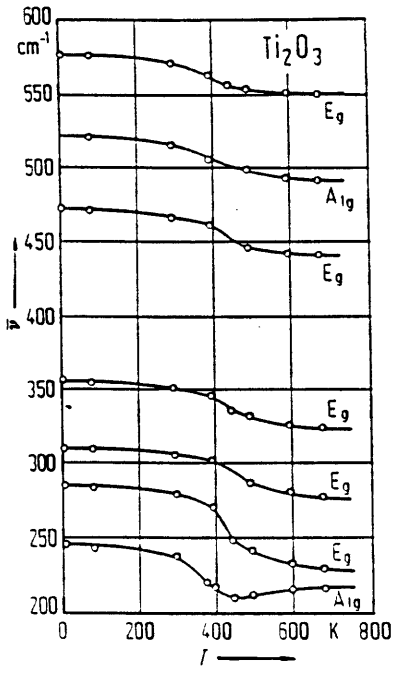

Figure 2-17: Raman-active modes in Ti_2O_3, as a function of temperature across the semiconductor-to-semimetal transition [16].

ure 2-17). The frequency of the coherent A_{1g} mode decreases with increasing temperature by ~10% through the semiconductor-semimetal transition, and at higher temperatures the A_{1g} frequency increases again.

Because the reflectivity changes are so large, we made an experimental estimation of the amplitude of the coherent phonon displacement [3]. The purpose of such an evaluation was to determine if the atomic motions during the coherent phonon oscillation could drive the material across the semiconductor-to-semimetal transition. The analysis consisted of establishing mappings between time-dependent static magnitudes of x-ray, absolute reflectivity values and spontaneous Raman scattering measurements in relation to the pump-probe transient data. A more detailed explanation of this analysis is presented in T. K. Cheng doctoral dissertation [6]. The outcome of the study was a prediction of a vibrational amplitude of 0.03Å, corresponding to a $\sim$ 1% change of the Ti(1)-Ti(2) separation. It must be noted that the accuracy of this mapping relies on the assumption that temperature-dependent changes in the refractive index arise primarily from deformations along the A_{1g} phonon coordinates.

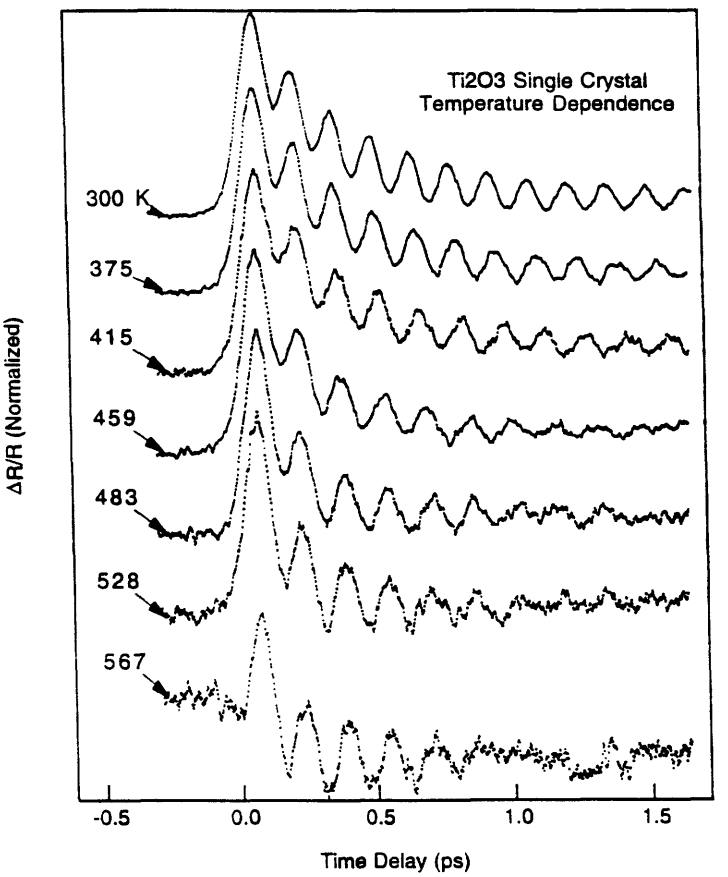

Figure 2-18: Temperature-dependent pump-probe data for Ti_2O_3. [3]

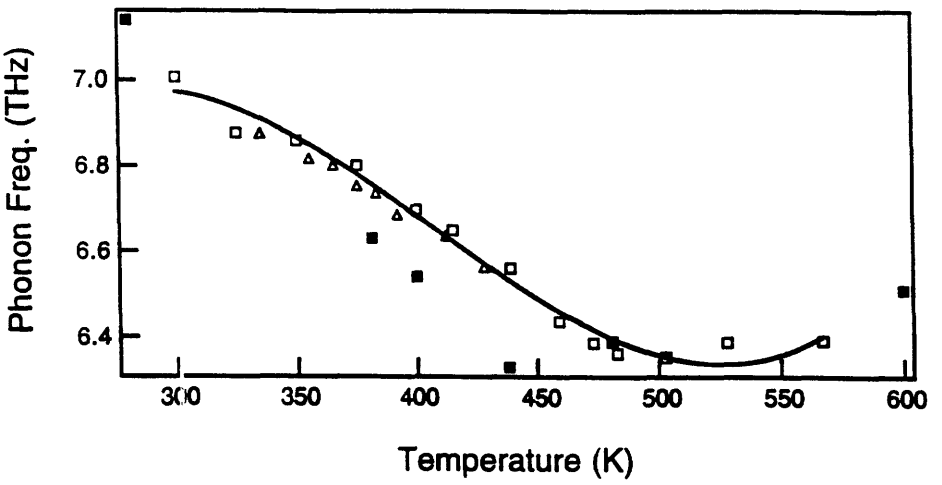

Figure 2-19: Temperature-dependence of the A_{1g} mode frequency for Ti_2O_3 across the semiconductor-semimetal transition, obtained from pump-probe experiments. [6]

2.5 Conclusions

In conclusion, we have shown that in certain coherent phonon generation experiments, it is possible to significantly modulate the properties of a solid on a subpicosecond time scale. The experiments described in this chapter extend previous coherent phonon studies because they show, for the first time, the possibility for coupling coherent phonon dynamics to electron dynamics in the limit of large vibrational amplitudes. The examples shown support the general notion that it is possible to modulate the ion coordinates in a solid so as to transform its physical characteristics at THz frequencies.

In the following chapters, we will investigate this hypothesis from a theoretical point of view, via quantitative microscopic evaluations of the coherent phonon phenomenon.

Chapter 3

Perturbative pseudopotential calculations in Bi and Sb

Although pump-probe data are available for both the Bi-Sb system and Ti_2O_3, the latter is much less understood, both theoretically and experimentally. From a theoretical standpoint, it is obvious that a hexagonal structure with two Ti_2O_3 groups per unit cell is much more difficult to tackle than the rhombohedral A7 structure, with two atoms per unit cell. In addition, Ti_2O_3 is a strongly correlated system, while bands in Bi, Sb and $Bi_{1-x}Sb_x$ alloys can be regarded as one-electron bands.

The purpose of this work is to demonstrate that the ultrafast laser-generated coherent phonons can induce a metal-insulator transition on a subpicosecond time scale. It would be desirable to develop a generic model which could account for all materials which show coherent phonon oscillations. The difficulty of such a task is compounded by the additional realization that the occurrence of a metal-insulator transition depends eventually on the value of the relative band shifts of the material in question. If the knowledge of the band structure is insufficient, as is the case for Ti_2O_3, we would fail to confirm our hypothesis.

Therefore, we will restrict our theoretical considerations to the Bi-Sb system, the ground state properties of which have been studied extensively (see Section 2.4.1 for a description of the main properties and a list of references).

3.1 Effects of the A_{1g} phonon distortion on the arsenic structure

Back in the 60's, Cohen *et al.* [25] investigated the connection between the crystal structure and the band structure of the group V semimetals and their electric behavior. For this purpose, they studied the influence on the band structure of the two distortions from the simple cubic (SC) which characterize the arsenic structure, namely the rhombohedral shear and the sublattice displacement between the two face centered cubic (FCC) lattices along one of the diagonals [1]. The band structures were obtained via first-principles pseudopotential calculations using a set of 89 plane waves.

Figures 3-1(a) through 3-1(d) show the band structures for As, presented by Cohen *et al.* [25] as a generic case for the group V elements. In Figure 3-1(a), the SC configuration leads to the band structure of a metal, with no band gaps in the vicinity of the Fermi level. Under cubic symmety, the L and T points are equivalent, but this equivalence breaks down with any of the two departures from the SC structure which characterize the group V semimetals. As shown in Figure 3-1(b), the effect of the shear distortion is to produce some band shifts, but almost all the degeneracies at the high symmetry points remain unlifted[2] . The relative displacement between the two FCC sublattices (Figure 3-1(c)) is the most sensitive distortion that leads to a breaking of the band degeneracies around the Fermi level (L and T points) and causes the opening of band gaps. Therefore, this latter departure from the SC changes the electronic properties of the material from metallic to semiconducting. Finally, the superposition of the two distortions (Figure 3-1(d)) causes the valence band at the T point to rise above the conduction band at the L point, leading to the indirect negative bandgap which characterizes these semimetals. A very interesting connection can be established between this static picture and the transient phenomena which occur in

[1] Which becomes the trigonal axis (111) in the rhombohedral structure.

[2] The T-point bands have the same degenarcies as the L-point in the SC case. The lowering of the symmetry at the rhombohedral L-point produces the splitting of a 4-fold dengenerate band into two 2-fold degenerate bands, but all of them remain below the Fermi level.

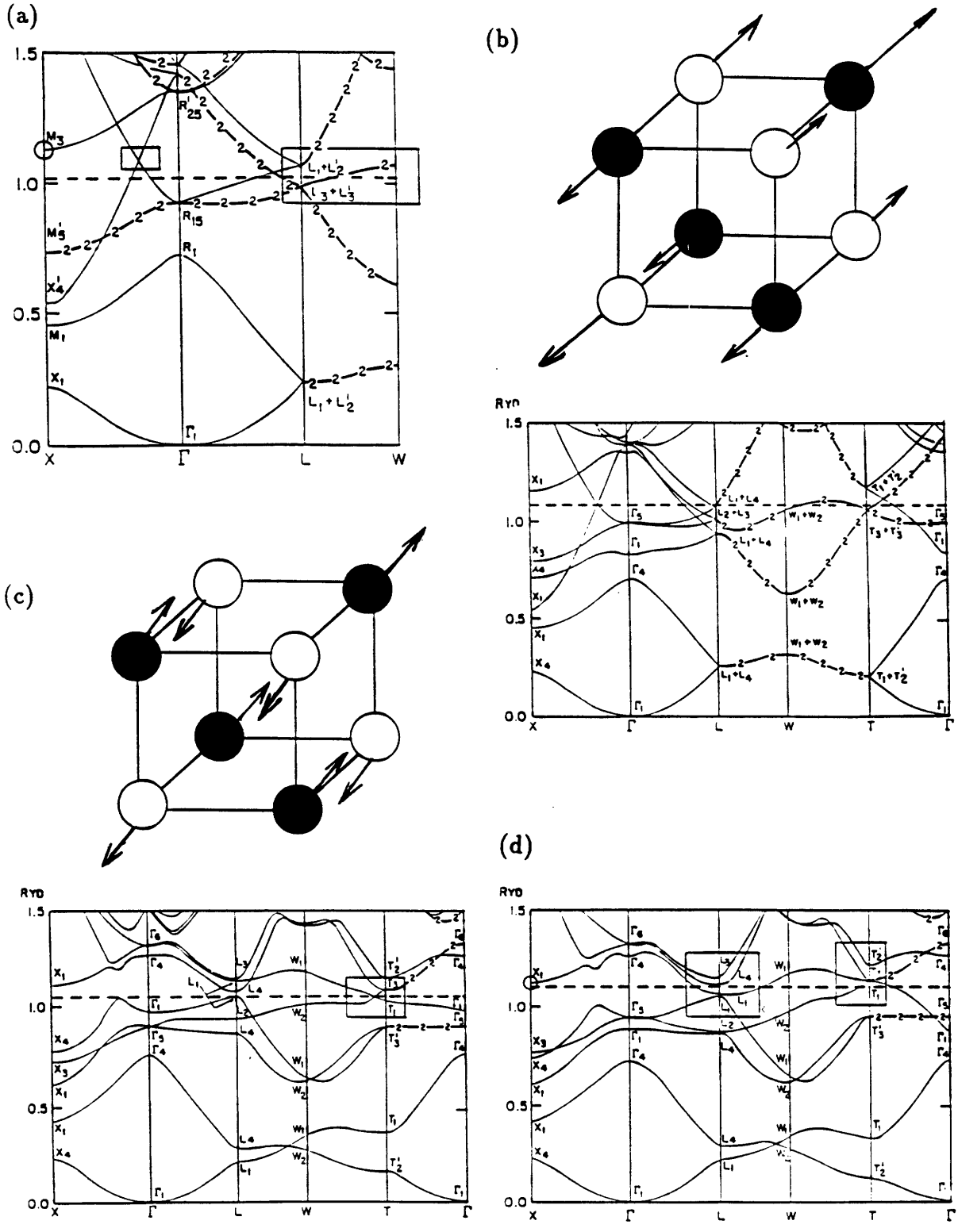

Figure 3-1: Pseudopotential band energies for the different structures obtained from distorting the simple cubic structure to obtain an arsenic structure: (a) SC, (b) Simple rhombohedral, (c) Displaced FCC , (d) Arsenic. The boxes emphasize the important features of the dispersion curves. [25]

our experiment. The association is based on the fact that the sublattice displacement (which produces the change in behavior from a metal to a semiconductor) corresponds precisely to the eigenvector of the A_{1g} phonon mode at the Γ point. This presents strong evidence for a potentially large modulation of the electronic properties of the group V semimetals when the ions are set into an A_{1g}-mode oscillation.

This qualitative description cannot bring us any further. The ultimate proof of the existence of a metal-insulator transition on a THz time scale lies in having accurate quantitative data on the magnitude of the phonon-driven band shifts and carrier scattering times.

Before attempting an exhaustive *ab initio* pseudopotential calculation on such materials, we proceeded to do a quantitative study of the bands shifts via a nearly free electron approach. The goal of this study is a better familiarization with the general band structure of the group V semimetals, and specifically with the response of the bands to atomic motions analogous to those of the A_{1g} phonon, in the vicinity of the band gap.

3.2 Nearly free electron pseudopotential calculations in Bi and Sb

3.2.1 Description

In the light of the previous discussion, we performed a pseudopotential calculation of the band shifts in a pseudo-arsenic structure[3] in Bi and Sb in the vicinity of the Fermi level. We made the further simplification that the top of the valence band in Sb is at the high symmetry T-point, instead of the lower symmetry H-point where it has actually been shown to sit. Spin-orbit effects on the bands were not considered.

The calculation proceeds as follows. Starting with a free electron band calculation, we introduce the effects of the lattice periodicity as a perturbative potential. This

[3]The pseudo-arsenic structure is obtained from the SC structure by a displacement of the two interpenetrating FCC sublattices along the (111) diagonal. Thus, we neglect the effects of the shear distortion, for the reasons stated in the previous section.

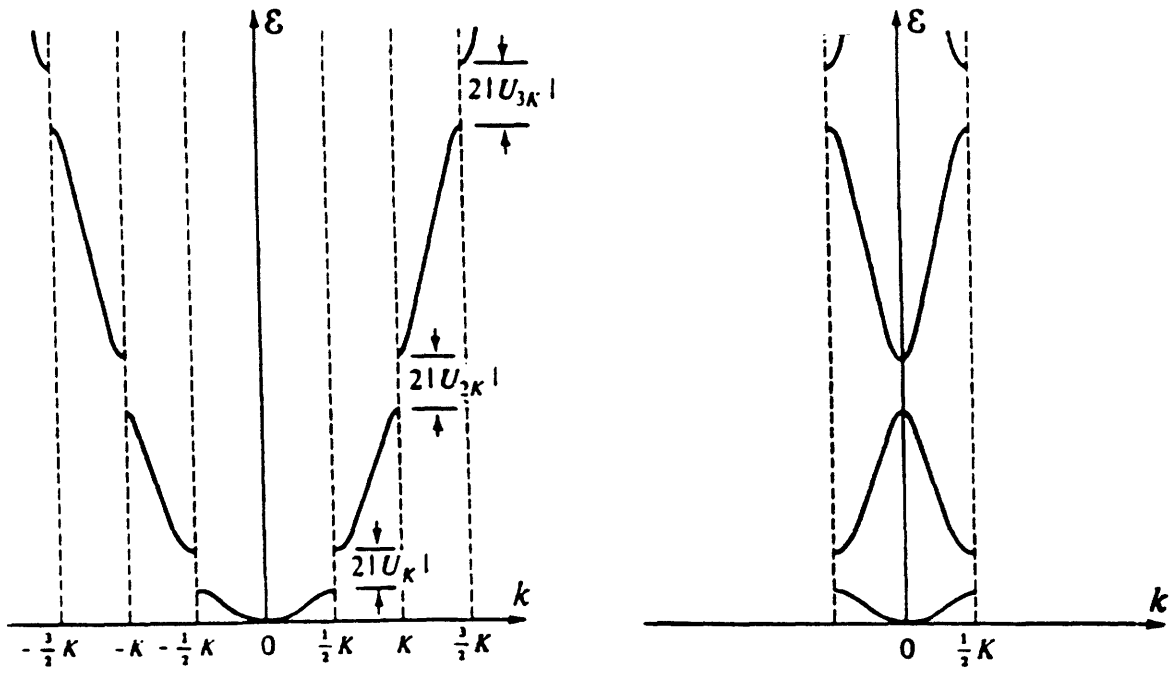

Figure 3-2: Free electron bands with a periodic perturbative potential (From [44]).

potential is evaluated by using the following semi-empirical atomic pseudopotentials, which were extracted from the literature. For antimony we consider [26]:

$$U^{\mathrm{Sb}}(K) = \frac{A_1(K^2 - A_2)}{exp(A_3(K^2 - A_4)) + 1} \tag{3.1}$$

where A_1=0.0782, A_2=2.367, A_3=3.260, and A_4=2.803 (in which K and $U^{\mathrm{Sb}}(K)$ are in atomic units) and similarly, for bismuth [27]:

$$U^{\mathrm{Bi}}(K) = \frac{3\pi Z}{Ka^3}\left[-\frac{cosKr_o}{K} + \frac{\beta sinKr_o + KcosKr_o}{\beta^2 + K^2}\right] \tag{3.2}$$

with r_o =0.474, β =3.37, and Z =3.013 (with K, a and $U^{\mathrm{Bi}}(K)$ in a.u.).

The pseudopotentials in Eqs. (3.1) and (3.2) cause a splitting of some bands, with the consequent opening of band gaps (see Figure 3-2). The 6-fold degeneracy at the L point in the SC structure is split into a 4-fold and a 2-fold degenerate level, as a result of the perturbation. These degeneracies will be totally (partially) lifted at the L (T) point, when the structure departs from the SC due to the action of the FCC sublattice displacement.

Table 3.1 shows the values of the gaps obtained in our calculations, compared to previous calculations by Falicov [26], for Sb, and Golin [27] for Bi. We also include

Table 3.1: Comparison of calculated and experimental band gap values.[a]

	Sb	Bi
$E_{gap\ dir}(L)$	286	660
(Other calculations)[b]	245	15
(Experimental value)[c]	100	15
$E_{gap\ dir}(T)$	1080	55
(Other calculations)[b]	980	505
(Experimental value)[c]	150	700
$E_{gap\ ind}$(meV)	18	347
(Other calculations)[b,d]	326	−38
(Experimental value)[c,d]	−160	−38

[a] All energies in meV.
[b] References [26, 27].
[c] Reference [28].
[d] The indirect gap for Sb is actually located between the L and H points in the Brillouin zone. This effect must be considered when comparing with the theoretical values, which are evaluated between the L and T points.

the experimental values for those gaps.

The poor agreement with experiment reflects the fact that a nearly free electron approach cannot reach the accuracy necessary to calculate the very small band gaps which characterize the semimetals. The more sophisticated first-principles calculations, which we present for comparison, show that there is some improvement in the values, but they still differ significantly from the experimental data. The extremely good agreement for the values of the gap at L and the indirect gap in Golin's calculations is merely due to the fact that these values were taken as fitting parameters to evaluate the atomic pseudopotential.

In addition, the inclusion of the spin-orbit coupling effect, which has recently been estimated to be on the order of 0.6 eV for Sb and 1.5 eV for Bi, becomes especially important and necessary when investigating the behavior of the bands in the vicinity of the Fermi level. We will again encounter at a later stage of our research the effect on the band eigenenergies of omitting the spin-orbit interaction. Nevertheless, the perturbative pseudopotential calculation under way is still a highly valuable method for estimating the size of the effect of the coherent phonon oscillation on the band

Table 3.2: Band derivatives about the band gap from perturbative pseudopotential calculations in Sb and Bi.

$dE/dz(\mathrm{eV}/\mathring{A})$	Sb	Bi
T(5)	−0.2	1.5
L(6)	−1.8	−1.8
$\mathrm{E_{gap\ ind}} = \mathrm{L(6)} - \mathrm{T(5)}$	−1.6	−3.3
$\Delta z_{\mathrm{Transition}}(\mathring{A})$[a]	−0.1	−0.01

[a] Δz indicates the change of equilibrium position needed to make the indirect band gap positive.

modulation.

3.2.2 Band gap shifts induced by the coherent phonon motion

The next step is the calculation of the band derivatives with respect to the displacement between the two FCC sublattices along the trigonal axis. Particular attention was given to the behavior of $E(\vec{k})$ at the high symmetry points T and L, where the band extrema are located.

The atomic motion affects the structure factor, which depends on the position of the atomic basis within the unit cell. We evaluated the derivatives of the bands at these points by means of a finite-difference method, that is, by calculaing band shifts, $\Delta E(\vec{k})$, for small atomic displacements, Δz, and computing the ratio $\Delta E(\vec{k})/\Delta z$.

For atomic displacements Δz as large as 1% of the trigonal axis lattice parameter c_{hex}, the band shifts at the high symmetry points T and L remained essentially linear with the A_{1g} phonon field displacements Δz. For both Sb and Bi, the band overlap increased with increasing Δz. We present in Table 3.2 the results of this quantitative analysis, which are sketched for Bi in Figure 3-3.

We have included in Table 3.2 the displacement of the equilibrium position, Δz, required to change the sign of the indirect band gap. Both in Sb and Bi this equilibrium shift is negative, which means that atom_2 would have to move towards the

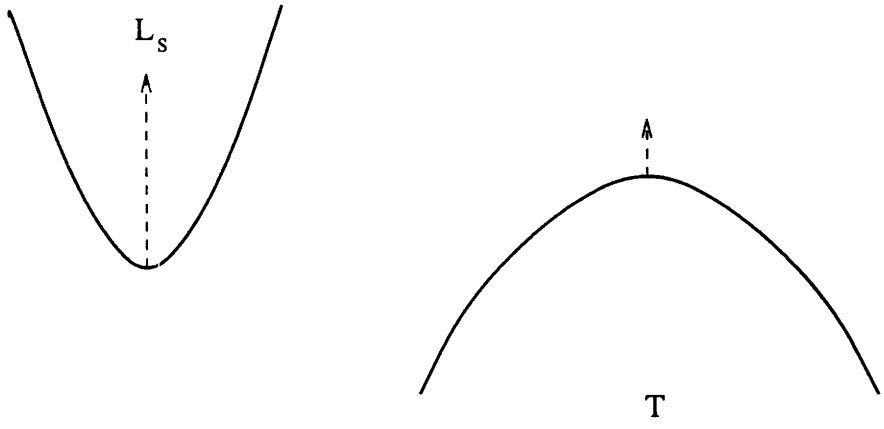

Figure 3-3: Schematic picture of the coherent phonon-induced band modulations in Bi for a phonon amplitude of $0.01\mathring{A}$, as predicted by a perturbative pseudopotential calculation.

closest $atom_1$ along the trigonal axis[4], thus increasing the distortion from the cubic structure. These calculations also indicate that the atomic shifts required to drive a metal-insulator transition in Sb are on the order of $-0.1\mathring{A}$, an order of magnitude larger than for Bi, mainly due to the fact that the band overlap in Sb at 300 K is four times bigger than in Bi.

If the amplitude of the coherent phonons were the size of the indicated displacements, $E_{gap\,ind}$ would be negative during half of the coherent A_{1g} oscillation, and it would be positive during the other half. If the characteristic time for carrier intervalley scattering across the indirect band gap were smaller than the oscillation period[5], the material would be semimetallic during the former half of the oscillation and semiconducting during the latter half.

[4]As a reminder, $atom_1$ is the atom at the origin (O), and $atom_2$ is at a distance z_0 from $atom_1$ along the trigonal axis (See Figure 2-9).

[5]See Section 2.4 for a discussion on the characteristic intervalley scattering times in Bi and Sb.

3.3 Conclusions

By means of a perturbative pseudopotential calculation for Sb and Bi, we have demonstrated that large amplitude coherent phonons can produce strong modulations of the energy bands of those materials in the vicinity of the Fermi level. Whether these modulations are sufficient or not to reverse the sign of the indirect band gap at each cycle of the oscillation depends on the amplitude Δz of the phonon.

This study does not allow us to evaluate Δz. Therefore, we cannot draw conclusions abut the feasibility of a THz metal-insulator transition in Sb and Bi. Morover, the model does not provide a means for evaluating the frequency shift, and thus compare with experimental results.

We will have to undertake a more complete theoretical study of the coherent phonon phenomenon to be able to confirm our hypothesis of a laser-excited metal-insulator transition. This study is the object of the next chapter.

Chapter 4

First-principles pseudopotential calculations for Sb

Recently, Gonze *et al.* performed an *ab initio* electron density calculation for the group V semimetals [34]. Their work showed that the spin-orbit interaction, which increases with atomic number, had an important effect on the characterization of Bi in the vicinity of the Fermi level, in agreement with prior work. The influence of spin-orbit coupling in Sb seemed to be less relevant but still important for the correct ordering, and a good description of this material around the gap could be achieved when the effect was not included.

In our description of the Bi-Sb system we displayed the band structures for Sb and Bi (Figure 2-11), as obtained by Gonze's calculations including spin-orbit coupling. These ground state calculations can be further extended to study the effect of the laser excitation on the carriers and the lattice dynamics which would follow. Such a study would provide a microscopic basis for the DECP model. A collaborative project with X. Gonze and J. C. Charlier[1] was therefore undertaken. Due to the lack of a fast code which included spin-orbit interaction, we focused our research onto the study of Sb. The goal was to extract a general picture of the mechanism for the generation of coherent phonons. This picture could then be applied to the other semimetals and

[1] Université Catholique de Louvain, Belgium.

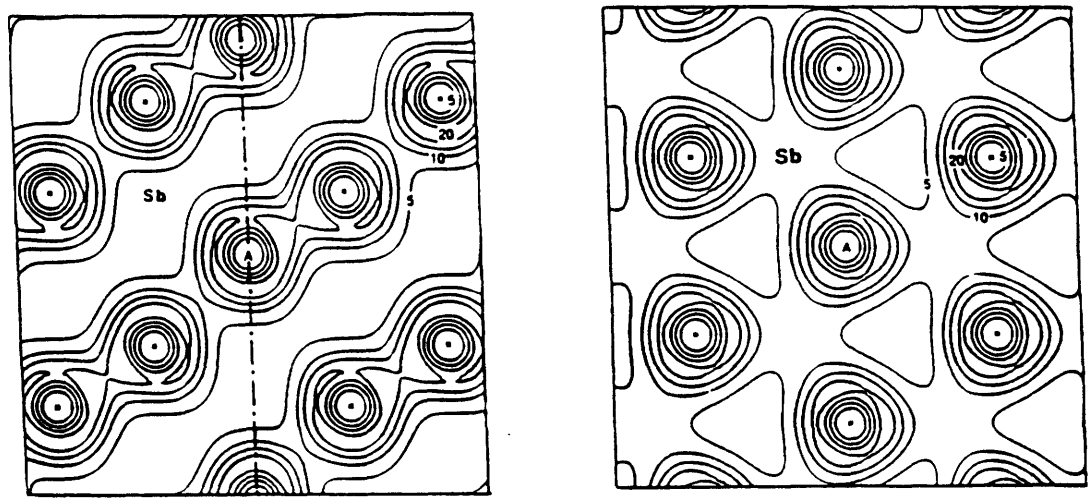

Figure 4-1: Valence electron pseudocharge densities for Sb in the planes: (a)$(1\bar{1}0)$ and (b)(111). The contour interval is in units of 5.0 electrons per primitive cell. The dashed line represents the trigonal axis. Dots indicate atoms. [34]

narrow-gap semiconductors as well.

When a laser interacts with the sample, it produces optical transitions from occupied to unoccupied states, with special spectral features observed at certain points of the Brillouin Zone. The density of electrons excited at each region in k-space depends on the square of the matrix element for optical transitions which couple initial and final states separated by an energy equal to that of the laser. Correspondingly, changes in the real space electronic distribution will occur (see Figure 4-1).

These changes in charge density generate a local potential, which produces a force on the ions and set them into coherent motion. The minimum of the total potential now acting on the ions becomes the new equilibrium around which the atoms oscillate. The difference between equilibria before and after the pump excitation determines the symmetry of the motion, and also the maximum amplitude of the coherent phonon. The second derivative of the potential with respect to the phonon eigenvector provides the new frequency of oscillation. *Ab initio* calculations can supplement our qualitative picture of the generation of coherent phonons with a complete quantitative analysis. At the time the project was undertaken, we did not have a code which could calculate the matrix elements for transitions between bands of Sb. Thus, we had to restrict the

investigation to studying the effects of the laser excitation on an A_{1g} fully symmetric phonon, an assumption based on the empirical knowledge that this is indeed the atomic displacement produced by the laser-induced change of electronic distribution. As explained before, the eigenvector of the A_{1g} phonon mode corresponds to having one of the two atoms in the unit cell displaced along the trigonal axis with respect to the other atom.

A second goal was to investigate the effects on the carriers of having the atoms set into an A_{1g}-mode coherent oscillation. These effects can be evaluated by calculating the band shifts as a consequence of the lattice motion.

In summary, we present in this chapter the *ab initio* study of the following effects on antimony:

1. The displacement of the equilibrium position and the changes in the A_{1g} phonon frequency caused by the laser-induced electronic excitation.

2. The modulation of the bands, especially in the regions around the band gap, caused by the coherent phonon oscillation.

4.1 *Ab initio* pseudopotential calculations in the framework of density functional theory

The rapid development of computers, and especially the incredible increase of computational power and speed, has permitted a parallel growth of a recent field in physics: that of first-principles techniques (also known under the latin denomination, *ab initio*). In these methods, the only input parameters are the atomic numbers of the species which constitute the system.

Even a brief overview of this vast subject would go beyond the scope of this thesis. We will summarize the main features of such calculations, so that the reader can follow our *ab initio* investigation of the coherent phonon phenomenon. Among the almost unlimited amount of literature available about the topic, I suggest an excellent review paper by Payne *et al.* [37] and references therein.

4.1.1 First-principles calculations and their approximations

The first-principles calculations can predict the electronic and geometric structure of a solid by evaluating the quantum mechanical total energy of the system and minimizing it with respect to the electronic and nuclear coordinates. Such calculations are performed with the help of advanced computational techniques, provided that some approximations are made. The main hypotheses adopted are:

- Adiabatic approximation: The large difference of mass between electrons and ions causes them to react to external fields on very different time scales. In this spirit, we can decouple the electronic and ionic dynamics, and consider the electrons moving in the static field of the frozen ions.

- Density-Functional Theory: Hohenberg and Kohn [38] proved that the total energy of an inhomogeneous gas, including exchange and correlation, is a unique functional of the electron density. The minimum value of the total-energy functional is the ground-state energy of the system, and the density that yields this minimum value is the exact single-particle ground-state density. Kohn and Sham [39] proposed then the replacement of the many-electron problem by an exactly equivalent set of self-consistent one-electron equations.

- Pseudopotential Theory: We can replace the strong ionic-core potential by an accurate *ab initio* pseudopotential that describes the salient features of the valence electron moving through the solid. (See Figure 4-2).

4.1.2 Matrix diagonalization techniques

Traditionally, the solutions of the Schrödinger equation for a physical system are achieved via the diagonalization of its Hamiltonian. This was the initial approach adopted in the first-principles calculations, but was later on replaced with other techniques better tailored to the computational nature of such calculations.

The first step towards the reduction of computational time was achieved in the spirit of the molecular dynamics method. In short, it consists of considering the

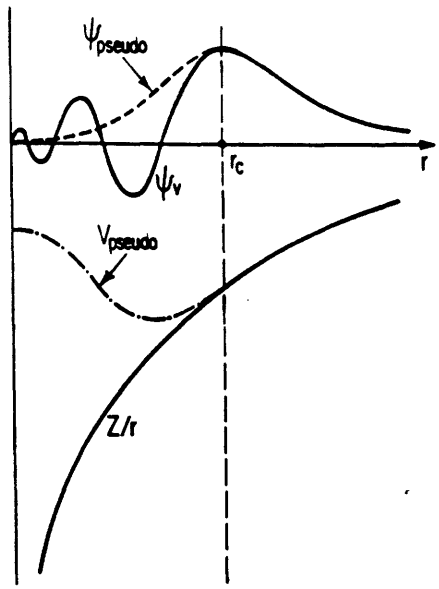

Figure 4-2: Schematic picture of all-electron (solid lines) and pseudoelectron (dashed lines) potential and their wave functions (From [37]).

coefficients of the expansion in plane waves used to generate the electronic wave function as "classical variables". The problem is then solved by a procedure analogous to that of annealing: the "particles" are given an initial kinetic energy and gradually cooled until they reach their ground state. The calculations became even faster by replacing the traditional methods of minimizing the energy functional with the method of conjugate gradients. The idea behind the conjugate gradients is that the shortest path to reach a minimum is not by going in the direction of maximum negative slope at each point of the iteration, as it woud seem at first sight, but by moving towards a direction defined from the information on all the previous iteration steps.

Again, I refer here to the paper by Payne *et al.* [37] for a more extensive description of these techniques.

4.2 *Ab initio* study of coherent phonons in Sb

In our study we used a code written by D.C. Allan, of Corning Glass [33]. This very efficient code uses separable pseudopotentials, Fast Fourier Transforms and preconditioned conjugate-gradients methods. Unfortunately, spin-orbit coupling is not included. The phonon frequencies, associated with second derivatives of the total energy, are obtained by means of a finite-difference (or frozen-phonon) technique. This consists of producing small changes in the atomic coordinates and self-consistently calculating the new total energy via the conventional matrix diagonalization procedure.

The pseudopotential for antimony was generated from the Bachelet, Hamann and Schlüter table, as explained in [35].

The first part of our dynamical simulations consists of a self-consistent calculation of the total energy, E_{tot}, for various displacements Δz for atom_2 in the unit cell away from its equilibrium position along the trigonal axis, while atom_1 remained fixed at the origin. (See illustration of the rhombohedral unit cell, in Figure 2-9). The minimum of $E_{tot}(z)$ and the second derivative at the minimum provide the ground state equilibrium position and frequency of the A_{1g} optical mode, respectively. These parameters could also be obtained from the zero-value and the first derivative of the restoring force on the displaced atom, and this force is also evaluated in the self-consistent calculation.

In order to determine the accuracy for the calculation of the equilibrium position and frequency, we studied their dependence on:

- The density of the grid in k-space, given by the number of special points, N_{SP}, in the irreducible Brillouin Zone that generate the grid. These special points are generated by applying the symmetry operations of the crystal to a set of equidistant points.

- The size of the basis set of plane waves used to expand the electronic eigenfunctions. This is determined by the cutoff kinetic energy, E_{cut}, of the expansion.

The convergence study consisted of calculating the total energy and the force on the

displaced atom for various atomic displacements along the (111) direction, at different sets (N_{SP},E_{cut}). For each set, we evaluated the minimum and second derivative of the total energy. We first fixed the number of special points at $N_{SP} = 13$, and allowed the cutoff to take different values $E_{cut} = 6.5$, 8, 9.5, 13, 15, and 22 Ha. Then, E_{cut} was fixed at 9.5 Ha, and we varied the density of the grid in k-space, with $N_{SP} = 13$, 32, 67 and 115.

Figures 4-3 and 4-4 show the results of this convergence study for both the equilibrium position z_0 and the frequency of the A_{1g} mode. We observe in those figures a much faster convergence with E_{cut} than with N_{SP}. The reason for the different rates of convergence is that Sb is a narrow gap material, and the variations of the this gap throughout the Brillouin zone can be very large. As a result, there is a different mixing of the conduction and valence bands at each point in the Brillouin zone, and the total energy of the system varies accordingly, when a new set of special points is taken. The final calculations of the electronic density were done with $N_{SP} = 67$ and $E_{cut} = 9.5$ Ha, and this cutoff energy corresponds to including a set of 580 plane waves in the expansion of the electronic wavefunction at each special point. We can evaluate from Figure 4-4 the errors in the calculations using $N_{SP} = 67$ and $E_{cut} = 9.5$ Ha. These are about 0.2% for the equilibrium position and 3% for the frequency.

For such parameters, the equilibrium position of the second atom in the unit cell[2] was found to be $z_0 = (0.4734 \pm 0.0008) \times c_{hex}$, and the frequency of the A_{1g} phonon, $\nu_{A_{1g}} = (4.5 \pm 0.1)$ THz. Figure 4-5 presents $E_{tot}(z)$, for small atomic displacements along the trigonal axis. The large error in the determination of $\nu_{A_{1g}}$ is associated with the fact that the valence and conduction bands of antimony will cross if the spin-orbit interaction is neglected. The calculation becomes unstable if the region of crossing is overemphasized in the Brillouin zone sampling. The second derivatives of the total energy, and thus the phonon frequencies, seem to be particularly sensitive to these instabilities.

A second step was to make a non-self-consistent calculation of the eigenvalues of

[2] c_{hex} is the lattice parameter along the trigonal axis, which is equal to 11.2Å for Sb. From this point on, positions will be expressed in reduced units, that is, in units of c_{hex}, unless specified otherwise.

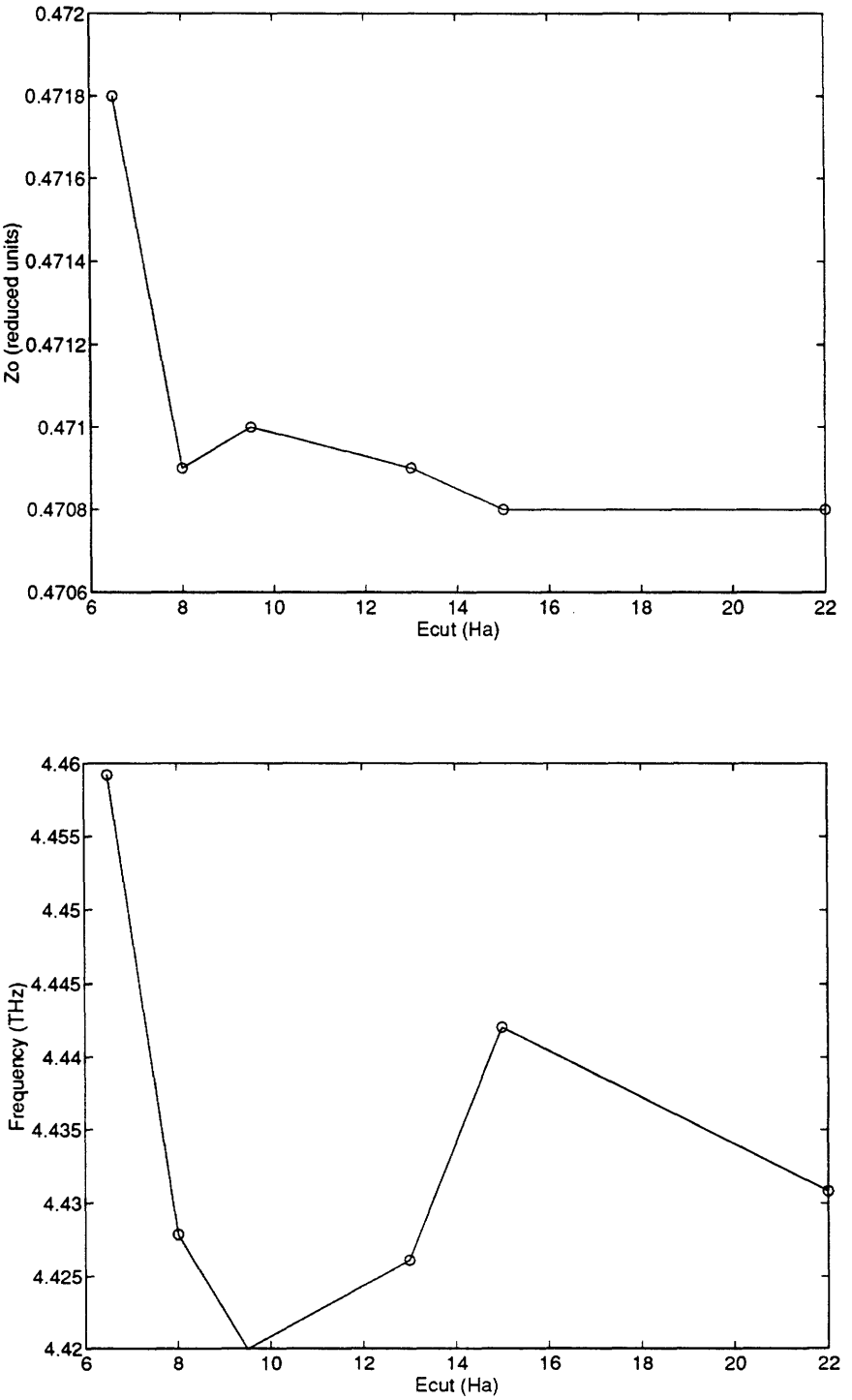

Figure 4-3: Convergence with E_{cut} of the equilibrium position and $\nu_{A_{1g}}$ for atomic displacements along the trigonal axis, using a grid in reciprocal space generated by 13 special points.

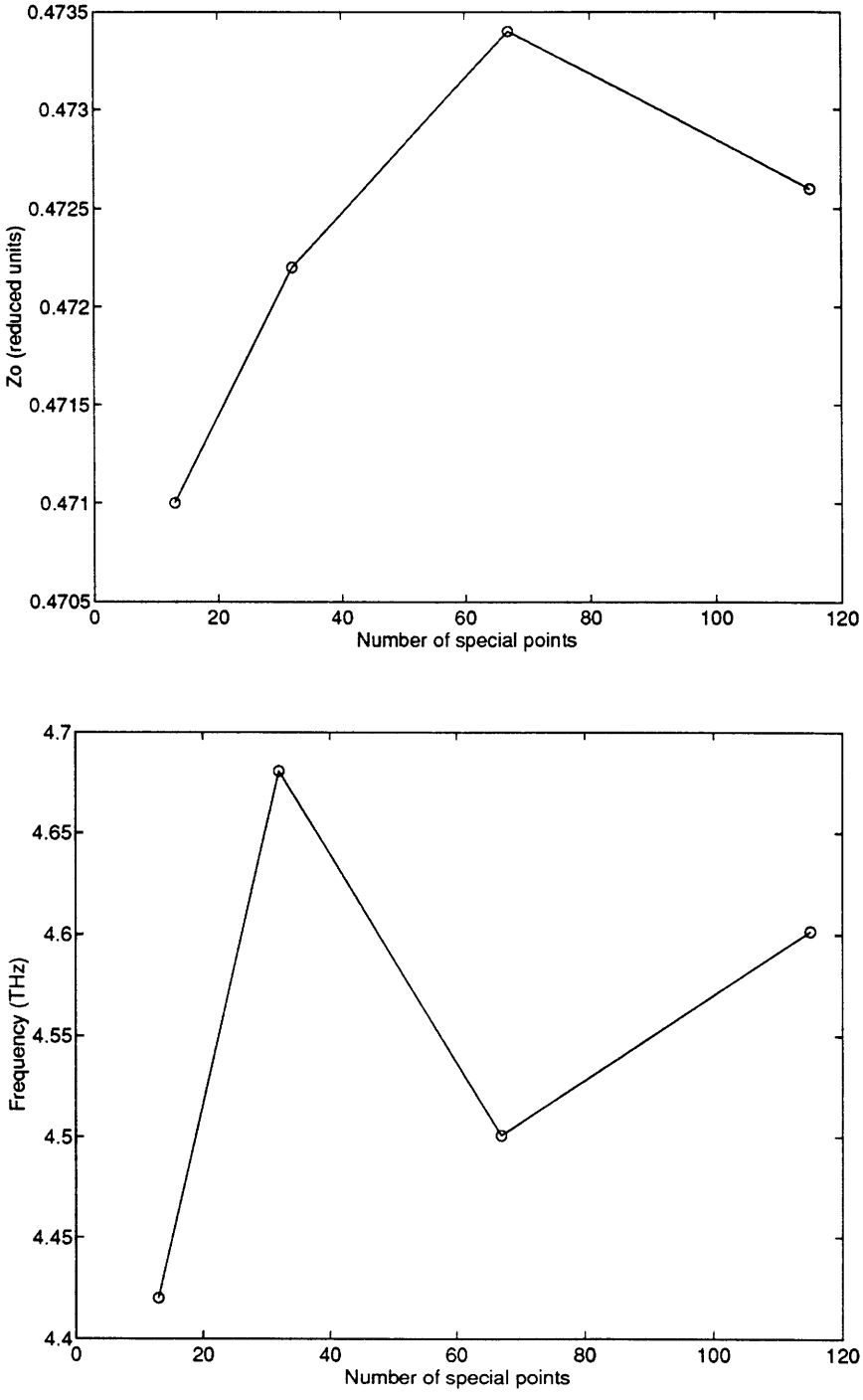

Figure 4-4: Convergence with the number of special points, N_{SP}, of the equilibrium position and $\nu_{A_{1g}}$ for atomic displacements along the trigonal axis, using an E_{cut} = 9.5 Ha.

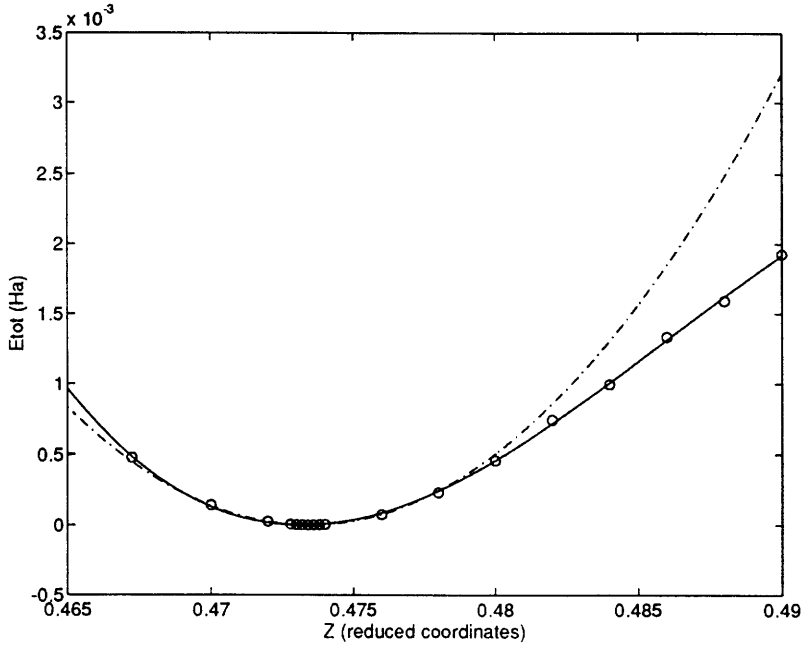

Figure 4-5: Plot of the total energy E_{tot} as a function of the displacement of atom$_2$ along the (111) axis about its equilibrium position, as obtained by a self-consistent *ab initio* calculation using an E_{cut} = 9.5 Ha and a grid in reciprocal space generated by 67 special points. The origin of energies is set at $E_{tot}(z_0)$.

Table 4.1: Eigenvalues and their first and second derivatives of the 5s (numbered 1 and 2) and the 5p bands (3 through 8) at the H and L points in the Brillouin Zone, for atom$_2$ sitting in its equilibrium position z_0.[a]

	$E(H)$	$E(L)$	$dE(H)/dz$	$dE(L)/dz$	$dE^2(H)/dz^2$	$dE^2(L)/dz^2$
1	−.423382	−.354539	.045971	.249921	−2.529652	1.970348
2	−.227334	−.339976	−.326279	−.311429	8.220348	−2.279652
3	−.141637	−.064348	.002171	.307521	−.279652	11.970348
4	−.030166	−.058221	.679771	.800121	6.470348	8.970348
5	.000000	−.032104	.000021	−.895029	.220348	5.470348
6	.012268	−.020449	−.927529	.148021	.720348	5.220348
7	.028900	−.010363	−.306529	−.305679	7.970348	−.029652
8	.105319	−.009583	.154671	−1.110929	−2.779652	.720348

[a]Energies are expressed in Hartrees and positions in reduced units, *i. e.*, in units of $c_{hex} = 11.2\mathring{A}$ for Sb.

the 5s and 5p bands at the Γ, L and H-points, using the electronic density previously calculated in a self-consistent fashion, for the various displacements of the atom from its ground state equilibrium. In addition, we obtained the first and second derivatives of these eigenvalues with respect to the atomic motion. Table 4.1 presents the results of this analysis for the gap k-points (L and H) and the atoms at the ground state equilibrium position. A first look at the results in Table 4.1 shows that the top of the valence band, H(5), lies above all the 5p bands at L. Moreover, our calculations predict a value for the indirect band gap between H(5) and L(6) of −0.020449 Ha=−555 meV, in clear contrast with the experimental value of −160 meV. This discrepancy is to be attributed to the lack of spin-orbit coupling treatment, as the above mentioned accurate calculations including spin-orbit coupling [34] are essentially in agreement with experimental data. This present calculation should nevertheless be able to obtain correct orders of magnitude for the eigenvalue derivatives with respect to atomic displacements. We also can see in the table that the derivatives of the eigenenergies with respect to z are very different from band to band. One would expect the first band to have a positive derivative (because it is a bonding state), the second to be negative (antibonding), the third, fourth, and fifth to be positive, and the upper bands to be negative, with roughly the same magnitude. Therefore, the large modulation

of the observed reflectivity is justified by the strong variation of the gradient of the eigenvalues with respect to the atomic position for bands that differ by a small energy. If this interpretation is right, a correct quantitative treatment of the states near the Fermi level, including the spin-orbit interaction, becomes extremely important.

Thus, the analysis of our data will provide at most the correct order of magnitude of the effects of the laser excitation. A more quantitative evaluation of such effects remains to be done.

4.3 Calculation of the coherent phonon amplitude and frequency shift

We develop a theory which permits us to extract from our data the changes in nuclear positions and vibrational frequencies due to electronic excitations. Let us consider three limiting cases:

1. An electron-hole pair is excited at some well-defined k-point.

2. A set of electron-hole pairs are excited, for all k-points where transitions of an energy equal to that of the laser are allowed.

3. The laser excitation is translated into a change of carrier temperature with the subsequent changes in the Fermi-Dirac distribution.

The second case is the closest to experiment, but we do not have the code to calculate the matrix elements of the transition, which are necessary to determine the number of electron-hole pairs generated at each k-point. Also the failure to obtain accurate band eigenvalues due to the omission of the spin-orbit interaction term makes this treatment difficult, because we have to borrow those values from other theoretical calculations.

If the laser excitation was followed by a carrier thermalization on a time scale smaller than the pulse width, the third case would be a good description of the process. In this situation, we would need to determine the band eigenvalues, and their first

and second derivatives for the complete set of special points used in the self-consistent calculation. Then we would calculate the variation of the band occupation numbers across the Brillouin zone caused by the carrier heating.

The inaccuracy in the determination of band eigenvalues, and thus of the Fermi level, makes any attempt of an exact treatment of Cases 1 through 3 ineffective. However, we can still give a semi-empirical description by taking from experiment the value of the energy gap and the bands between which 2 eV transitions could occur, but use the *ab initio* values for the first and second derivatives of the eigenenergies.

In the remainder of this chapter, we will develop the basic theory to make quantitative predictions of the coherent phonon phenomenon. We will then apply it to Cases 1 and 3, using the semi-empirical approach that we just described. For the carrier thermalization case, we will consider that the electrons and holes are confined to the L and H points, respectively, where the bands can be described as rigid parabolas with curvatures given by the effective masses. For small carrier temperatures, this two-band model would give a good quantitative evaluation of the effect of the carrier thermalization on the ions. In our experiment the laser may be raising the carrier temperature by a few thousand degrees, and the results of this analysis must be taken only as an estimate of the size of the effect.

4.3.1 Theory

The total energy per unit cell, when no electon-hole pairs are created, can be expanded as a Taylor series around the equilibrium position of one of the atoms:

$$E(z) = E(z_0) + \frac{\partial E}{\partial z}(z - z_0) + \frac{1}{2}\frac{\partial^2 E}{\partial z^2}(z - z_0)^2 + ... \tag{4.1}$$

At this equilibrium position z_0, the force acting on the atom vanishes:

$$\left.\frac{\partial E}{\partial z}\right|_{z=z_0} = 0 \tag{4.2}$$

and the second derivative is connected to the phonon frequency.

A fundamental theorem in density functional theory [42] relates the derivative of the energy with respect to the occupation of a level i, f_i, with its eigenvalue, ϵ_i:

$$\frac{\partial E}{\partial f_i} = \epsilon_i. \tag{4.3}$$

We consider now the total energy as a function of the parameters z and Δf_i, where Δf_i is the change in occupation number associated with the electronic excitation. Because the changes in occupation numbers are small, as well as those of the ion position with respect to its equilibrium, we use

$$E(z;\Delta f_i) = E(z_0;\Delta f_i) + \left.\frac{\partial E}{\partial z}\right|_{(z_0;\Delta f_i)}(z-z_0) + \frac{1}{2}\left.\frac{\partial^2 E}{\partial z^2}\right|_{(z_0;\Delta f_i)}(z-z_0)^2 + \ldots \tag{4.4}$$

or also

$$\begin{aligned} E(z;\Delta f_i) = \; & E(z_0;\Delta f_i=0) + \Sigma_i \epsilon_i(z_0)\Delta f_i + \left(\left.\tfrac{\partial E}{\partial z}\right|_{(z_0;\Delta f_i=0)} + \Sigma_i \left.\tfrac{\partial \epsilon_i}{\partial z}\right|_{z_0}\Delta f_i\right)(z-z_0) \\ & + \tfrac{1}{2}\left(\left.\tfrac{\partial^2 E}{\partial z^2}\right|_{(z_0;\Delta f_i=0)} + \Sigma_i \left.\tfrac{\partial^2 \epsilon_i}{\partial z^2}\right|_{z_0}\Delta f_i\right)(z-z_0)^2 + \ldots \end{aligned} \tag{4.5}$$

Figure 4-6 illustrates the dependence of $E_{tot}(z)$ on atomic displacement, both before and after the pair excitation.

Because the number of electrons remains unchanged, we have $\Sigma_i \Delta f_i = 0$. In other words, the excitation of an electron into an unoccupied band causes the creation of a hole (or absence of an electron) in the occupied band where the transition originated. In addition, in this excited-state equilibrium, the change in z due to the electronic excitation is such that the first derivative of the energy should vanish for any Δf_i:

$$\left.\frac{\partial E}{\partial z}\right|_{(z;\Delta f_i)} = 0. \tag{4.6}$$

This condition implies that

$$\left.\frac{\partial E}{\partial z}\right|_{(z_0;\Delta f_i=0)} + \Sigma_i \left.\frac{\partial \epsilon_i}{\partial z}\right|_{z_0}\Delta f_i + \left(\left.\frac{\partial^2 E}{\partial z^2}\right|_{(z_0;\Delta f_i=0)} + \Sigma_i \left.\frac{\partial^2 \epsilon_i}{\partial z^2}\right|_{z_0}\Delta f_i\right)(z-z_0) = 0 \tag{4.7}$$

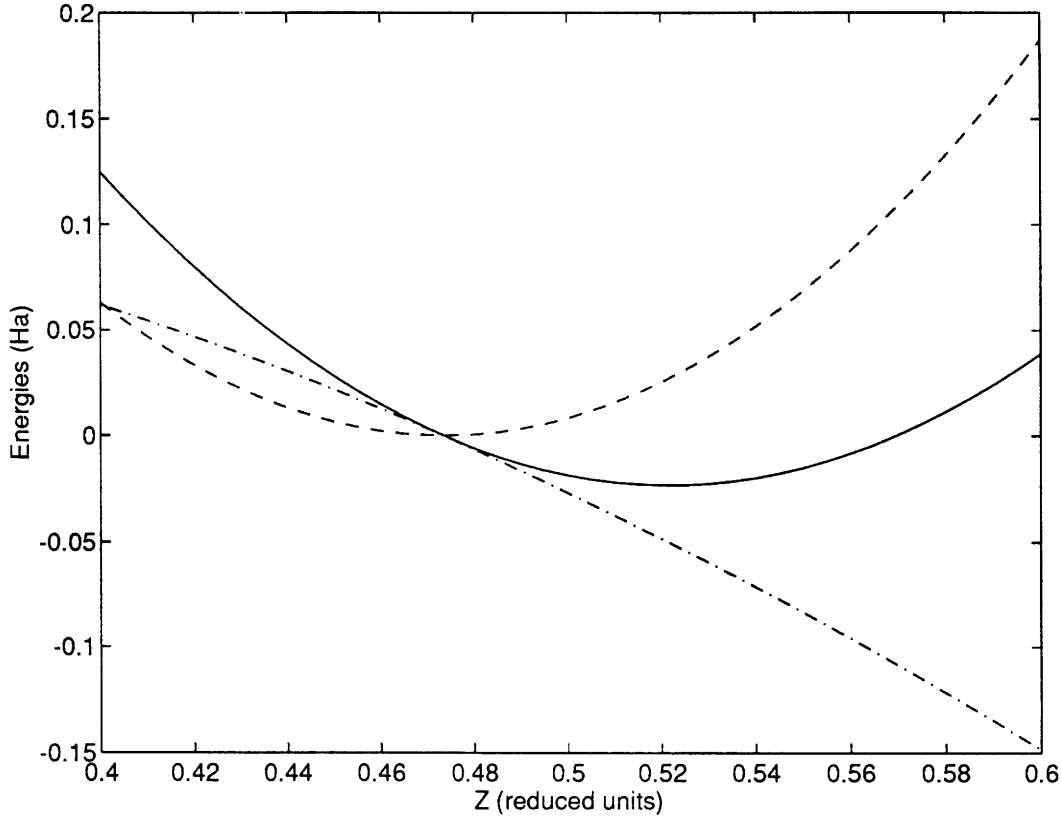

Figure 4-6: Schematic picture of the ground state energy, $E_{tot}(z; \Delta f_i = 0)$ (dashed line), change of energy due to an electronic excitation (dash-dotted line), and the resulting energy in the excited state (solid line), as a function of atomic displacement.

The first term in (4.7) vanishes due to the equilibrium condition (4.1), so we are left with

$$\Delta z = z - z_0 = -\frac{\Sigma_i \frac{\partial \epsilon_i}{\partial z}\Big|_{z_0} \Delta f_i}{\frac{\partial^2 E}{\partial z^2}\Big|_{(z_0;\Delta f_i=0)} + \Sigma_i \frac{\partial^2 \epsilon_i}{\partial z^2}\Big|_{z_0} \Delta f_i}. \tag{4.8}$$

The numerator describes the driving force, proportional to the change in occupation number, and the denominator describes the spring constant.

The phonon frequency shift relative to the spontaneous Raman value ν_R can be obtained from the latter:

$$\frac{\Delta\nu}{\nu_R} = \frac{\sqrt{\frac{\partial^2 E}{\partial z^2}\Big|_{(z_0;\Delta f_i=0)} + \Sigma_i \frac{\partial^2 \epsilon_i}{\partial z^2}\Big|_{z_0} \Delta f_i} - \sqrt{\frac{\partial^2 E}{\partial z^2}\Big|_{(z_0;\Delta f_i=0)}}}{\sqrt{\frac{\partial^2 E}{\partial z^2}\Big|_{(z_0;\Delta f_i=0)}}}. \tag{4.9}$$

In the case that the Δf_i are small, Eq. (4.8) can be simplified to:

$$\Delta z = \frac{\Sigma_i \frac{\partial \epsilon_i}{\partial z}\Big|_{z_0} \Delta f_i}{\frac{\partial^2 E}{\partial z^2}\Big|_{(z_0;\Delta f_i=0)}}, \tag{4.10}$$

and the frequency would remain essentially constant, and equal to its ground state value.

4.3.2 Direct electron-hole pair excitation

Let us consider the first case of electronic excitation, which is the generation of an electon-hole pair at a specific k-point of the Brillouin Zone. We will evaluate the equilibrium position and frequency shifts due to excitations at the H and L points, for which we have the values of the first and second derivatives of the band energies already tabulated (Table 4.1).

It is important to mention at this point that the force exerted on the atoms by a small energy or a large energy electron-hole pair can be on the same order of magnitude, because the derivative of the eigenenergy versus atomic position varies

widely from band to band. Therefore, the most important parameter is the number of such electron-hole pairs. In the experimental power-dependence study of coherent phonons (Section 2.3), we observed a linear dependence of the initial amplitude of the $\Delta R/R$ oscillations with laser power (Figure 2-4). This indicates that the number of excited particles scales linearly with the pump power, for values up to 24 mW.

The maximum number of pairs per unit cell excited by a pump pulse from a laser of energy E_{laser} and intensity P_{pump}, with a repetition rate F, focused on a spot of radius r, is given by:

$$\Delta f = \frac{P_{pulse}(1-R)}{\pi r^2 l E_{laser}} V_{uc}, \tag{4.11}$$

where $P_{pulse} = P_{pump}/F$ is the energy provided by a pulse, R is the reflectivity at the laser frequency, l the skin depth of the sample, and V_{uc} the volume of the unit cell. In our experiment, $E_{laser} = 2$ eV, P_{pump} ranges from 2 to 24 mW, $F = 80$ MHz, and $r = 1\mu$m. With regard to the parameters for Sb, $R = 0.7$ and $l = \frac{c}{2\omega Im\epsilon} \sim 100\mathring{A}$ at 2 eV [28], and $V_{uc} = 60.4\mathring{A}^{-3}$ [34]. Introducing these values in equation (4.11), we find the density of excited pairs to range from 0.05 to 0.6 per unit cell[3].

The last parameters needed to calculate Δz and $\Delta\nu/\nu_R$ are extracted from the self-consistent calculations. These are: $z_0 = 0.4734$ and $\left.\frac{\partial^2 E}{\partial z^2}\right|_{(z_0;\Delta f_i=0)} = 23.357$ Ha, which results in a frequency of 4.5 THz, in good agreement with the A_{1g}-mode spontaneous Raman value.

Let us consider first excitations at the H point in the Brillouin zone. The only transition allowed at H for the laser energy of 2 eV is between the occupied 4^{th} band and the unoccupied 6^{th} band. Using equations (4.8) and (4.9), we can calculate the coherent phonon amplitude and laser shifts as a function of the pump intensity. Figures 4-7 and 4-8 show plots of the results. We have added in Figure 4-8 the experimental data previously presented in Section 2.3.

An analogous study can be performed for excitations taking place at the L point, as a result of an optical transition between the 6^{th} partially occupied band and the

[3]This range corresponds to excited carrier densities on the order of $10^{19} - 10^{20}$ cm^{-3}.

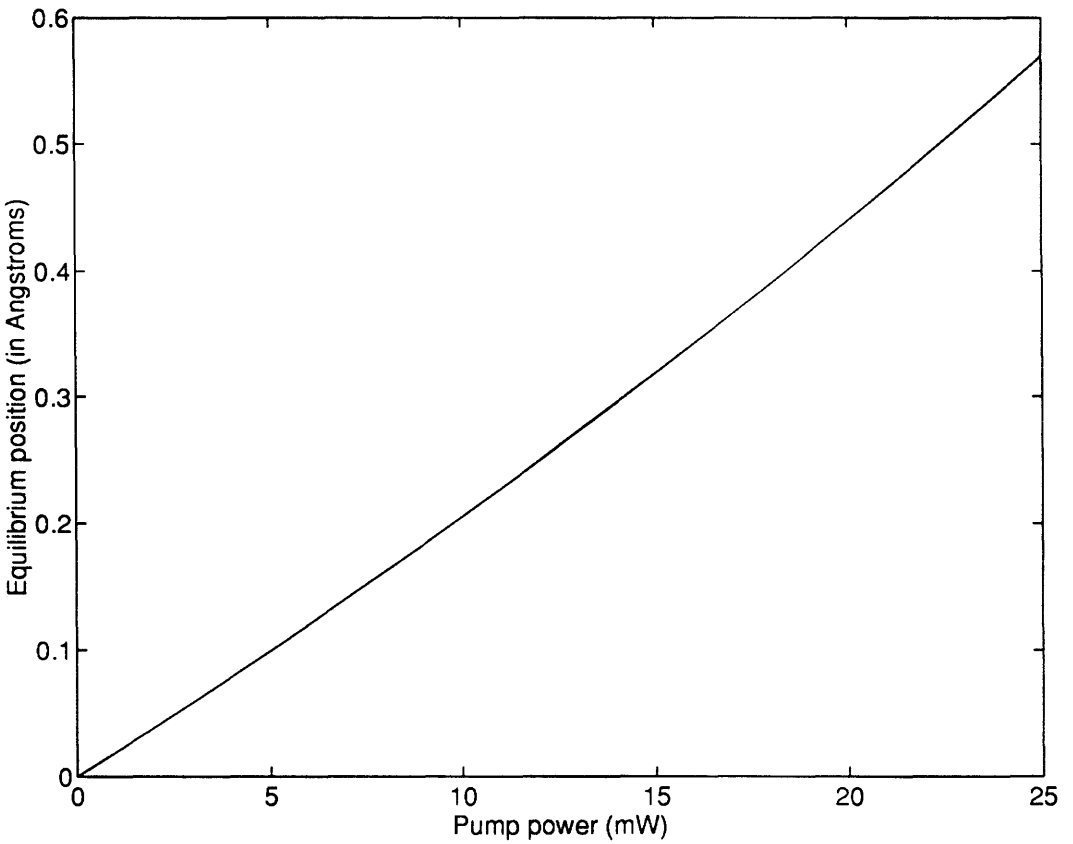

Figure 4-7: Calculated equilibrium position displacement of $atom_2$ along the trigonal axis as a function of pump power, for electron-hole pairs created via an optical transition between the 4^{th} and 6^{th} bands at the H point.

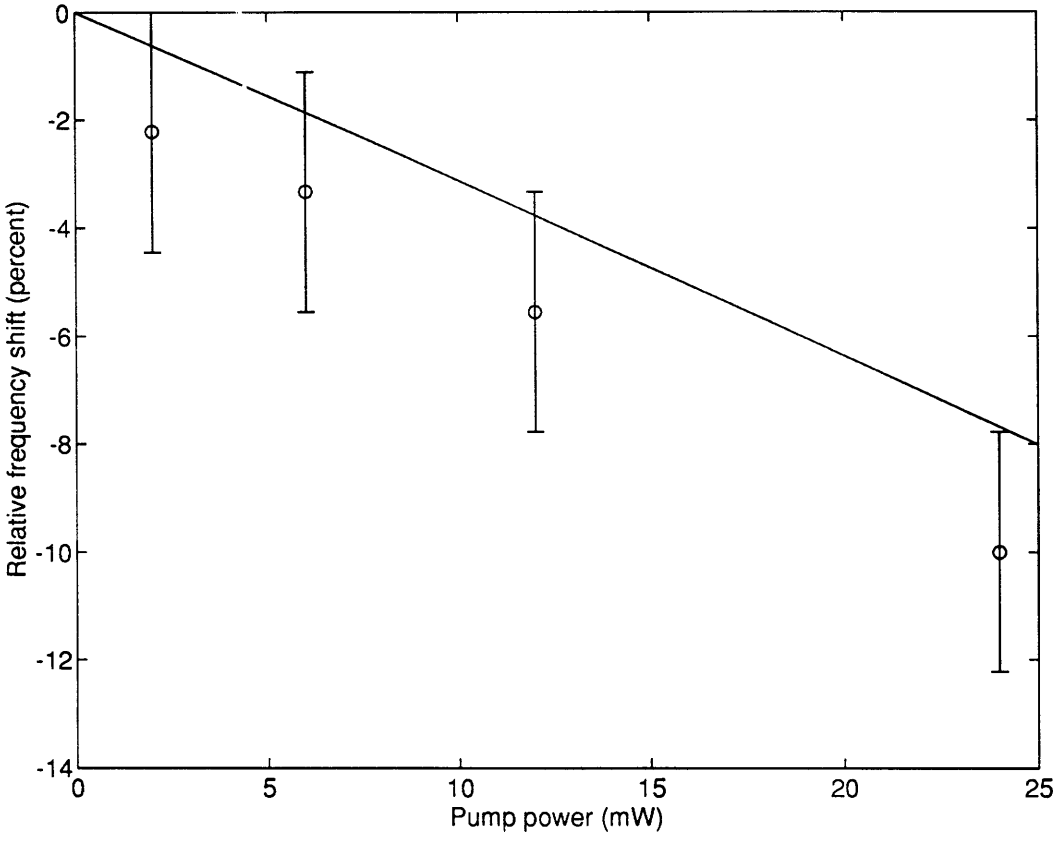

Figure 4-8: Calculated relative frequency shift of the A_{1g} vibrational mode as a function of pump power for e^--hole pairs excited between the 4^{th} and the 6^{th} bands at H (solid line). The data points correspond to the experimental fits from Figure 2-5, using as a baseline the A_{1g}-mode Raman value of 4.5 THz.

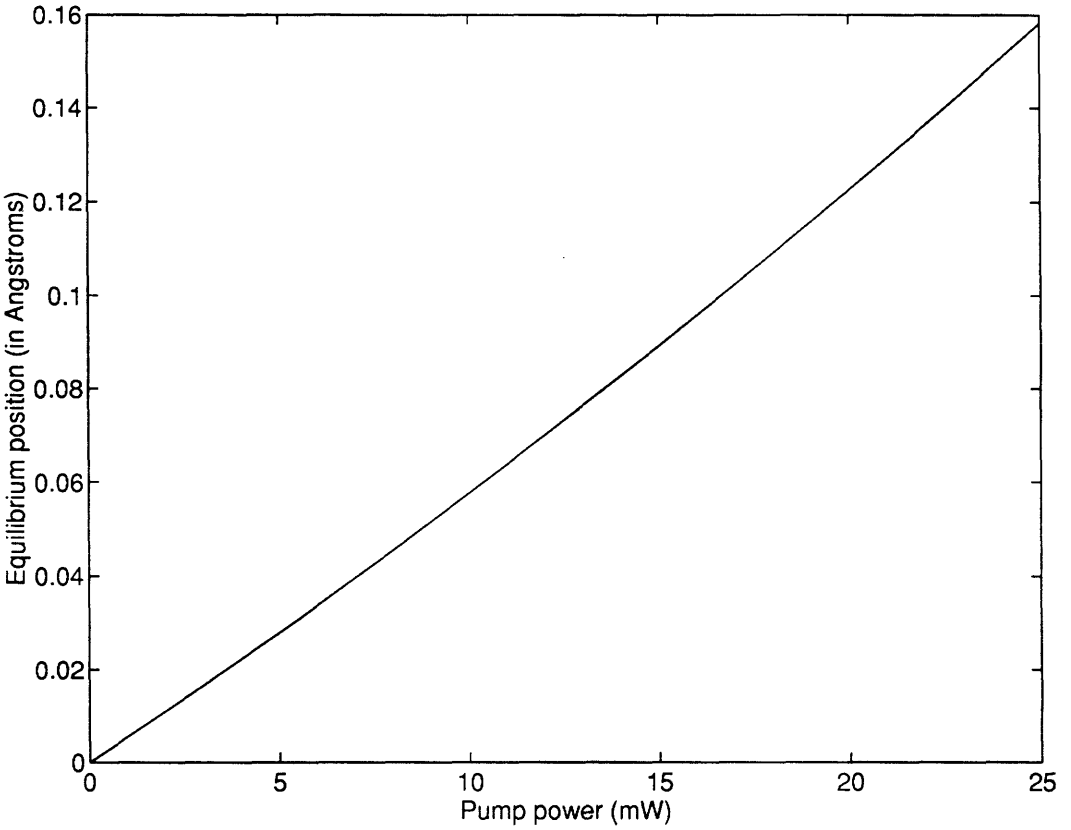

Figure 4-9: Calculated equilibrium position displacement of $atom_2$ along the trigonal axis as a function of pump power, for electron-hole pairs created via an optical transition between the 6^{th} and 7^{th} bands at the L point.

7^{th} unoccupied one. Figures 4-9 and 4-10 display those results.

From the results we can draw several conclusions:

- The shift of the equilibrium position induced when the laser creates 0.6 electrons pairs per unit cell at the H-point is of $\Delta z = 0.5\mathring{A}$. This value represents $\sim 10\%$ of the Sb-Sb minimum separation along the trigonal axis[4].

- If the laser excitation interacted only with electrons at the L point, the expected

[4]This number is to be compared with the A_{1g}-phonon thermal amplitude at $\sim$ 300 K, which is on the order of $10^{-2}\mathring{A}$. At first sight it may seem that the thermal excitation would disguise the effect of the coherent phonons in the low-power experiments. The reason for this not being the case is that the thermal oscillations are incoherent, and the average atomic displacement from equilibrium over a volume is zero at any instant. Instead, the laser-generated coherent phonons have a net displacement at all instants after the pump excitation.

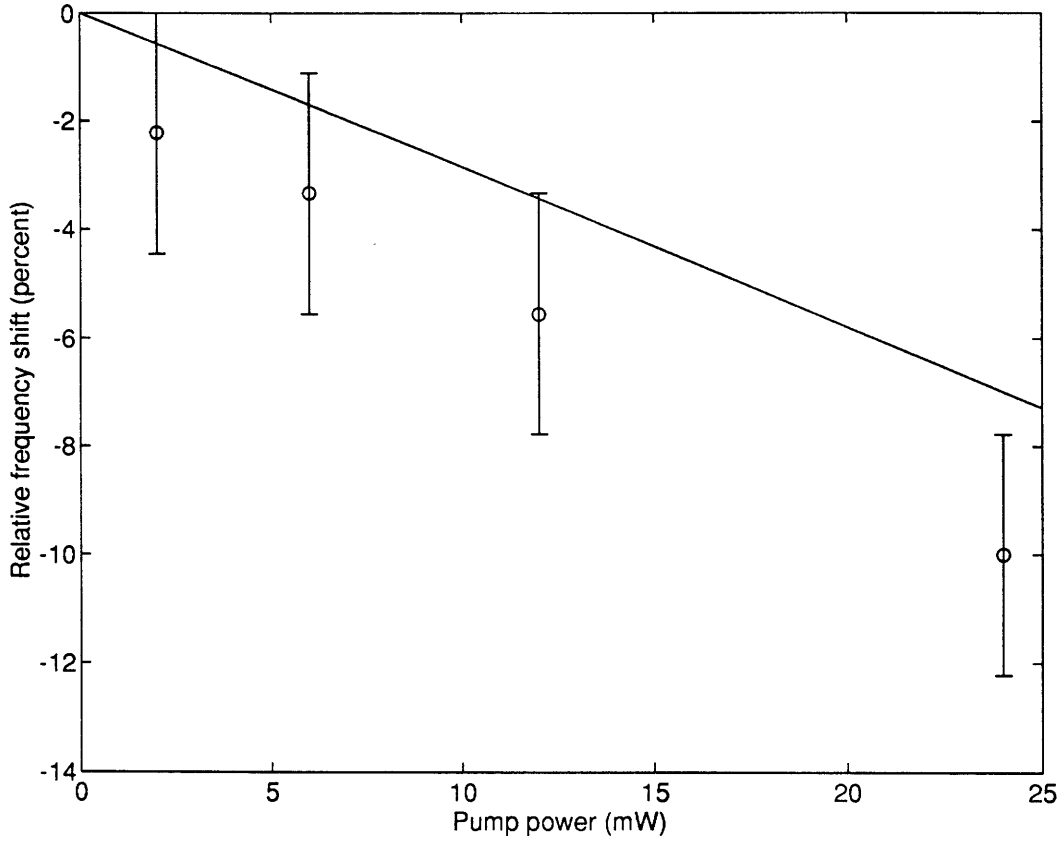

Figure 4-10: Calculated relative frequency shift of the A_{1g} vibrational mode as a function of pump power for e^--hole pairs excited between the 6^{th} and the 7^{th} bands at L (solid line). The data points correspond to the experimental fits from Figure 2-5, using as a baseline the A_{1g}-mode Raman value of 4.5 THz.

displacement of the equilibrium position would be about three times smaller.

- The sign of the shift is positive in both cases, indicating that the laser excitation moves $atom_2$ towards the center of the unit cell, thus reducing the distortion from the cubic structure that characterizes the group V semimetals. This result is intuitively correct, as an increase of the number of carriers turns the material more metallic, which is indeed the expected behavior if it crystallized in the simple cubic structure.

- It is to be expected that when we consider electron-hole excitations across the entire Brillouin Zone (Case 2) the size of the effect will not differ much from that obtained for Case 1. Nevertheless, the sign of the atomic displacement depends on the values of the first derivatives in the bands involved in the transition. Only the complete analysis in Case 2 can determine this sign with reliability.

- The agreement with experiment of the frequency shifts produced by excitations at the H and L points (Figures 4-8 and 4-10) indicate that transitions at those points have a strong influence on the A_{1g} coherent phonons. The slight divergence at high powers is due to having truncated the Taylor series of the total energy of the system with electronic excitation at second order in Δf. Therefore, the calculation becomes less accurate for $\Delta f = 0.6$.

- For high powers, the estimated frequency shift is $-7 \pm 0.2\%$[5], which is consistent with the experimental prediction of $-9 \pm 2\%$.

In summary, this calculation supports the hypothesis that the mechanism for the generation of coherent phonons is the direct laser excitation of electron-hole pairs at specific k-points in the Brillouin zone. The fact that the only Raman-active mode detected in all the materials studied is the fully symmetric A_1 mode indicates that these excitations take place simultaneously at many k-points of the Brillouin zone. The very good agreement with experiment of the evaluated frequency shifts in both

[5]Remember that the relative accuracy of our *ab initio* calculation for the frequencies is $\sim 3\%$.

examples considered provides quantitative support of our analysis. We have also estimated the coherent phonon amplitude to be on the order of a few tenths of an Angstrom, at most. The fact that the two examples give different predictions indicates that we need a full Brillouin zone study of the electron-pair excitation to determine this magnitude with more accuracy[6].

4.3.3 Carrier thermalization

We are going to study here the effects on the nuclear positions and frequencies of a rapid thermalization of the carriers after the laser excitation has occurred (Case 3). Recent studies of the carrier thermalization in Au following an ultrafast laser excitation indicate that the time needed for the carrier distribution to be described by a Fermi-Dirac function may be on the order if a picosecond [36]. Therefore, it is likely that the electronic distribution in Sb is not fully equilibrated right after the pump excitation, and that an intermediate situation between Cases 2 and 3 is occurring in the experiment. Even if the electronic distribution is not fully equilibrated, as soon as the number of secondary electron-hole pairs is sufficiently large, the force on the atoms will induce their motion. Thus, the fully equilibrated distribution will give a good measure of the maximal force, for constant energy given to the system.

This small temperature perturbative treatment is not valid for high carrier excitations. As we will see at the conclusion of our analysis, the temperatures reached by the carriers to achieve thermal equilibrium after an excitation by a low intensity pump-pulse are already quite high. Therefore, we restrict the use of this model to low pump-intensity experiments ($P_{pump} \sim 1$ mW, which corresponds to an excitation of ~ 0.02 carriers per unit cell). In this regime, we can extrapolate from Figure 4-7 in the previous section the expected atomic displacement, which is $< 5\text{m}\mathring{A}$, or about 0.1% of the Sb-Sb distance along the trigonal axis. The different nature of this new mechanism for displacive excitation of coherent phonons may invalidate estimates obtained with other mechanisms. Nevertheless, we will assume that the displacements

[6] As mentioned before, we would need a code which calculated the matrix elements for optical transitions, and also included the spin-orbit effect, to undertake such calculation.

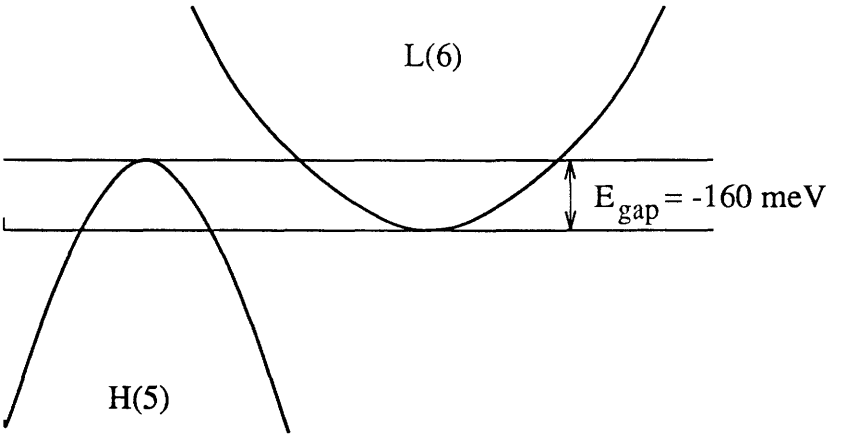

Figure 4-11: Schematic illustration of the bottom of the conduction band, L(6), and the top of the valence band, H(5), for the Sb the two-band model.

are small and verify our hypothesis *a posteriori*.

In our semi-empirical approach, we consider that the carriers are confined to two parabolic rigid bands. The curvatures of the bands are assumed to remain constant and equal to the reciprocal carrier effective masses, which we obtain from experimental data as an average of the mass tensor, $\overleftrightarrow{M}$ [28]: $m_{eff} = \sqrt[3]{det|\overleftrightarrow{M}|}$. Thus, for the electrons at the L pocket, the average effective mass is $m_L = 0.146m_0$[7], and for the holes at the H pocket, $m_H = 0.085m_0$. The experimental indirect band gap at 300 K is taken to be -160 meV. Figure 4-11 sketches the bands at 300 K.

The Fermi level for such a system is determined by charge neutrality, taking into account the multiplicity of the pockets (3 at the L point and 6 at the H point). We extract from our *ab initio* simulations the values for z_0 and $\partial^2 E/\partial z^2|_{(z_0;\Delta f_i=0)}$ given in the previous section, and also the shift of the band gap, E_{gap}, with respect to atomic displacement, which is given by the difference between the derivatives at the top of the valence band and at the bottom of the conduction band:

$$\frac{dE_{gap}}{dz} = \frac{dE(L(6))}{dz}\bigg|_{(z=z_0)} - \frac{dE(H(5))}{dz}\bigg|_{(z=z_0)}. \tag{4.12}$$

An alternative procedure to evaluate dE_{gap}/dz is to fit $\Delta E_{gap}(z)$ as a function of

[7] m_0 is the free electron mass.

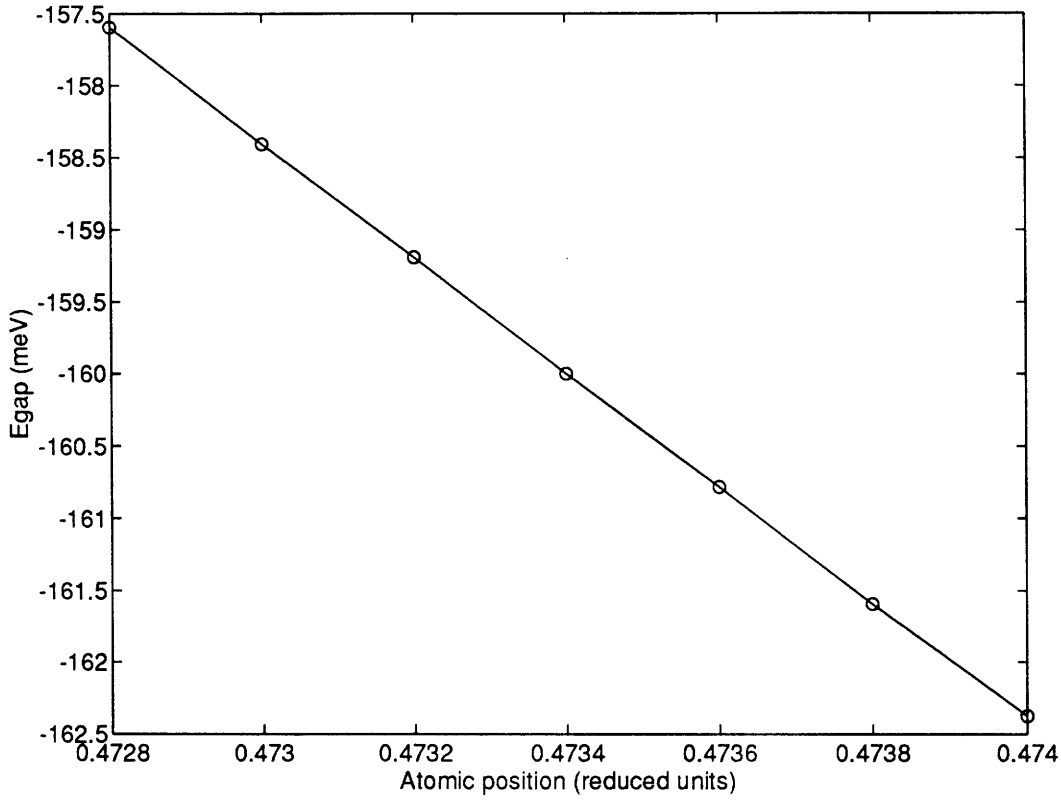

Figure 4-12: Variation of the energy gap in Sb as a function of the displacement of $atom_2$ along the trigonal axis.

Δz, where $\Delta E_{gap}(z)$ is the *ab initio*-calculated shifts of the the band gap when $atom_2$ moves along (111). Figure 4-12 shows the fit to the data.

This method provides in addition the possibility of verifying that the band gap varies linearly with atomic displacement, for small values of Δz. The slope of the straight line is $dE_{gap}/dz = -358$ meV/Å, which is consistent with the value of the first derivative of the gap, $dE_{gap}/dz = -360$ meV/Å, extracted from the data in Table 4.1.

Our goal is to find the equilibrium carrier temperature, T_{el}, and induced atomic displacement, Δz, when additional energy is given to the system by the laser. This value of Δz will be determined by minimizing the total free energy of the electrons

and ions with respect to the atomic displacement,

$$\left.\frac{\partial F(z,T_{el})}{\partial z}\right|_{(z=z_0+\Delta z;T_{el})} = 0 \tag{4.13}$$

with

$$F(z,T_{el}) = E_{el}(z,T_{el}) - T_{el} \times S_{el}(z,T_{el}) + E_{phonon}(z) \tag{4.14}$$

where $E_{el}(z,T_{el})$ and $S_{el}(z,T_{el})$ are the carrier energy and entropy, respectively, evaluated using well known expressions containing Fermi-Dirac integrals[8]. The atomic contribution, which models the changes in the atomic equilibrium position due to changes in electronic occupancy, can be written as,

$$E_{phonon}(z) = \frac{1}{2}\left.\frac{\partial^2 E_{tot}(z)}{\partial z^2}\right|_{(z_0;\Delta f_i=0)}(z-z_0)^2 \tag{4.15}$$

where the value of the second derivative of the energy was obtained by the *ab initio* calculation.

The minimization of $F(z,T_{el})$ for a set of carrier temperatures will give a functional dependence $\Delta z = f(T_{el})$. In order to determine the temperature achieved by the carriers and the associated atomic displacement we have to impose an additional constraint, namely, that the change of the total energy of the system equals the energy provided by the laser pulse. That is,

$$\Delta E(z,T_{el}) = E(z,T_{el}) - E(z_0,T) = \Delta E_{el}(z,T_{el}) + E_{phonon}(z) = E_{laser}, \tag{4.16}$$

where T is the temperature of the sample before the arrival of the pump and is equal to 300 K. The value of E_{laser} which corresponds to a 2 eV laser excitation of 0.02 electron-hole pairs per unit cell is 0.04 eV per unit cell.

Figures 4-13 and 4-14 show respectively the plots of the surfaces $F(z,T_{el})$ and $\Delta E(z,T_{el})$, for small atomic excursions and a range of carrier temperatures up to several thousand degrees. We have also included in Figure 4-14 the constant plane

[8]See Ashcroft and Mermin [44], p. 42 ff.

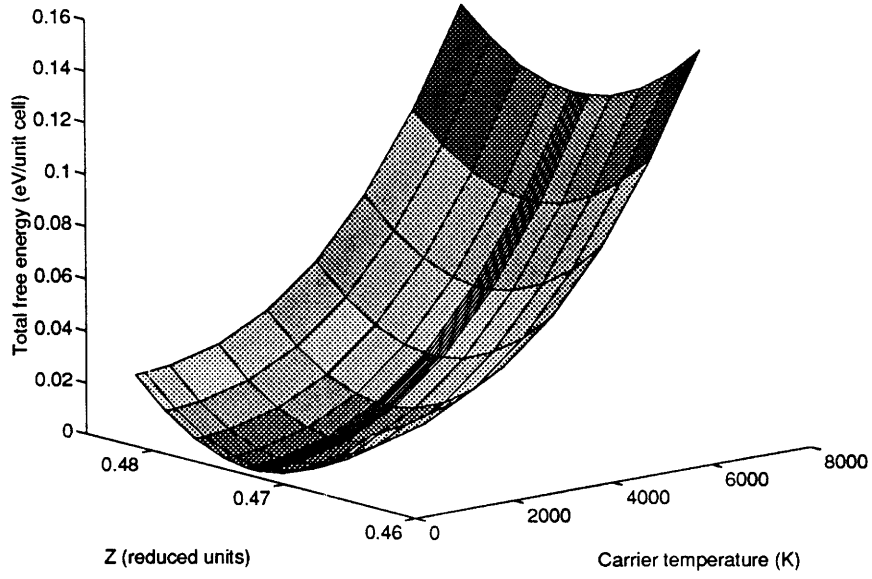

Figure 4-13: Total free energy calculated through the semi-empirical two-band model, as a function of carrier temperature and atomic displacement along the trigonal axis.

$\Delta E(z, T_{el}) = E_{laser}$.

Figure 4-15 shows the graphic determination of the point (z, T_{el}), which corresponds to the crossing of the two curves, $\Delta z = f(T_{el})$ and $\Delta z = e(T_{el})$, obtained by imposing the two conditions described above.

The equilibrium is reached at $T_{el} \simeq 6500$ K and $\Delta z \sim 4$mÅ. The high value for T_{el} indicates that this small temperature model is indeed an approximation, and the analysis is only pertinent when taken as providing an estimate for the size of the effect. An interesting result is that the size of the thermally-induced atomic displacement is the same as that obtained through direct excitation of electron-hole pairs across the band gap at the H point. Also the sign of the displacement coincides with that predicted in the latter case. The numerical agreement between the values of Δz obtained through the two analyses is fortuituous, and cannot be taken but as an estimate of the size of the effect. The fact that Cases 1 and 3 predict the same order of magnitude for the displaced equilibrium of the ions, in the low power regime, allows us to believe that a more complete analysis of the three mechanisms for generation

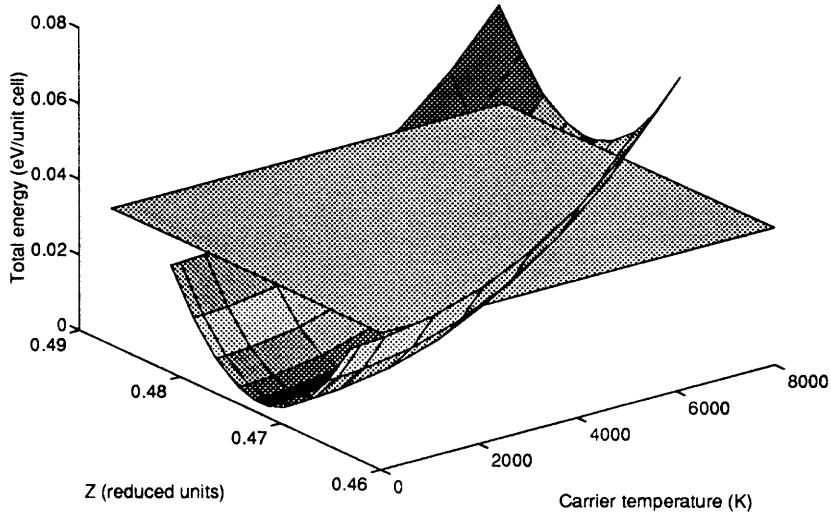

Figure 4-14: Variations of the total energy with respect to its ground state value, calculated through the semi-empirical two-band model, as a function of carrier temperature and atomic displacement along the trigonal axis. The horizontal plane corresponds to the value $\Delta E(z, T_{el}) = E_{laser}$.

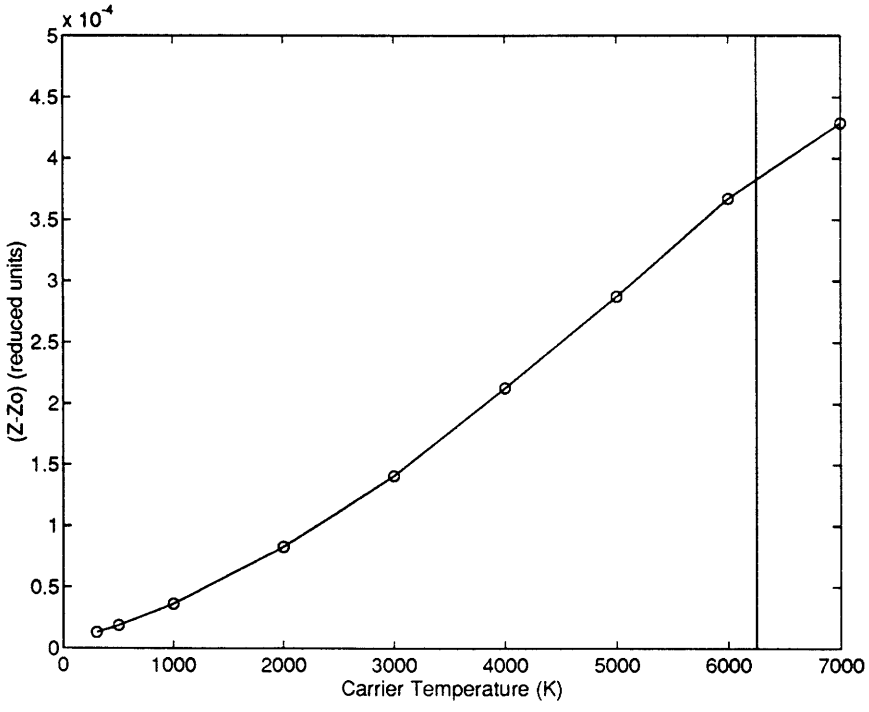

Figure 4-15: Dependences of the atomic equilibrium position on the carrier temperature, $\Delta z = f(T_{el})$ (-o- line) and $\Delta z = e(T_{el})$ (solid line), as determined by the free energy mimimization and the energy conservation conditions, respectively.

of coherent phonons would not change this result.

As well as in the electron-hole generation case, we may expect an increase of the induced atomic displacement with increasing laser power. The laser power dependence of Δz can be easily extracted from the analysis. Nevertheless, the very high carrier temperatures reached in the high power regime invalidate this small temperature model.

The frequency shifts arising from the carrier thermalization can be extracted from the second derivative of the energy of the system at the new equilibrium:

$$\frac{\Delta\nu}{\nu_R} = \frac{\sqrt{\left.\frac{\partial^2 E(z,T_{el})}{\partial z^2}\right|_{(z=z_0+\Delta z;T_{el})}} - \sqrt{\left.\frac{\partial^2 E_{tot}(z)}{\partial z^2}\right|_{z_0}}}{\sqrt{\left.\frac{\partial^2 E_{tot}(z)}{\partial z^2}\right|_{z_0}}}. \tag{4.17}$$

The variation of the frequency in this case is equal to 0.02 %, which is an order of magnitude smaller than the frequency shift produced by the electron-hole pair excitation at H, with the same pump power. This indicates that a rapid carrier thermalization after the arrival of the pump cannot account for the experimental observations of the frequency shifts. Therefore, it is most likely that Case 3 does not play a major role in the generation of coherent phonons. Nevertheless, we cannot totally discard the carrier thermalization as a possible mechanism, because of the lack of a valid treatment of this mechanism at large carrier temperatures. Such a treatment would give us the possibility to compare with the experiments for data points other than the one at low powers.

4.4 Coherent phonon-induced band shifts

In the discussion of the potential occurrence of an ultrafast metal-insulator transition we emphasized the importance of evaluating the band shifts in the vicinity of the band gap.

Such calculations follow directly from the analysis performed in the previous sections. We presented already (see Table 4.1) the derivatives of the bands at the H

Table 4.2: Derivatives of the band energies with respect to atomic dsiplacements along (111) at the band extrema near the band gap, from *ab initio* calculations for Sb.

	$dE/dz(\mathrm{eV}/\mathring{A})$
H(5)	0.[a]
L(6)	−0.36
$E_{\text{gap ind}}$ = L(6) − H(5)	−0.36

[a] The value of the derivative at H is zero because we took this level as the origin of energies (E=0) for all atomic displacements. Therefore, the values of the derivatives for the other bands describe their behavior relative to the top of the valence band H(5).

and L points. Table 4.2 contains the entries for the 5^{th} and 6^{th} bands, as well as the variations of the indirect gap.

Using these data, we can estimate the band gap shift induced by an A_{1g}-phonon coherent motion generated with a high power laser, with an atomic displacement on the order of $0.1\mathring{A}$. This is an upper limit, as non-linear effects will presumably reduce the magnitude of the resulting amplitude of the oscillation. In addition, phonon-phonon scattering processes will dampen the coherent phonon amplitude, and the oscillations will die after a few periods[9].

Table 4.3 contains the band shifts corresponding to this atomic displacement, together with the band gap values to facilitate the discussion. We have sketched this results in Figure 4-16.

The accuracy of our calculations does not allow us to draw final conclusions about the feasibility of an ultrafast metal-insulator transition in Sb. Nevertheless, in the high power experiments, the effect of the laser excitation is a an increase of the band overlap, which is consistent with the presence of a larger number of carriers. However, the size of the effect makes the metal-insulator transition hypothesis plausible in the high power pump-probe experiments with semiconducting $Bi_{1-x}Sb_x$ alloys, if the bands in such alloys show a similar behavior to Sb. If the additional condition, that

[9]Nevertheless, the oscillations can be maintained by illuminating the material with pumps at intervals of a few A_{1g}-mode oscillation periods.

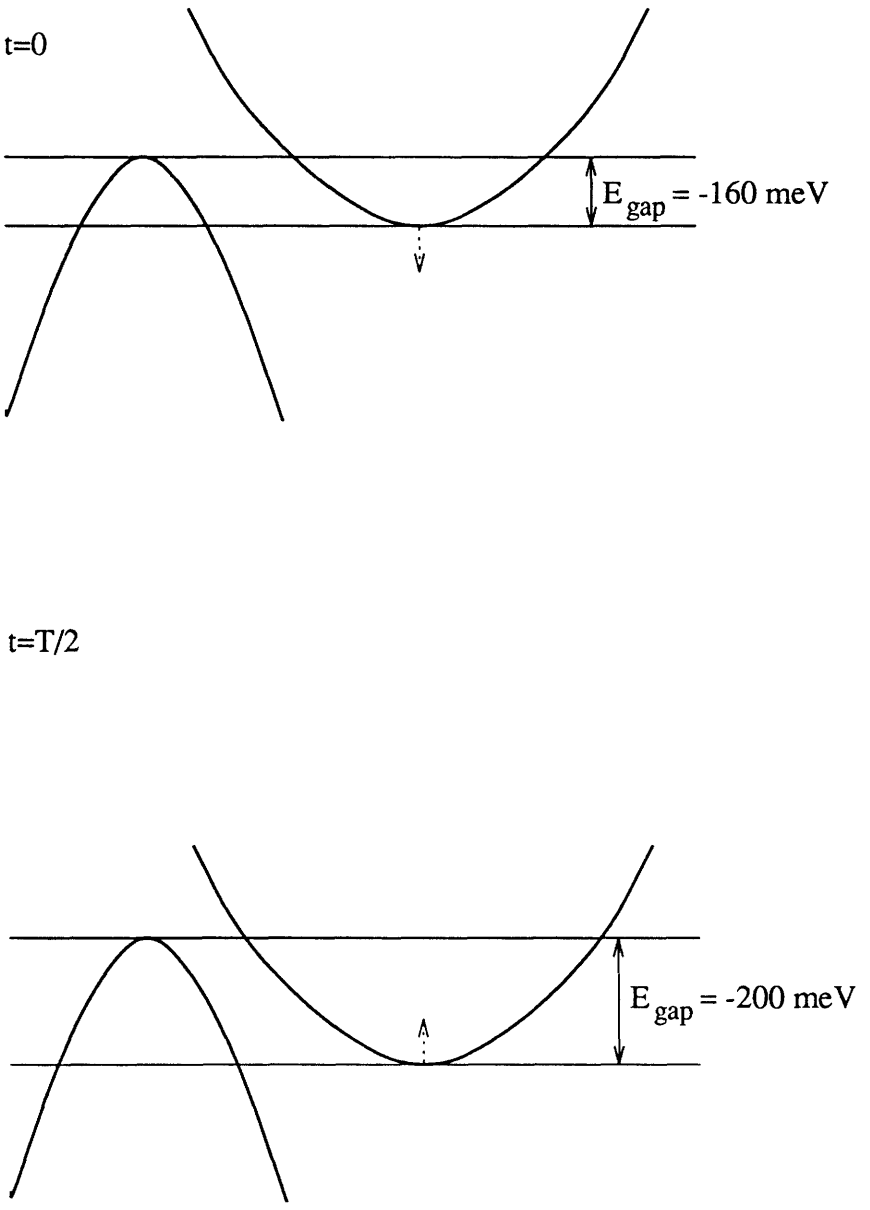

Figure 4-16: Band gap modulation in Sb, induced by laser-excited coherent phonons with A_{1g} symmetry and vibrational amplitude $\sim 0.1\mathring{A}$.

Table 4.3: Band gap values and shifts produced by a 0.1$\AA$ atomic displacement along (111), as predicted by the analysis of the *ab initio* calculations in Sb.[a]

	Ab initio	Experiment
$E_{gap\ ind}$	-555	-160[b]
$\Delta E_{gap\ ind}$	-36	No[c]

[a] All energies in meV.
[b] Reference [28].
[c] Would the modulation of the energy gap induced by the A_{1g}-phonon change the signs of the gap during the coherent oscillation?

the intervalley scattering rate between holes and electrons be larger than the phonon frequency, is fulfilled, it will lead to a metal-insulator transition at a THz frequency.

Once the spin-orbit coupling is introduced, and we predict the correct ordering of the bands, we can already improve the evaluation of the A_{1g}-phonon amplitude and frequency shifts, even if we do not know the matrix elements for optical transitions. We may get around the lack of knowledge of these matrix elements by considering all the transitions equally probable. Moreover, we will also be able to calculate the imaginary part of the dielectric constant in terms of the joint density of states. Using this equiprobability approximation, we could then directly calculate the force on $atom_2$ produced by all possible 2 eV optical excitations in the Brillouin zone. This force would be obtained by means of a total energy self-consistent calculation in which the occupation of the levels would be modified. If in the ground state calculations we took the five valence bands to be completely filled and the higher bands empty, in the excited state case some lower bands will be partially emptied in favor of some higher bands gaining electrons.

In the event that we cannot have the complete spin-orbit calculations, but we can evaluate the matrix elements for optical transitions, the force on $atom_2$ can also be estimated. In this case, we would proceed by calculating the optical spectrum of Sb without spin-orbit, and we would compare it with experimental results. The effect of neglecting the spin-orbit coupling term in the optical spectrum is an overall shift in photon frequency by a constant value. Thus, we can identify, by means of

this comparison with experiment, which transitions contribute to the displaced 2 eV peak. Then, we proceed to modify the occupation numbers of the levels involved in the optical transitions, and then calculate self-consistently the force on $atom_2$.

Finally, we compare the values of the band derivatives (Table 4.2) with those obtained from the perturbative pseudopotential analysis (Table 3.2). In the nearly free electron approach the magnitude of the band shift was overestimated. This disagreement newly demonstrates that only through very accurate calculations can we obtain a good description of physical processes taking place in the vicinity of the band gap of these narrow-gap materials.

4.5 Time evolution of the coherent phonons

Up to this point, we have only analyzed theoretically the initial changes in the oscillatory component of the reflectivity, which are linked to the mechanism of generation of coherent phonons.

In this section, we will discuss the procedure for extending our theoretical calculations to study how the coherent phonons evolve in time. In the power-dependent study of the coherent phonons (Section 2.3), we found experimental evidence that the mechanism for the frequency downshift and later recovery was the screening produced by the excited carriers. We shall now analyze this statement within the theoretical framework that we have developed in this chapter.

The effect of the electronic screening is included in our mathematical formalism in terms of the changes in occupation number of a level i, Δf_i, caused by the electronic excitation. We assume that the excited carrier population decays exponentially back to the ground state, with a characteristic decay time τ_{el}. Therefore:

$$\Delta f_i(t) = \Delta f_i(0) e^{-t/\tau_{el}}. \tag{4.18}$$

After the pump-induced electronic excitation, the atomic equilibrium coordinate is shifted by Δz, although the atoms are still located at their pre-pump equilibrium position. The new potential acting on the atoms produces a force which causes them

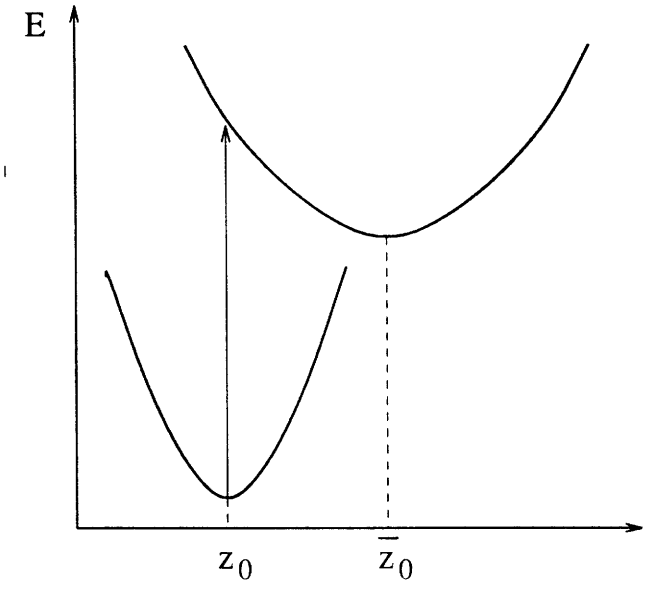

Figure 4-17: Schematic picture of the pump-induced coherent atomic motion due to a quasi-instantaneous change of equilibrium position.

to move (see Figure 4-17). We will solve the equation of motion for the displacements of atom_2 relative to atom_1.

The equation of motion for a particle of mass m under some external force $F(t)$ is given by Newton's second law:

$$m \cdot \ddot{z}(t) = F(t) \tag{4.19}$$

Using the definition of the second derivative of a function, the acceleration of the particle can be expressed in terms of its positions:

$$\ddot{z}(t) = \overset{lim}{\delta t \to 0} \frac{z(t+\delta t) + z(t-\delta t) - 2z(t)}{\delta t^2} \tag{4.20}$$

Therefore, if we know the positions of the atom at $z(t-\delta t)$ and $z(t)$, and also the force acting upon it, $F(t)$, we can find the atomic position at any later time as

$$z(t+\delta t) = \frac{F(t)}{m}\delta t^2 + 2z(t) - z(t-\delta t). \tag{4.21}$$

The force exerted on the atom by the pump-excited system with energy $E(t)$ is simply

$$F(t) = -\frac{\partial E(t)}{\partial z}\Big|_{(z(t),\Delta f_i(t))}. \tag{4.22}$$

The total energy of the system in the excited state can be expanded about its minimum in a similar fashion as we did in equation (4.5) for the ground state. In Section 4.3.1 (eq. (4.8)) we obtained an expression for the new equilibrium, $\overline{z}_0$, which is displaced from its pre-pump value by $\Delta z(0)$, namely:

$$\overline{z}_0 = z_0 + \Delta z(0) = z_0 - \frac{\Sigma_i \frac{\partial \epsilon_i}{\partial z}\Big|_{z_0} \Delta f_i(0)}{\frac{\partial^2 E}{\partial z^2}\Big|_{(z_0;\Delta f_i(0)=0)} + \Sigma_i \frac{\partial^2 \epsilon_i}{\partial z^2}\Big|_{z_0} \Delta f_i(0)}, \tag{4.23}$$

where we have implicitly stated that the change of occupation numbers is evaluated at zero time delay.

In the harmonic approximation, we can expand the total energy of the system as

$$\begin{aligned} E(z(t);\Delta f_i(t)) = \; & E(\overline{z}_0;\Delta f_i = 0) + \Sigma_i \epsilon_i(\overline{z}_0)\Delta f_i \\ & + \left[\frac{\partial E}{\partial z}\Big|_{(\overline{z}_0;\Delta f_i(0))} + \Sigma_i \frac{\partial \epsilon_i}{\partial z}\Big|_{\overline{z}_0} (\Delta f_i(t) - \Delta f_i(0))\right](z(t) - \overline{z}_0) \\ & + \frac{1}{2}\left[\frac{\partial^2 E}{\partial z^2}\Big|_{(\overline{z}_0;\Delta f_i(0))} + \Sigma_i \frac{\partial^2 \epsilon_i}{\partial z^2}\Big|_{\overline{z}_0} (\Delta f_i(t) - \Delta f_i(0))\right](z(t) - \overline{z}_0)^2 \end{aligned} \tag{4.24}$$

Notice that we could eventually go beyond the harmonic approximation and solve the numerically the exact equation of motion for the ions coupled to the time-dependent excited electronic state. The exact equation is obtained by replacing the Taylor expansion of the total energy by $E(z(t);\Delta f_i(t))$, which is evaluated at each time by means of an *ab initio* simulation. In the present treatment, we are studying the effect of the time-evolving "electronic degrees of freedom" on a harmonic atomic potential. The aim of this study is, thus, to predict the qualitative trends of the microscopic evolution of the coherent phonons after the displacive excitation.

From equation (4.24), we can find the time-dependent force acting on atom$_2$:

$$\begin{aligned} F(t) = & -\frac{\partial E}{\partial z}\Big|_{(\bar{z}_0;\Delta f_i(0))} - \Sigma_i \frac{\partial \epsilon_i}{\partial z}\Big|_{\bar{z}_0} (\Delta f_i(t) - \Delta f_i(0)) \\ & + \Big(\frac{\partial^2 E}{\partial z^2}\Big|_{(\bar{z}_0;\Delta f_i(0))} - \Sigma_i \frac{\partial^2 \epsilon_i}{\partial z^2}\Big|_{\bar{z}_0} (\Delta f_i(t) - \Delta f_i(0)) \Big)(z(t) - \bar{z}_0). \end{aligned} \tag{4.25}$$

The new equilibrium is a minimum of the excited state energy, and the first derivative of the energy at this point vanishes:

$$\frac{\partial E}{\partial z}\Big|_{(\bar{z}_0;\Delta f_i(0))} = 0. \tag{4.26}$$

If we make explicit the time dependence of the occupation numbers, given by equation (4.18), the final expression for the force is

$$\begin{aligned} F(t) = & -\Sigma_i \frac{\partial \epsilon_i}{\partial z}\Big|_{\bar{z}_0} \Delta f_i(0)(e^{-t/\tau_{el}} - 1) \\ & - \Big(\frac{\partial^2 E}{\partial z^2}\Big|_{(\bar{z}_0;\Delta f_i(0))} + \Sigma_i \frac{\partial^2 \epsilon_i}{\partial z^2}\Big|_{\bar{z}_0} \Delta f_i(0)(e^{-t/\tau_{el}} - 1) \Big)(z(t) - \bar{z}_0). \end{aligned} \tag{4.27}$$

The time-dependent "frequency", $\nu(t) = \omega(t)/2\pi$, is connected to the curvature of the total energy parabola, $E(t)$, through:

$$m\omega^2(t) = \frac{\partial^2 E}{\partial z^2}\Big|_{(\bar{z}_0;\Delta f_i(0))} + \Sigma_i \frac{\partial^2 \epsilon_i}{\partial z^2}\Big|_{\bar{z}_0} \Delta f_i(0)(e^{-t/\tau_{el}} - 1), \tag{4.28}$$

where the curvature at the new equilibrium was found in Section 4.3.1 to be

$$m\omega^2(0) = \frac{\partial^2 E}{\partial z^2}\Big|_{(\bar{z}_0;\Delta f_i(0))} = \frac{\partial^2 E}{\partial z^2}\Big|_{(z_0;\Delta f_i=0)} + \Sigma_i \frac{\partial^2 \epsilon_i}{\partial z^2}\Big|_{z_0} \Delta f_i(0). \tag{4.29}$$

From equation (4.28), we see that the characteristic relaxation time of the frequency back to its spontaneous Raman value, which we called τ_{pf} in previous sections, is equal to the carrier relaxation time τ_{el}, for small power excitations. Experimentally, we observed a linear dependence of the frequency shifts (Figure 2-5) and oscillation amplitude (Figure 2-4) at zero time delay with pump power. In this linear regime,

$\tau_{el} \approx \tau_{pf}$, which means that the decay time for the carrier excitation can be empirically determined from the relaxation time of the frequency shift in the pump-probe data.

Finally, introducing the expression of the force (eq. (4.27)) in the equation of motion for atom$_2$ (eq. (4.21)), and taking all the above considerations into account, we obtain:

$$\begin{aligned} z(t+\delta t) = & -\Sigma_i \frac{\partial \epsilon_i}{\partial z}\Big|_{\overline{z}_0} \frac{\Delta f_i(0)}{m}(e^{-t/\tau_{pf}} - 1)\delta t^2 \\ & -\left[\omega^2(0) + \Sigma_i \frac{\partial^2 \epsilon_i}{\partial z^2}\Big|_{\overline{z}_0} \frac{\Delta f_i(0)}{m}(e^{-t/\tau_{pf}} - 1)\right]\delta t^2 (z(t) - \overline{z}_0) \\ & +2z(t) - z(t-\delta t). \end{aligned} \tag{4.30}$$

This equation can be solved by recurrence, once the values of two positions very close in time are known. It is clear that, at zero time delay, atom$_2$ is located at the pre-pump equilibrium position z_0. If the atom starts to move towards this new equilibrium, its position a small time later δt can be found by assuming that it behaves harmonically during this small time interval. Thus, the motion of atom$_2$ at a short time δt after the arrival of the pump pulse can be described by Hook's law:

$$\ddot{z}(t) = -\omega^2(0)(z(t) - \overline{z}_0), \tag{4.31}$$

with the boundary conditions $z(0) = z_0$ and $\dot{z}(0) = 0$. The solution for this equation is

$$z(t) = z_0 + (\overline{z}_0 - z_0)(1 - cos\omega(0)t) = z_0 + \Delta z(0)(1 - cos\omega(0)t), \tag{4.32}$$

which can be approximated, for short times δt, to

$$z(\delta t) \approx z_0 + \frac{1}{2}\Delta z(0)(\omega(0)\delta t)^2. \tag{4.33}$$

In order to calculate the atomic motion from equation (4.30), we need the values of the first and second derivatives of the bands involved in the optical transition, evalu-

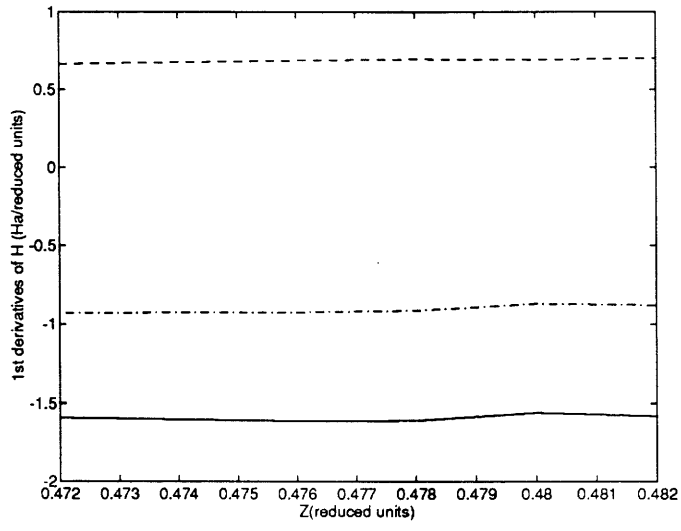

Figure 4-18: First derivatives of the eigenvalues of bands H(4) (dashed line), H(6) (dash-dotted line) and [H(6)-H(4)] (solid line), as a function of $atom_2$ displacement along the trigonal axis, as obtained from our *ab initio* calculations. The ground state equilibrium position is $z_0 = 0.4734$.

ated at the equilibrium of the excited electronic state. We have plotted in Figures 4-18 and 4-19 the values of those derivatives as a function of atomic displacement, for the case of electron-hole pairs created at the H point as a result of an optical transition between the 4^{th} occupied band and the 6^{th} unoccupied band.

From these figures, we see that the first derivatives remain almost constant with atomic displacement, whereas there is a rather large dispersion in the second derivatives of the eigenvalues with respect to atomic position. This is due to the error in calculating these derivatives. As an approximation, we will evaluate the first and second derivatives of the eigenvalues of the bands involved at the ground state equilibrium position.

In order to visualize the solution of the equation of motion (4.30), we consider the case of a electron-hole pair excitation between the 4^{th} and 6^{th} band at the H point. Figure 4-20 shows the trajectories followed by the coherent phonons at different pump powers. The decay times of the electronic excitation are taken from the pump-probe data, as well as the change of occupation numbers at zero time delay.

The atomic trajectories reproduce very well the main features of the modulated

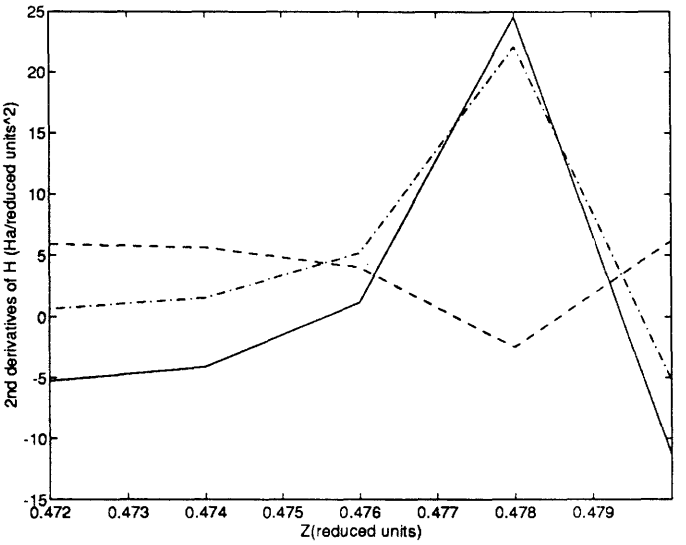

Figure 4-19: Second derivatives of the eigenvalues of bands H(4) (dashed line), H(6) (dash-dotted line) and [H(6)-H(4)] (solid line), as a function of atom$_2$ displacement along the trigonal axis, as obtained from our *ab initio* calculations. The ground state equilibrium position is $z_0 = 0.4734$.

reflectivity pump-probe data (see Figure 2-3), namely, a cosine-behaviour, large amplitude oscillations and a negative shift of the vibrational frequency, which is larger in absolute value for higher powers. In the plot of the atom dynamics for long times (Figure 4-21), we observe the decay of the displaced equilibrium coordinates back the ground state equilibrium position, as well as a return of the frequency to its spontaneous Raman value.

The evaluation of the damping time of the oscillations, τ_{ph}, requires a study of the different decay channels of the A_{1g} phonon via phonon-phonon scattering.

The fact that the atom motion cannot be described as a simple function of time indicates that the decay time of the electronic population, τ_{el}, is different from the decay time of the equilibrium coordinates, which we will call τ_z. In the pump-probe reflectivity data, τ_z is traced by the decay time of the background, which was equated to τ_{el} for simplicity. The appropriate fitting expression for the modulated reflectivity

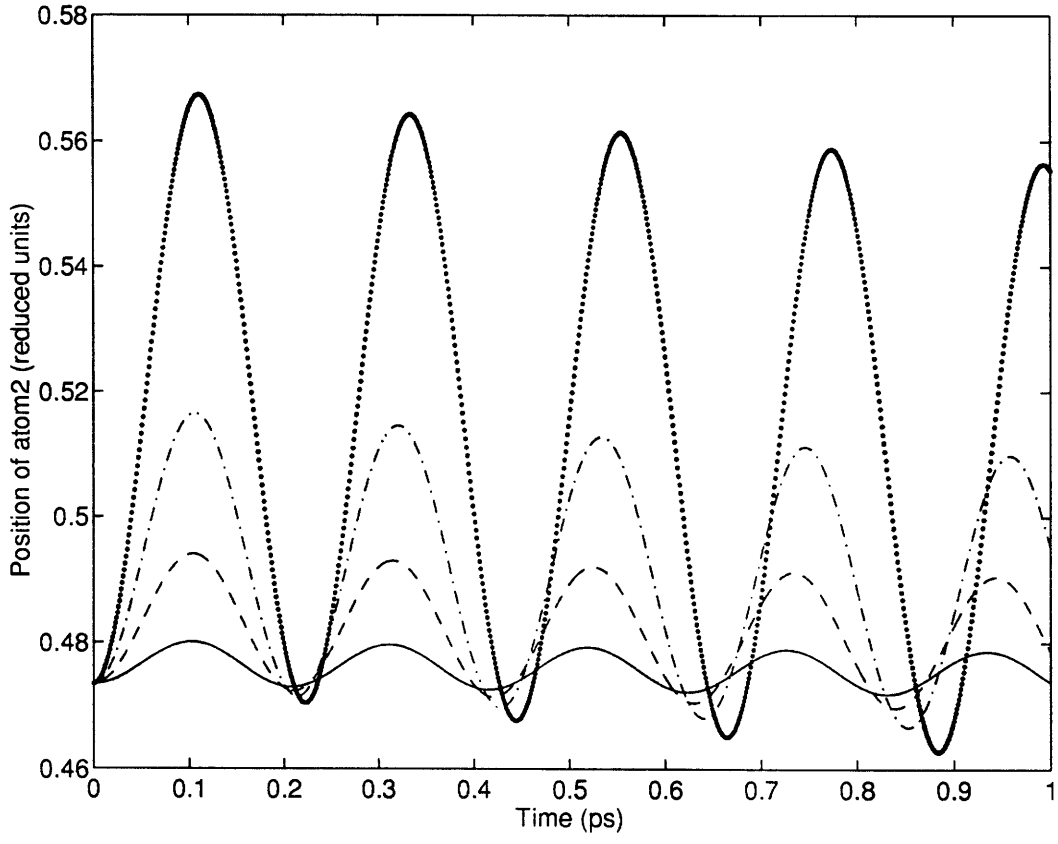

Figure 4-20: Trajectories of $atom_2$ with respect to $atom_1$ for Sb at different pump powers, P_{pump} = 2 mW (solid line), 6 mW (dashed line), 12 mW (dash-dotted line) and 24 mW (dotted line). These traces reproduce the main features of the displacive generation of coherent phonons, namely, a cosine-behaviour, large amplitude oscillations and a negative shift of the vibrational frequency.

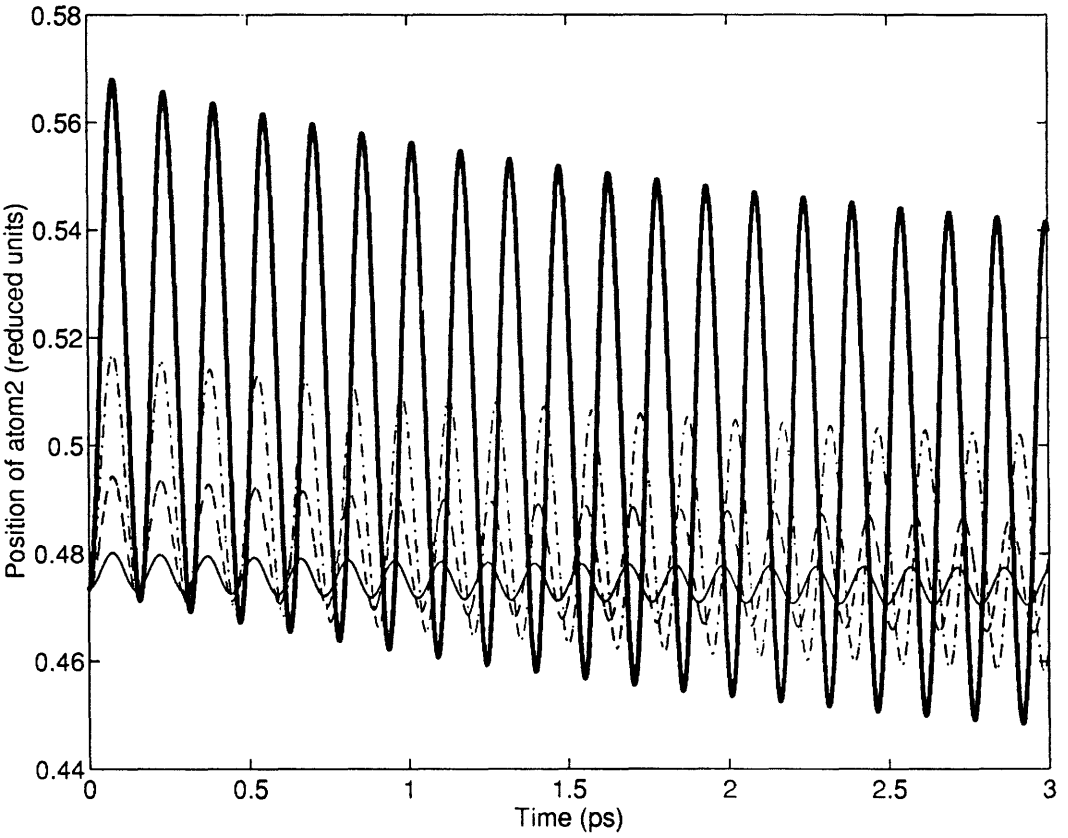

Figure 4-21: Trajectories of $atom_2$ with respect to $atom_1$ for Sb at different pump powers, P_{pump} = 2 mW (thin solid line), 6 mW (dashed line), 12 mW (dash-dotted line) and 24 mW (thick solid line). As the DECP model predicts, the displaced equilibrium coordinates decay back to the ground state equilibrium position, and the frequency of the phonon oscillations returns to its spontaneous Raman value.

at high powers is

$$\left(\frac{\Delta R}{R}\right)_{system} = A \cdot e^{-t/\tau_{el}} + B \cdot (e^{-t/\tau_z} - e^{-t/\tau_{ph}} cos\omega_0(t)t) + C. \qquad (4.34)$$

instead of Equation (1.10). Unfortunately, the fact that the coefficient of the pure electronic decay term A is in general about an order of magnitude smaller than the amplitude of the $\Delta R/R$ oscillatory component, B (see Table 1.1), makes it impossible to determine τ_{el} from fits to the pump-probe data. Actually, the background decay time presented in the experimental fits corresponds to τ_z, rather than τ_{el}.

4.6 Conclusions

In this chapter we have performed first-principles calculations of the phenomenon of generation of coherent phonons and their subsequent evolution in time for Sb.

This study gives evidence that the A_{1g} symmetry coherent atomic motion is a result of an electronic excitation which instantaneously displaces the ground state equilibrium coordinate of the ions. The agreement with experimental pump-probe data points to the electron-hole pair creation at specific k-points in the Brillouin zone as a mechanism for generation of the coherent phonons. These excitations could cause atomic displacements along the trigonal axis on the order of $0.1\mathring{A}$, or $\sim 1\%$ of the lattice parameter in this direction.

We have also evaluated the band modulations in the vicinity of the Fermi level which result from this coherent atomic displacement. Although the accuracy of our calculations does not allow us to a give conclusive answer, it is unlikely that the band gap in Sb reverses its sign at a terahertz frequency, when the material is illuminated by a high power short laser pulse. Nevertheless, such metal-insulator transition could occur when the pump-probe experiment is performed with semiconducting $Bi_{1-x}Sb_x$ alloys.

Chapter 5

Semi-empirical calculation of background decay times

Femtosecond pulse pump-probe experiments provide a very valuable tool to study the dynamics of the electron-phonon coupled system in a solid. It is of fundamental importance to develop theoretical models which can explain the microscopic evolution of the material in the excited state from the transient optical signal. We have concentrated most of our work on the phenomenon of coherent phonon generation because of its uniqueness. Nevertheless, some additional information can be extracted from a theoretical study of the background decay times of the transient reflectivity signal. Of particular interest are materials which undergo metal-insulator transitions. For such systems, a calculation of the dependence of the characteristic decay times on the parameters which control the transition can allow us to identify which microscopic changes are occurring.

Combining the DECP theory with simplified band models for both the $Bi_{1-x}Sb_x$ alloys at different compositions, and also for Ti_2O_3 at different temperatures, we can better understand the evolution of the coupled carrier and lattice dynamics throughout the transition.

5.1 Experimental results

In this section, we present the experimental analysis of the effective background decays from the pump-probe studies of the Ti_2O_3 and $Bi_{1-x}Sb_x$ systems in the vicinity of their metal-insulator transitions. A more complete analysis of these experiments is contained in T. K. Cheng's doctoral dissertation [6].

The pump-probe study of the $Bi_{1-x}Sb_x$ alloys was introduced in Section 2.4.1. The very low thermal conductivity in Bi, and also in the $Bi_{1-x}Sb_x$ alloys with small Sb content, causes the temperature of the illuminated spot to approach the melting point on typical experimental time scales. A lattice heating effect was observed in Figure 2-14, insofar as the background of the reflectivity signal does not return to the pre-pump value. As a result, there is a great uncertainty in the determination of the background decay time, τ_{el}.

In Section 2.4.2 (Figures 2-18 and 2-19) we showed the temperature dependent pump-probe reflectivity data for Ti_2O_3. The most striking feature of the data is the temperature-dependent behavior of the effective decay time for the excited carriers, τ_{el}, which we plot in Figure 5-1. The electron relaxation times decrease rather sharply in the vicinity of the transition, from $\sim$300 fs to $\sim$100 fs, as the material turns metallic. In Chapter 2, we introduced the modulated reflectivity experiments as a tool to study changes in the band structure, which produce modifications in the interband contribution of the dielectric constant, $\epsilon(\omega)$. In the case of Ti_2O_3, the fact that the background decay shows such a strong correlation with the metal-insulator transition indicates that the pump-induced electronic excitations take place between bands which are largely modified across the transition. As we previously mentioned, the strong variation with temperature of many macroscopic properties of Ti_2O_3 in the range from 300 K to 600 K have been explained as a result of a change of sign of the indirect band gap. Therefore, we can make the hypothesis that there is also an association between the sudden drop of τ_{el} and the changing of the transport properties of the material from semiconducting to semimetallic. This hypothesis is based on the possibility that the pump-induced transitions occur between an occupied

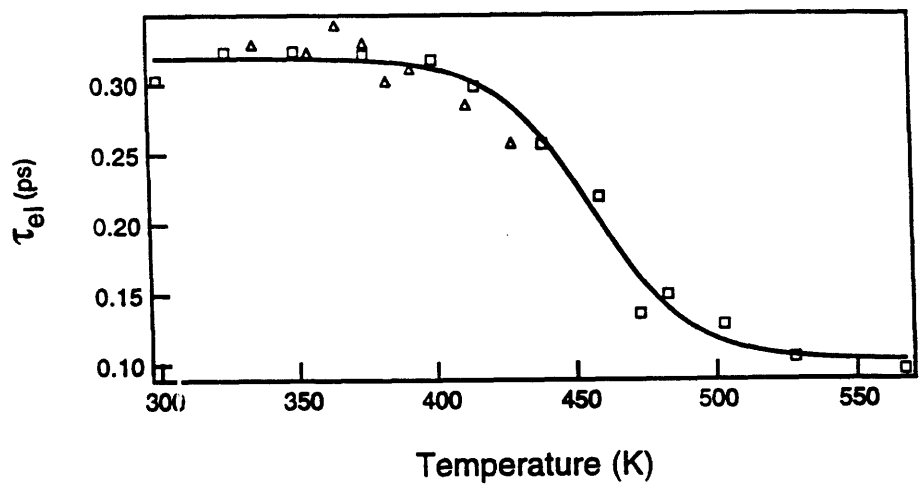

Figure 5-1: Temperature-dependence of the decay time of $\Delta R/R$, τ_{el}, for Ti_2O_3 across the semiconductor-semimetal transition, extracted from temperature-dependent pump-probe data. The estimated error in the calibration of the temperature is ± 30 K. [6]

band 2 eV below the Fermi level and either the valence or the conduction band. The inaccurate knowledge of the band structure of Ti_2O_3 prevents a quantitative confirmation of such a hypothesis, but it is clear that the change of carrier density throughout the transition would modify the optical response of the material to the pump excitation. The combined effect of a higher density of intrinsic carriers in the semimetallic phase, and the presumably faster intervalley scattering time between electrons and holes, would accelerate the decay process of the laser excitation.

In the Bi-Sb system, optical data show the existence of several transitions between bands at 2 eV below the Fermi level and the conduction and valence bands[1]. It is then plausible to extend the hypothesis made for Ti_2O_3 to the $Bi_{1-x}Sb_x$ alloys, in order to predict theoretically the decay times for the background of the transient reflectivity signal.

The fact that we neither know at which exact k-points in the Brillouin zone the laser-induced transitions are occurring, nor do we know the value of the matrix element for such transitions, will oblige us to make further simplifications. In this

[1]See Landolt and Börnstein [28], **III/17e**, pp. 39 ff. and 47 ff., and references therein.

chapter, we will develop two-band models from which we will calculate the carrier-phonon scattering rate.

5.2 Electronic relaxation via electron-phonon interaction

Allen [54] developed a theory for metals which connected the macroscopic background relaxation of the transient modulated reflectivity signal, $\Delta R/R$, with a microscopic picture. The principal mechanism for the recovery of $\Delta R/R$ to its pre-pump value is the scattering of the excited carriers with phonons. The relaxation of the non-equilibrium excited carrier population to a quasi-equilibrium state via electron-electron scattering is believed to take place in times shorter than the pulse width, which means that such processes cannot be observed in our experiment.

Allen's formalism can be extended to semimetals, which have a metallic-like character, in the sense that there is a band overlap, and also that the dynamics due to the laser excitation occurs near to the Fermi level. In semimetals, however, two types of carriers are present and both electrons and holes need to be considered. For illustrative purposes, we will treat all the carriers as electrons, and at a later stage we will distinguish between electrons and holes in writing the final expressions.

The rate of change of the electronic distribution, f_k, due to electron-phonon scattering processes is given by [54]

$$\frac{\partial f_k}{\partial t} = -\frac{2\pi}{\hbar}\Sigma_{k'}|M_{k,k'}|^2\{f_k(1-f_{k'})[(n_q+1)\delta(\epsilon_k-\epsilon_{k'}-\hbar\omega_q)+n_q\delta(\epsilon_k-\epsilon_{k'}+\hbar\omega_q)]$$

$$-(1-f_k)f_{k'}[(n_q+1)\delta(\epsilon_k-\epsilon_{k'}+\hbar\omega_q)+n_q\delta(\epsilon_k-\epsilon_{k'}-\hbar\omega_q)]\}, \tag{5.1}$$

where $\mathbf{k}$ and $\mathbf{k}'$ denote the wave vectors for the electrons in the initial and final states and $\mathbf{q}$ those of the phonons, with $\mathbf{k} = \mathbf{k}' \pm \mathbf{q}$, in order to satisfy conservation of momentum. Each distribution function, f_k for electrons and n_q for phonons, is taken

to be in local equilibrium at a temperature $T_{el}(t)$ and T_L, respectively:

$$f_k(t) = \frac{1}{e^{\frac{\epsilon_k - E_F}{k_B T_{el}(t)}} + 1}; \qquad n_q = \frac{1}{e^{\frac{\hbar\omega_q}{k_B T_L}} - 1}. \tag{5.2}$$

The system will reach equilibrium at a time t' when the electron and lattice temperatures are equal, $T_{el}(t') = T_L$. In the preceding definitions, we have assumed that the lattice temperature reimains essentially constant during the electronic relaxation process. In Figure 5-2 we illustrate the effect of the pump on the carrier distribution. The pump-induced electronic excitation across the band gap produces a sharply peaked distribution of non-equilibrium carriers. This distribution relaxes back to a Fermi-Dirac quasi-equilibrium distribution via electron-electron scattering on a time scale smaller than the pulsewidth. The quasi-equilibrium distribution is characterized by a carrier temperature, T_{el}, that is higher than the lattice temperature, T_L. Finally, the quasi-equilibrium carrier system achieves equilibrium by interacting with the phonons until $T_{el} = T_L$. This electron-phonon relaxation process, which happens on a time scale larger than the pulsewidth and can be observed experimentally, is the object of the present calculation.

In the relaxation time approximation, the rate of energy change of the electronic distribution function, due to electron collisions with the lattice, defines the electronic decay time τ_{el}

$$\frac{\partial E_{el}}{\partial t} = 2\Sigma_k \epsilon_k \frac{\partial f_k}{\partial t} = -\frac{\Delta E}{\tau_{el}} \tag{5.3}$$

where ϵ_k is the energy of an electron of wave vector k, and ΔE is the energy per unit volume given by the laser to the electron system.

We express the electron-phonon interaction matrix element, $M_{k,k'}$, via a deformation potential theory [55]. This theory connects the band gap shifts in a semiconductor with the lattice motions which produce these shifts. The lattice displacements are caused by some field, such as a pressure, a stress or a laser-excited change in the electronic distribution, which modifies the potential seen by the ions. The resulting lattice distortions generate a phonon field which interacts with the carriers, thus shifting the electron bands.

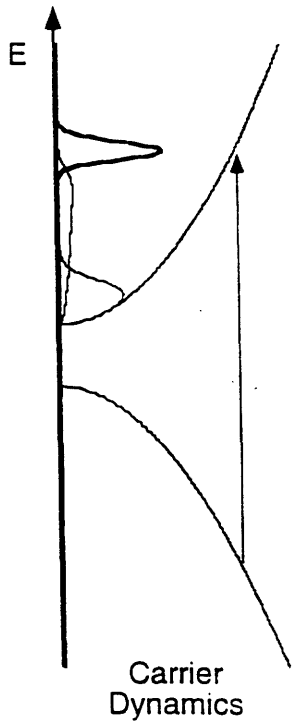

Figure 5-2: Schematic representation of the transient evolution of the pump-excited carriers. (From [6])

The effect of the phonon field is included in the microscopic formalism by means of a perturbative term in the electronic Hamiltonian:

$$\delta U(\mathbf{r}) = \mathbf{E_1}\boldsymbol{\Delta}(\mathbf{r}), \tag{5.4}$$

where $\Delta(\mathbf{r})$ is a characteristic amplitude of the phonon field acting on the carriers, and E_1 is the deformation potential constant, which contains information on how strongly the gap couples to the phonon field. In the case of a pressure or a stress acting on the system, there will be a net change in the volume of the unit cell, and the resulting deformation potental is called acoustic. In our transient-modulated reflectivity experiments, the pump-induced changes in electronic distribution cause a phonon field with the fully symmetric A_{1g} symmetry, and the volume of the unit cell remains unmodified. By analogy, we can speak of an optical deformation potential constant.

The interaction matrix between the phonon field and the free carriers, $M_{k,k'} = \int \psi^*(\mathbf{r},\mathbf{k}')\delta\mathbf{U}(\mathbf{r})\psi^*(\mathbf{r},\mathbf{k})\mathbf{dr}$, is given in the deformation potential theory [55]

as

$$|M_{k,k'}|^2 = \frac{A_q^2 E_1^2}{N\langle x_q^2\rangle} \tag{5.5}$$

where N is the number of ions per unit volume, $A_q^2 = k_B T_L/(2M\omega_q^2)$ is the square of the oscillator amplitude in which M is the ion mass, $\sqrt{\langle x_q^2\rangle}$ is the root mean square amplitude of the phonons involved, and E_1 is the deformation potential constant:

$$\Delta E_g = E_1 \Delta; \qquad \Delta = \epsilon_{ij} \tag{5.6}$$

and ϵ_{ij} denotes the component of the elastic constant along the direction of the phonon field.

Equations (5.1), (5.3) and (5.5) lead to the following expression for the decay time:

$$\frac{1}{\tau_{el}} = \frac{\hbar E_1^2}{\pi\rho\langle x_q^2\rangle \Delta E}(k_B T_{el} - n_q \hbar\omega_q)\int \frac{d^3k}{(2\pi)^3}\frac{\partial f_k}{\partial \epsilon_k}\left(\frac{\partial \epsilon_k}{\partial k}\right)^{-1} k^2 \tag{5.7}$$

where $\rho = NM$ is the density of the material, and the integral over momenta includes all types of carriers. If we model the conduction and valence bands for the system under study as rigid parabolic bands, the integral on the right-hand side of equation (5.7) can be expressed as a Fermi-Dirac integral[2], f_2. If we further make the effective mass approximation, equation (5.7) takes the form:

$$\frac{1}{\tau_{el}(y)} \simeq C(E_1)\overbrace{\left[1 - \frac{\hbar\omega_q}{k_B T_{el}} n_q\right]}^{phonons} \times$$

$$\overbrace{\times \left\{\overbrace{\left(\frac{m_e}{m_0}\right)^3 f_2\left[exp\left(-\frac{2E_F(y) - E_g(y)}{2k_B T_{el}}\right)\right]}^{electrons} + \overbrace{\left(\frac{m_h}{m_0}\right)^3 f_2\left[exp\left(\frac{2E_F(y) + E_g(y)}{2k_B T_{el}}\right)\right]}^{holes}\right\}}^{carriers} . \tag{5.9}$$

[2]The Fermi-Dirac integrals are defined as:

$$f_n(z) = \frac{1}{\Gamma(n)}\int_0^\infty \frac{x^{n-1}dx}{z^{-1}e^x + 1}, \tag{5.8}$$

where $\Gamma(n)$ is the Gamma function. See, for example, the Appendix E of Pathria [45], for the definition and properties of the Fermi-Dirac integrals.

Here, y is a generic label for the parameter which controls the metal-insulator transition, and would be replaced by the temperature $T = T_L$ in Ti_2O_3, and by the alloy composition x in the Bi-Sb system. $C(E_1)$ is a factor which is independent of y:

$$C(E_1) = \frac{2\langle x_q^2 \rangle {E_1}^2 {m_0}^3 (k_B T_{el})^2}{\pi^3 \hbar^5 \Delta E \rho}, \tag{5.10}$$

In the following sections, we will apply this formalism to the study of τ_{el} for specific materials.

5.3 $Bi_{1-x}Sb_x$ alloys

We have evaluated τ_{el} at the two compositions for which pump-probe data were shown in Figure 2-14. For $x = 1\%$, the almost pure Bi sample is semimetallic with an indirect band gap of -25 meV between the bottom of the conduction band (CB) at the L point and the top of the valence band (VB) at the T point (see Figure 5-3(a)). Thus, the carrier pockets are localized at the L and T points, for electrons and holes, respectively, with an intrinsic carrier density at room temperature on the order of 10^{18}cm^{-3}. At $x = 12\%$, the alloy is semiconducting with a direct gap of 25 meV at the L point. The T point for $Bi_{.88}Sb_{.12}$ lies well below the Fermi level, which is now in the middle of the band gap (Figure 5-3(b)). In this case, the 5^{th} band is filled at the T point, and most of the thermally excited carriers are localized at the L point. As a result, the intrinsic carrier density for this semiconducting alloy at room temperature is an order of magnitude smaller than that of pure Bi.

For small Sb concentrations, the masses can be approximated to the average effective masses of the carriers in Bi[3]. These are $m_L = 0.05m_0$, at the L point, and $m_T = 0.15m_0$, at the T point.

The effect of the pump is to add $3 \times 10^{20}\text{cm}^{-3}$ carriers for the case of Bi, Sb and their mixed alloys[7]. In an analogous fashion as in the discussion of the carrier thermalization in the previous chapter (Section 4.3.3), the Fermi energy and

[3]Like in the previous sections, we define the average effective mass as $\sqrt[3]{det(\overleftrightarrow{m}^*)}$.

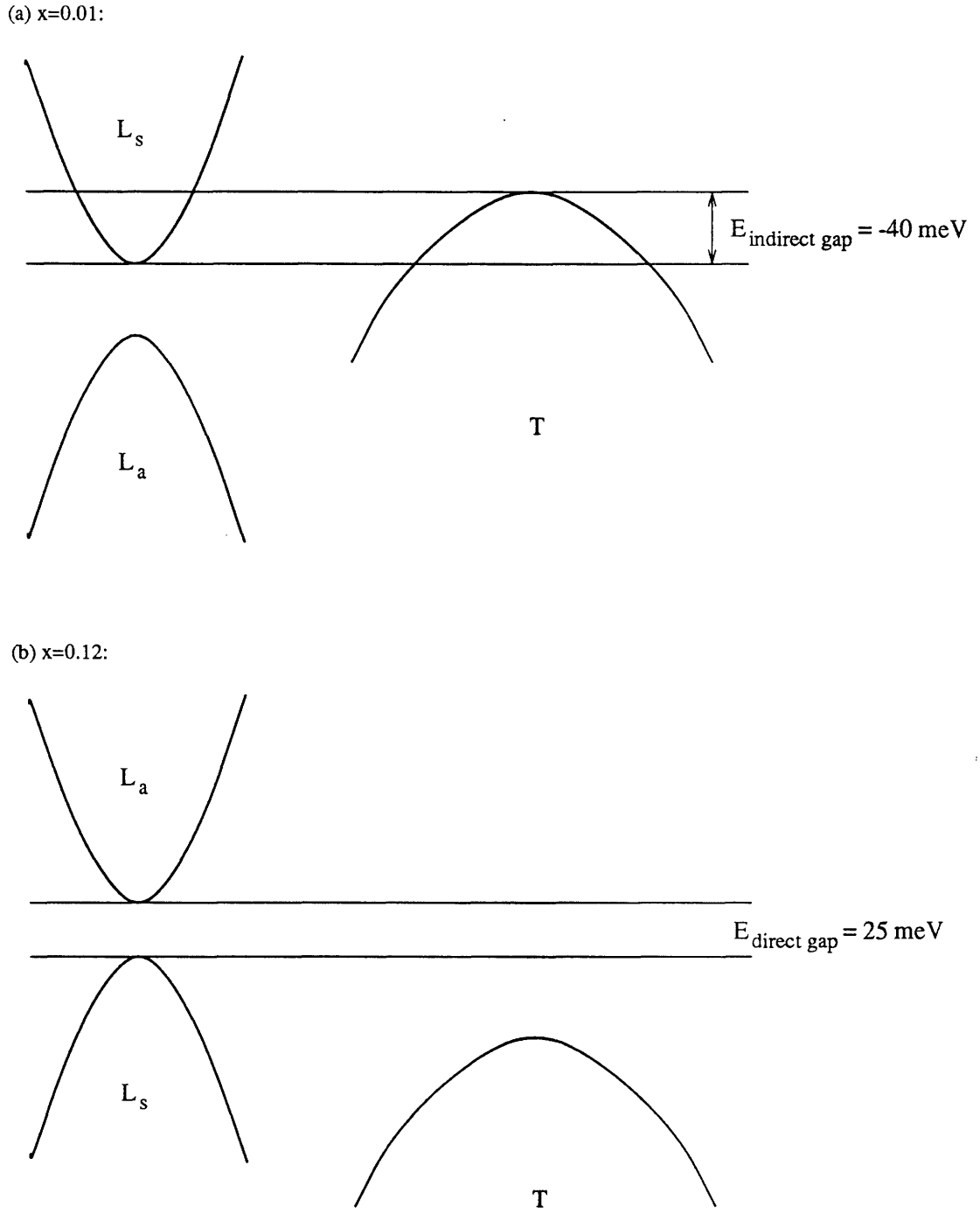

Figure 5-3: Schematic representation of the bands in the vicinity of the Fermi level for the $Bi_{1-x}Sb_x$ alloys with two alloy compositions: (a) $x = 0.01$ (Semimetal), (b) $x = 0.12$ (Semiconductor).

Table 5.1: Theoretical and experimental background decay times for the $Bi_{.99}Sb_{.01}$ and $Bi_{.88}Sb_{.12}$ alloys.

τ_{el}(ps)	$x = 0.01$	$x = 0.12$
Calculated	5	8
Experimental[a]	1.34	5.0

[a] From reference [17].

electronic temperature of the resulting quasi-equilibrated carrier distribution are determined by imposing the condition that the material remains intrinsic, and that the maximum energy gain of the electronic system equals the energy given by the pump pulse. As before, these conditions translate into an increase in the electronic temperature by approximately one order of magnitude to reach quasi-equilibrium in the excited state. At this high electronic temperatures, we can make the approximation $k_B T_{el} - \hbar\omega_q \simeq k_B T_{el}$ in equation (5.7), which makes τ_{el} independent of the specific phonon frequency, at these high carrier temperatures. The lattice temperature T_L is considered to remain constant at 300 K. This is a rather gross simplification given the high thermal conductivity for Bi. More accurate calculations which would include effects of lattice heating are needed.

For very low Sb concentrations, the physical constants of the Bi-Sb alloy can be taken to be those of Bi, and we can therefore use the values $\rho = 9.8\ \mathrm{g/cm^{-3}}$, $E_1 = 2eV$ and $\sqrt{\langle x_q^2 \rangle} \simeq 0.05\mathring{A}$ [7][4]. The substitution of these parameters in equation (5.9) leads to the numerical results for τ_{el} presented in Table 5.1, where we have also included the experimental values. These numerical estimates are consistent with the experimental values, inasmuch as they predict a faster decay rate when the bands overlap. The smaller value of τ_{el} in the semimetallic $Bi_{1-x}Sb_x$ alloys than in the semiconducting samples can thus be explained in terms of a higher density of states available for electron-phonon scattering in the semimetallic phase.

[4]The value of the deformation potential constant is for an acoustic phonon field, which we have used due to the lack of empirical data for the optical deformation potential constants. The results of the calculations may be only interpreted as an estimate of the time scale for the electronic relaxation. In any case, the approximations made throughout the analysis already restrict the results to an order-of-magnitude estimation.

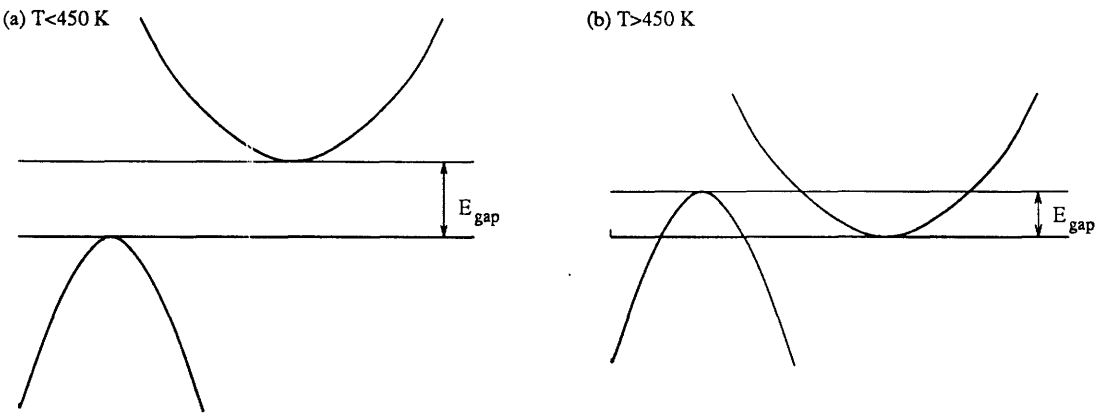

Figure 5-4: Schematic representation of the bands for Ti_2O_3 in the vicinity of the Fermi level at the temperatures: (a) T < 450 K (Semiconductor), (b)T > 450 K (Semimetal).

5.4 Titanium sesquioxide

An analogous behavior can be found in Ti_2O_3, in which the decay time τ_{el} decreases as the temperature is increased across the metal-semiconductor transition [3]. Presumably, the decrease in τ_{el} when the material becomes more metallic is also a result of the increase of the density of states available for electron-phonon scattering when the indirect band gap becomes negative. In the particular case of Ti_2O_3, the temperature is the driving mechanism of the lattice distortions leading to the transition.

Using a similar rigid band model as for the $Bi_{1-x}Sb_x$ alloys (see Figure 5-4), we can calculate τ_{el} from equations (5.9) and (5.10), once we have the pertinent parameters for the Ti_2O_3. The expression for the background decay now becomes:

$$\frac{1}{\tau_{el}(T)} \simeq \frac{2\langle x_q^2\rangle E_1{}^2 m_0{}^3 (k_B T_{el})^2}{\pi^3 \hbar^5 \Delta E \rho}\left[1 - \frac{\hbar\omega_q}{k_B T_{el}} n_q\right]\times$$
$$\times\left\{\left(\frac{m_e}{m_0}\right)^3 f_2\left[exp\left(-\frac{2E_F(T)-E_g(T)}{2k_B T_{el}}\right)\right] + \left(\frac{m_h}{m_0}\right)^3 f_2\left[exp\left(\frac{2E_F(T)+E_g(T)}{2k_B T_{el}}\right)\right]\right\}. \tag{5.11}$$

Unfortunately, the conduction and valence bands for this material are not well characterized, and there is a large range of values in the literature for the effective carrier masses[5], namely $m^*/m_0 \sim 2-5$. Although there seems to be agreement in the

[5] I refer to the data compiled in Landolt and Börnstein, Vol. III/17g, p. 151 ff. [28].

value for the experimental indirect band gap at room temperature of ~ 0.15 eV [28], there is a very large uncertainty in the experimental predictions for the evolution of the indirect band gap with temperature. A band model based on heat conductivity measurements [59] suggested shifts of the band overlap throughout the transition as large as 1 eV. A more modest estimate of the change of band overlap was provided by Lucovsky *et al.*, from electrical conductivity measurements below the semiconductor-semimetal transition [58]. By means of a simple two-band model, and assuming that the Ti_2O_3 is a non-degenerate semiconductor for this range of temperatures, Lucovsky predicted that the indirect band gap would become zero at $\sim$465 K. No information was given about the further evolution of the gap at temperatures above the transition.

It seems ironic that the pump-probe data for a material which is so poorly characterized give such good fits for the various DECP parameters, contrary to what happened to the $Bi_{1-x}Sb_x$ alloys for small x. In these circumstances, we can use our experimental data to improve the understanding of the microscopic behavior of Ti_2O_3, by simply inverting the roles of the knowns and unknowns in equation (5.11). Specifically, we observed in Figure 5-1 a correlation between the background decay, τ_{el}, and the fact that the material was undergoing a semiconductor-semimetal transition. On these grounds, we can use the functional dependence of the pump-probe experimental decay times on temperature to predict the evolution of the band gap in the temperature range from 300 K to 600 K. The only empirical parameters that we use in our model are the effective masses and the indirect band gap value at 300 K. From thermoelectric power measurements, we have $m_h = 5m_0$ for the holes [60], and the effective mass for the electrons is taken to be $m_e = 2m_0$ [28].

Using an analogous procedure to that followed for the Bi-Sb system, the Fermi level and electronic temperature at 300 K are determined by imposing that the material remains intrinsic. We adopt the value for the indirect band gap of Ti_2O_3 at room temperature $E_g = 13$ meV [59]. The maximum energy per unit volume provided by the laser is evaluated using equation 4.11 in Section 4.3.2:

$$\Delta E = \frac{P_{pulse}(1-R)}{\pi r^2 l}. \tag{5.12}$$

Table 5.2: Values of the band gap, E_g, and the deformation potential constants, $|E_1|$, for Ti_2O_3, as calculated from a semi-empirical two-band model. The experimental values extracted from the literature are also included.

	E_g(eV)		$\|E_1\|$(eV)
	(T = 300K)	(T = 575K)	($\|$ c − axis)
Present work	0.13	−0.12	~ 2.1
Experimental values	$0.1 - 0.2$[a]	?	2.1[b] 1.8 ± 0.6[c]

[a] Reference [28].
[b] From elastic constants data [56].
[c] From piezoresistivity measurements [57].

Here, P_{pulse} = 10 pJ, R = 0.1 and $Im\epsilon$ = 2 (*i.e.*, $l = c/2\omega Im\epsilon \sim 40\AA$), at $\hbar\omega$ = 2 eV [28], and the beam radius is $r = 1\mu$m.

Substituting those values in equation (5.11), and using from pump-probe data at room temperature τ_{el}(300K)=300 fs, we can extract the value of an effective deformation potential for the scattering of carriers with phonons. The value obtained is $|E_1| = 2.1$ eV, and is included in Table 5.4, together with the acoustic deformation potential constants from the literature, for comparison. The agreement between the theoretical and experimental values of $|E_1|$ is very good. Nevertheless, we must regard this agreement as fortuitous, given that the approximate character of our simplified model restricts the analysis of the results to an order-of-magnitude estimate.

Once $|E_1|$ is determined, we can study the temperature-dependence of the indirect band gap in the range 300 K-575 K. The result of this analysis is plotted in Figure 5-5, together with the results from Lucovsky's work [58]. The values of the band gap at 300 K and 575 K are listed in Table 5.4.

According to our fit, the band gap changes by about 0.3 eV during the semiconductor-semimetal transition, and this change in E_g is on the same order of magnitude as the estimated changes from conductivity data. A 0.3 eV change in E_g thus

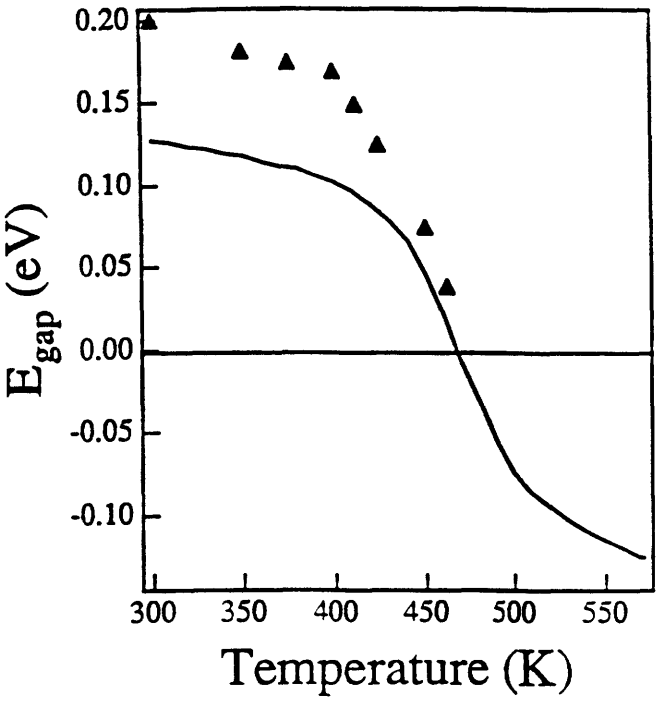

Figure 5-5: Evolution of the indirect band gap for titanium sesquioxide across the semiconductor-semimetal transition, obtained from temperature-dependent pump-probe measurements of the decay of the background [6]. The triangles indicate semi-empirical predictions from conductivity measurements [58].

seems more plausible than the 1 eV value predicted from heat conduction experiments.

5.5 Conclusions

In this Chapter, we have shown that electron-phonon scattering processes provide a plausible mechanism for the exponential decay of the background of the transient modulated reflectivity signal.

In the $Bi_{1-x}Sb_x$ and Ti_2O_3 systems, the smaller values of the electronic relaxation time τ_{el} in the semimetallic phase, relative to the corresponding values in the semiconducting phase, can be attributed to a larger density of states available for scattering.

In the Bi-Sb system, we have estimated τ_{el} to be on the order of a few picoseconds, a time scale which is two orders of magnitude longer than for Ti_2O_3. The different carrier relaxation of these two systems is mainly due to the values of the effective carrier masses, which are more than an order of magnitude larger in titanium sesquioxide than in the $Bi_{1-x}Sb_x$ alloys. The heavier carriers in Ti_2O_3 scatter much faster with

the phonons, because of the more similar mass of the electrons and ions involved in the scattering process.

We have also been able to predict the temperature-evolution of the indirect band gap in Ti_2O_3 across the semiconductor-semimetal transition. A word of caution should be raised in this case with regard to the assumption that the system reaches quasi-equilibrium on a time scale much shorter than the effective carrier relaxation time. Given that τ_{el} is only 100 fs, it is possible that the excited carriers do not achieve thermalization during their relaxation to the ground state.

Conclusion

In this thesis we develop theoretical models to explain the time-domain reflectivity response for a group of narrow-gap semiconductors and semimetals, when these materials are illuminated with ultrashort laser pulses. Emphasis has been put on a novel phenomenon, namely, the generation of coherent phonons with the full symmetry of the lattice.

The main purpose of this work is to describe quantitatively the microscopic processes associated with the generation and subsequent evolution of the coherent phonons. This phenomenon opens the door to study the coupled electron-ion dynamics in a narrow-gap material, when it is excited to a transient non-equilibrium state.

In addition, we have inspected an interesting physical implication of having a lattice oscillating in phase with the A_1 optical phonon frequency in a narrow-gap material: the possibility that the material undergoes a metal-insulator transition at a terahertz frequency. If this hypothesis was confirmed, one could develop an optical switch which would be faster than the electronic and optical devices available at the moment. T. K. Cheng's proposes in his doctoral dissertation [6] a series of experiments, ranging from fundamental studies to practical applications, which further exploit the novel phenomenon of coherent phonon oscillations. An interesting idea is the design of a terahertz modulator, which could be used to probe the change of carrier density in Sb, in order to verify the metal-insulator transition hypothesis from an experimental standpoint. I refer to Cheng's work for a complete description of the experiment.

The series of theoretical calculations presented in this thesis provide a qualitative

microscopic basis for the coherent phonon phenomenon. These calculations support the general notion that it is possible to modulate the ion coordinates in a solid so as to transform its physical characteristics at THz frequencies. Unfortunately, the properties of the narrow-gap materials are highly sensitive to the electronic structure in the vicinity of their band gaps. As a result, the approximate treatments that we have used in our models are insufficient to achieve a full quantitative description of the coherent phonon phenomenon from a microscopic viewpoint. Even the very accurate *ab initio* techniques encounter difficulties when attempting to describe the electronic band structure of narrow-gap semiconductors and semimetals close to the Fermi level.

We have also described the methods by which we could make quantitative evaluations of the coherent phonon amplitude and frequency shifts, even in the case that the complete calculation including spin-orbit coupling was not available.

This work could be taken as a preface to a more ambitious project, namely, the accurate and complete first-principles calculation of the changes in the lattice and band structure produced by a 2 eV laser pulse of a duration shorter than the optical phonon period in the group V semimetals Sb and Bi. Of course, the treatment can be extended to any system which can display this coherent phonon behavior. One could then know whether the indirect band gap can reverse its sign at a terahertz frequency, when the atoms oscillate in phase with large amplitudes. A last step required for the confirmation of the metal-insulator transition hypothesis is the calculation of the rate for scattering between electrons and holes, which should be larger than the characteristic oscillation period of the A_1 phonon mode.

In addition, one can calculate the dielectric function of these materials, and thus the transent reflectivity response observed in the pump-probe experiments. Also the *ab initio* dynamical calculation of the phonon dispersion relations in Sb and Bi remains to be done. At the present time, none of the existing theoretical calculations of the phonon dispersion relations in Sb and Bi can accurately describe the behavior of the optical branches. These calculations would undoubtely become part of any basic reference data book on these materials.

Bibliography

[1] T. K. Cheng, S. D. Brorson, A. S. Kazeroonian, J. S. Moodera, G. Dresselhaus, M. S. Dresselhaus, and E. P. Ippen, Appl. Phys. Lett. **57**, 1004 (1990).

[2] T. K. Cheng, J. Vidal, H. J. Zeiger, G. Dresselhaus, M. S. Dresselhaus, and E. P. Ippen, Appl. Phys. Lett. **59**, 1923 (1991).

[3] T. K. Cheng, J. Vidal, H. J. Zeiger, E. P. Ippen, G. Dresselhaus, and M. S. Dresselhaus. "Displacive excitation of Coherent Phonons", In *Ultrafast Phenomena VIII*, Springer Series in Chemical Physics, Vol.**55**, p. 66. Editors: J. -L. Martin, A. Migus, G. A. Mourou, A. H. Zewail. Springer Verlag, 1993.

[4] T. K. Cheng, J. Vidal, H. J. Zeiger, G. Dresselhaus, M. S. Dresselhaus and E. P. Ippen. "Proposed Modulation of a Metal-Semiconductor Transition at 7 TeraHertz", In *Materials Theory and Modeling: MRS Symposia Proceedings*, Boston, v. 291, edited by J. Broughton, P. D. Bristowe, and J. M. Newsam, page 619. Materials Research Society Press, Pittsburgh, PA, 1993.

[5] T. K. Cheng, L. H. Acioli, E. P. Ippen, J. Vidal, H. J. Zeiger, G. Dresselhaus, and M. S. Dresselhaus, Appl. Phys. Lett. **62**, 1901 (1993).

[6] T. K. Cheng, Ph.D. Thesis, Massachusetts Institute of Technology, 1994.

[7] H. J. Zeiger, J. Vidal, T. K. Cheng, E. P. Ippen, G. Dresselhaus, and M. S. Dresselhaus, Phys. Rev. B **45**, 768 (1991).

[8] R. L. Fork, B. I. Greene, and C. V. Shank, Appl. Phys. Lett. **38**, 671 (1981).

[9] E. P. Ippen and C. V. Shank. In *Picosecond Phenomena*, edited by C. V. Shank, E. P. Ippen, and S. L. Shapiro, page 104, Springer-Verlag, Berlin, 1978. Series in Chemical Physics.

[10] E. P. Ippen and C. V. Shank. In *Ultrashort Light Pulses*, edited by S. L. Shapiro, page 83, Springer-Verlag, Berlin, 1984. Chap. 3.

[11] In *Ultrafast Phenomena VII*, edited by C. B. Harris, E. P. Ippen, G. A. Mourou, and A. H. Zewail, Springer-Verlag, Berlin, 1990. Series in Chemical Physics: See also earlier volumes of this series.

[12] S. B. Brorson, Ph.D. Thesis, Massachusetts Institute of Technology, 1990.

[13] T. K. Cheng, M.S. Thesis, Massachusetts Institute of Technology, 1990.

[14] J. S. Lannin, J. M. Colleja, and M. Cardona, Phys. Reb. B **12**, 585 (1975).

[15] A. S. Pine and G. Dresselhaus, Phys. rev. V **4**, 356 (1971).

[16] S. H. Shin, R. L. Aggarwal, B. Lax, and J. M. Honig, Phys. Rev. B **9**, 583 (1974).

[17] J. Vidal, T. K. Cheng, A. W. Fung, H. J. Zeiger, G. Dresselhaus, M. S. Dresselhaus and E. P. Ippen. Pump-Probe Study of Bismuth-Antimony Alloys, In *Materials Theory and Modeling: MRS Symposia Proceedings*, Boston, v. 291, edited by J. Broughton, P. D. Bristowe, and J. M. Newsam, page 413. Materials Research Society Press, Pittsburgh, PA, 1993.

[18] Y. X. Yan and K. A. Nelson, J. Chem. Phys. **83**, 5391 (1986).

[19] Y. X. Yan and K. A. Nelson, J. Chem. Phys. **87**, 6240 (Part I) and 6259 (Part II) (1987).

[20] T. Pfeifer, W. Kütt, H. Kurzv, and R. Scholz, Phys. Rev. Lett. **69**, 3248 (1992).

[21] G. C. Cho, W. Kütt, and H. Kurz, Phys. Rev. Lett. **65**, 764 (1990).

[22] J. M. Chwalek, C. Uher, J. F. Whitaker, G. A. Mourou, and J. A. Agostinelli, Appl. Phys. Lett. **58**, 980 (1991).

[23] Y. R. Shen and N. Bloembergen, Phys. Rev. **A137**, 1787 (1965).

[24] J. Chesnoy and A. Mokhtari, Phys. Rev. **A38**, 3566 (1988).

[25] M. H. Cohen, L. M. Falicov, and S. Golin, IBM J. Res. Dev. **8**, 215 (1964).

[26] L. M. Falicov, and P. J. Lin, Phys. Rev. **141**, 562 (1966), and references therein.

[27] S. Golin, Phys. Rev. **166**, 643 (1968), and references therein.

[28] Landolt-Börnstein, *Numerical data and Functional Relationships in Science and Technology*, Volume **III/17e**. Editors: O. Madelung, M. Schulz, H. Weiss, Springer-Verlag, New York (1983).

[29] A. A. Lopez, Phys. Rev. **175**, 823 (1968).

[30] E. V. Bogdanov, N. B. Brandt, V. M.Manankov, and L. S. Fleishman, Sov. Phys. Semicond. **18** (7), 778 (1984).

[31] m. Akinaga, J. Phys. Soc. Jpn. **56** (2), 827 (1987).

[32] X. Gonze, J. -P. Vigneron, Phys. Rev. B **39**, 13120 (1989).

[33] D. C. Allan, and M. P. Teter, Phys. Rev. Lett **59**, 1136 (1987).

[34] X. Gonze, J. -P. Michenaud, and J. -P. Vigneron, Phys. Rev. B **41**, 11827 (1990).

[35] X. Gonze, R. Stumpf, and M. Scheffler, Phys. Rev. B **44**, 8503 (1991).

[36] R. H. Groenveld, R. Sprik, and A. Lagendijk, Phys. Rev. B **45**, 5079 (1992).

[37] M. C. Payne, M. P. Teter, D. C. Allan, T. A. Arias, and J. D. Joannopoulos, Rev. Mod. Phys. **64**, 1045 (1992).

[38] P. Hohenberg, and W. Kohn, Phys. Rev. B **136**, 864 (1964).

[39] W. Kohn, and L. J. Sham, Phys. Rev. **A140**, 1136 (1965).

[40] K. Walther, Phys. rev. **174**, 782 (1968).

[41] Y. Suido., Y. Yasida, S.Mase, J. Phys. Soc. Jpn. **39**, 109 (1975).

[42] J. F. Janak, Phys. Rev. B **18**, 7165 (1978).

[43] D. Pines, *Elementary excitations in solids.* Addison-Wesley, New York (1963).

[44] N. W. Ashcroft and N. D. Mermin, *Solid State Physics.* HRW International Editors, Philadelphia, 1976.

[45] R. K. Pathria, *Statistical Mechanics.* Pergamon Press, Oxford, 1972.

[46] P. Y. Wang, and A. L. Jain, Phys. Rev. B **2**, 2978 (1970).

[47] A. L. Jain, Phys. Rev. **114**, 1518 (1959).

[48] N. B. Brandt, S. M. Chudinov, V. G. Karavev, Sov. Phys. JETP **34**, 368 (1972).

[49] J. S. Lannin, Phys. Rev. B **19**, 2390 (1979).

[50] C. N. R. Rao, R. E. Loehman, and J. M. Honig, Phys. Rev. Lett. **A 27**, 271 (1968).

[51] C. E. Rice and W. R. Robinson, Acta Cryst. B **33**, 1342 (1977).

[52] S. H. Shin, G. V. Chandrashekhar, R. E. Loehman, and J. M. Honig, Phys. Rev. B **8**, 1364 (1973).

[53] L. L. Van Zandt, J. M.Honig, and J. B. Goodenough, J. Appl. Phys. **39**, 594 (1968).

[54] P. B. Allen, Phys. Rev. Lett. **59**, 1460 (1987).

[55] W. Shockley and J. Bardeen, Phys. Rev. **77**, 407 (1950).

[56] H.-L. S. Chen and R. J.Sladek, Phys. Rev. B **16**, 4413 (1977).

[57] H.-L. S. Chen and R. J.Sladek, Phys. Rev. B **18**, 6824 (1978).

[58] G. Lucovsky, J. W. Allen and R. Allen, Inst. Phys. Conf. Ser. **43**, 465 (1979).

[59] H. L. Barros, G. V. Chandrasekhar, T. C. Chi, J. M. Honig, and R. J. Sladek, Phys. Rev. B **7**, 5147 (1973).

[60] J. Yahia and H. P. R. Frederikse, Phys. Rev. **123**, 1434 (1961).

[61] From private discussions with Prof. Ippen.